

Development of Innovative Coatings
for Sun Protection Glasses
Based on the Theory
of the Optimal Spectral Transmittance

Inauguraldissertation

zur

Erlangung der Würde eines Doktors der Philosophie

vorgelegt der

Philosophisch-Naturwissenschaftlichen Fakultät
der Universität Basel

von

Iris Mack
aus Tübingen
(Deutschland)

Basel, 2008

Genehmigt von der Philosophisch-Naturwissenschaftlichen Fakultät
auf Antrag von

Prof. Dr. Peter Oelhafen

Prof. Dr. Ernst Meyer

Basel, den 31. März 2008

Dekan Prof. Dr. Hans-Peter Hauri

Abstract

In this work new coatings for sun protection glasses for windows and glass facades were developed. These coatings improve the reduction of the energy input by solar radiation in comparison to the best sun protection glasses on the market. They reduce the cooling load of buildings and therefore contribute to the measures to reduce global climatic changes on earth.

The new developed coatings are multilayer systems which are based on the principle of Fabry-Perot interference filters. The thin film multilayer systems are deposited on glass by magnetron sputtering under high vacuum conditions. The materials used in those coatings are silver, zinc oxide, titanium dioxide and silicon dioxide. Different coating designs were developed based on two bandpass filters, a metal-dielectric and an enhanced metal-dielectric filter. They were optimised to have a low energy load coefficient τ_e/τ_v and at the same time a stable colour appearance and a colour neutral light transmittance τ_v . The new coatings have energy load coefficients τ_e/τ_v between 0.339 and 0.398. For comparison one of the best commercial sun protection glass has an energy load coefficient of $\tau_e/\tau_v = 0.429$. A theoretical limit for this coefficient was determined to be at 0.334 if colour neutrality of the transmitted light is required.

Contents

1	Introduction	7
1.1	Anthropogenic Climate Change	7
1.2	Architectural Trend	12
1.3	New Coatings for Sun Protection Glasses	14
2	Theory of Sun Protection Glasses	15
2.1	Spectral Transmittance $\tau_{min}(\lambda)$	16
2.2	Transparent Conductive Coatings	20
2.3	Optical Filters	23
2.3.1	Fresnel's Equations for Thin Films	24
2.4	Bandpass Filters	28
2.4.1	Bandpass Filters with ZnO and Ag	30
2.4.2	Enhanced Bandpass Filters with TiO ₂ , Ag and SiO ₂	31
3	Simulations	33
3.1	From Theory to Real Multilayers	33
3.2	Evaluation of the Simulated Multilayer Stacks	35
3.3	Simulations for Optimisation during Deposition	37
4	Experimental Methods	39
4.1	Preparation of the Samples	39
4.1.1	Different Substrates	41
4.1.2	Magnetron Sputtering Deposition	42
4.1.3	Thickness Monitoring	44
4.2	Photoelectron Spectroscopy	45
4.3	Optical Measurements	50
4.3.1	Spectrophotometer	50
4.3.2	Window Stand	51
4.3.3	Spectral Ellipsometry	52
4.4	Resistivity Measurements	54

4.5	Scanning Electron Microscopy	56
5	Results	59
5.1	The Different Interfaces	59
5.1.1	Silver on a Dielectric Layer	60
5.1.2	Metal Oxides on Silver Layers	65
5.2	Multilayer Coatings	69
5.2.1	Design with TiO ₂ , Ag and SiO ₂	70
5.2.2	Design with ZnO and Ag	75
5.2.3	Influence of the Number of Silver Layers on the Spectral Prop- erties of the Coatings	83
6	Conclusions	91
A	Optical Functions and Quantities	97
A.1	Solar Spectrum and Photopic Luminous Efficiency	97
A.2	Light Transmittance and Direct Solar Transmittance	97
B	Electromagnetic Waves and Matter	99
B.1	Maxwell Equations	99
B.2	Drude Model	100
B.3	Plasma Frequency ω_p	101
	Bibliography	103
	List of Acronyms	113
	Important Quantities	115
	Acknowledgment	117
	Curriculum Vitae	119

Chapter 1

Introduction

Climatic change is a well discussed topic in the media nowadays. But it is not only playing an important role in the media, it is an important issue in politics too. This shows the increasing amount of global climate conferences taking place all over the world. The Nobel Peace Prize 2007 further stresses the actuality of this topic. The Intergovernmental Panel on Climatic Changes (IPCC) ¹ and Albert Arnold (Al) Gore Jr. were awarded by the Nobel comity “for their efforts to build up and disseminate greater knowledge about man-made climate change, and to lay the foundations for the measures that are needed to counteract such change”². One of the key sentences in the book *An Inconvenient Truth* by Al Gore is: “Beyond death and taxes, there is at least one absolutely indisputable fact: Not only human-caused global warming exist, but it is also growing more and more dangerous, and at a pace that has now made it a planetary emergency” [1]. The development of new coatings for windows and glass facades to save energy is described in this thesis. The aim of this development is to contribute to the measures to save the climatic conditions we are now experiencing and to suppress climatic changes.

1.1 Anthropogenic Climate Change

Earth is one of 287 known planets in our galaxy, yet it is the only one known to support life [2]. Life was able to develop on our planet due to its distance from the sun and because it possesses a number of gases in its atmosphere which have the ability to absorb and reradiate terrestrial infrared radiation. These gases are referred to as greenhouse gases, as an analogue to the glass of a greenhouse which lets visible solar

¹www.ipcc.ch

²http://nobelprize.org/nobel_prizes/peace/laureates/2007/

radiation through but traps much of the heat (infrared radiation) inside. Without these atmospheric gases and the resulting greenhouse effect, the global average temperature on earth would be -19°C instead of 14°C [1, 3]. Without the presence of these greenhouse gasses, it is uncertain whether life would have developed on Earth. The most important greenhouse gases are carbon dioxide (CO_2), methane (CH_4), nitrous oxide (N_2O), sulphur hexafluoride (SF_6), water vapour (H_2O), ozone (O_3), and the chlorofluorocarbons (CFCs including CFC-12 (CF_2Cl_2) and CFC-11 (CFCl_3)) [3].

Since 1750 the global concentration of atmospheric greenhouse gases has increased drastically due to human activities. The gas concentrations have exceeded pre-industrial values. Figure 1.1 illustrates the increase of the three greenhouse gases CO_2 , CH_4 and N_2O over the last 10 000 years. It is obvious that the amount of those gases was stable for a very long time and has increased drastically during the last century. This increase started with the industrial revolution and the accompanying huge amount of fossil fuel which has been burned. For example the amount of carbon dioxide was 280 ppm (parts per million) in 1750 and has reached a value of 380 ppm in 2005 (Figure 1.1) [4]. The

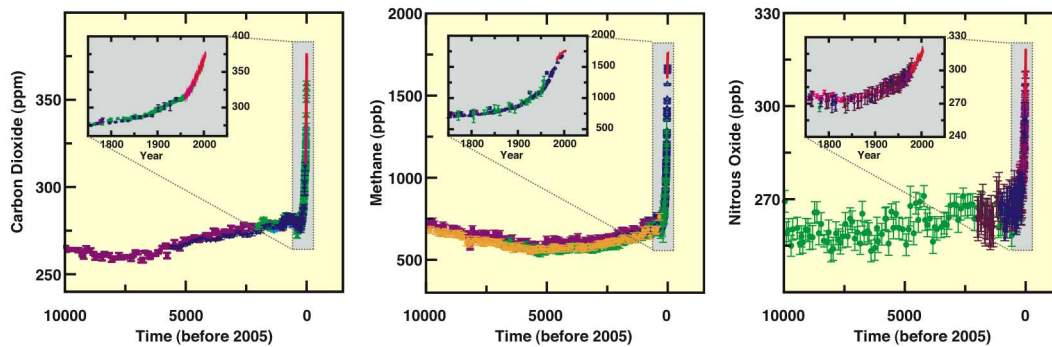


Figure 1.1: Atmospheric concentration of carbon dioxide, methane and nitrous oxide over the last 10 000 years (large panels) and since 1750 (insert panels). Measurements are shown from ice cores (symbols with different colours for different studies) and atmospheric samples (red lines) [4].

increase in global atmospheric CO_2 since the industrial revolution is mainly due to CO_2 emissions from fossil fuel used in transportation, building heating and cooling, gas flaring and cement production. Other sources include emissions due to land use changes such as deforestation and biomass burning [5]. About 50% of an increase in atmospheric CO_2 will be removed within 30 years, another 30% will be removed within a few centuries and the remaining 20% may remain in the atmosphere for many thousands of years, if no new carbon dioxide would be produced [6, 7].

As a result of agriculture, natural gas distribution and landfills, the amount of methane in the atmosphere increased from 715 ppb (parts per billion) to 1775 ppb in the same time period (i.e., 1750 to 2005). The main natural source for CH_4 are wetlands. The anthropogenic sources are rice agriculture, biomass burning, ruminant animals, waste

disposal in landfills and fossil fuel mining and distribution. Another important factor is that once emitted, methane remains for approximately 8.4 years in the atmosphere [6].

More than a third of all the N_2O emission is due to human agricultural activities. The total amount of nitrous oxide has increased from 270 ppb to 319 ppb in the last 150 years [4]. The main contributions come from fertiliser use, fossil fuel burning, biomass burning and raising cattle. Once emitted, N_2O remains in the atmosphere for approximately 114 years before being essentially removed, mainly by destruction in the stratosphere [6].

Increasing the percentage of greenhouse gases has the consequence of a global temperature rise, as more infrared radiation coming from the surface of the earth is reflected in the atmosphere back to the surface. This effect and other phenomena, which influence global temperature are described as radiative forcing. Radiative forcing is the change in the net, downward minus upward, irradiance [W/m^2] at the tropopause [8]. The tropopause is the boundary between the troposphere and the stratosphere. Radiative forces can be associated with human activities or natural processes. Data presented in figure 1.2 reveal that nearly all factors influencing the radiative forcing are due to human activities. One of the factors shown in the figure is the increase of the radiative force by the amount of ozone (O_3) in the atmosphere. On the one hand ozone in the stratosphere reduces the radiative force, but ozone is destroyed by halocarbons released by human activities. On the other hand ozone is a greenhouse gas that is continuously produced in the troposphere by chemical reactions released through the other greenhouse gases. Ozone in the troposphere adds to the radiative forcing, while ozone in the stratosphere reduces. A reducing factor is the amount of aerosols in the atmosphere. Aerosols are small liquid or solid particles, with a typical size between $0.01 \mu\text{m}$ and $10 \mu\text{m}$ that scatter or absorb radiation or act as condensation nuclei for clouds, who again reflect radiation back to space. Natural processes that influence the radiative forcing are changes in solar irradiance and explosive volcanic eruptions. Volcanic activity has not been significant since the eruption of Mt. Pinatubo in 1991 thus only changes in solar irradiance have to be taken into account when the current radiative forcing is determined [5]. As a result, the radiative forcing from human activities is much more important for current and future climate change than the radiative forcing from changes in natural processes.

Summing the positive and negative radiative forces in figure 1.2 results in a total net effect due to human activities since 1750 of warming with a radiative forcing of $1.6 \pm 1.0 \text{ W}/\text{m}^2$ [4, 5]. That this global warming has already started is unequivocal. There is evidence that the number of cold days and nights has decreased during the last decade. In addition, warm days and nights, as well as heat waves have become more

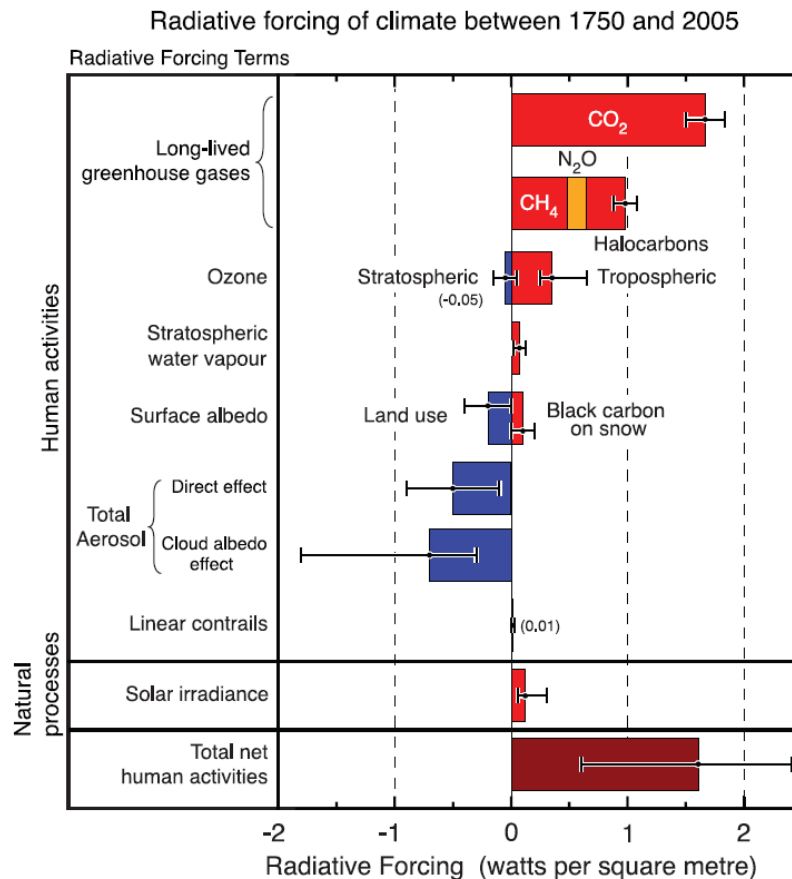


Figure 1.2: Overview of the principal components of the radiative forcing of climate change. All these radiative forcing result from one or more factors that affect climate and are associated with human activities or natural processes. The values represent the forcing in 2005 relative to the start of the industrial era in 1750. Human activities cause significant changes in greenhouse gases, ozone, water vapour, surface albedo, aerosols and contrails. The only increase in natural forcing of any significance between 1750 and 2005 occurred in solar irradiance. Positive forcing lead to a warming of the climate and negative forcing lead to a cooling. The thin black line attached to each coloured bar represents the range of uncertainty for the respective value [5].

frequent [9]. Inspection of the global mean temperature reveals that eleven of the last twelve years (1995 - 2006) rank among the twelve warmest years since the beginning of the instrumental recording of the global surface temperature in 1850 [4].

Figure 1.3 shows the evolution of the temperature over the last 195 years. The annual global mean temperatures are plotted in black dots and the smoothed evolution of the temperature is shown in blue. To give an idea of whether the fluctuations are meaningful, decadal 5% to 95% (light grey) error ranges around that curve are given. The left hand axis gives the difference to the global average between the years 1961 and 1990. The right axis gives the estimated actual global mean temperatures. The coloured lines show linear trend fits for different time periods. This figure illustrates that the rate of temperature increase has itself increased from 0.045°C per decade in the last 150 years (red) to 0.177°C per decade in the last 25 years (yellow) [9]. Further

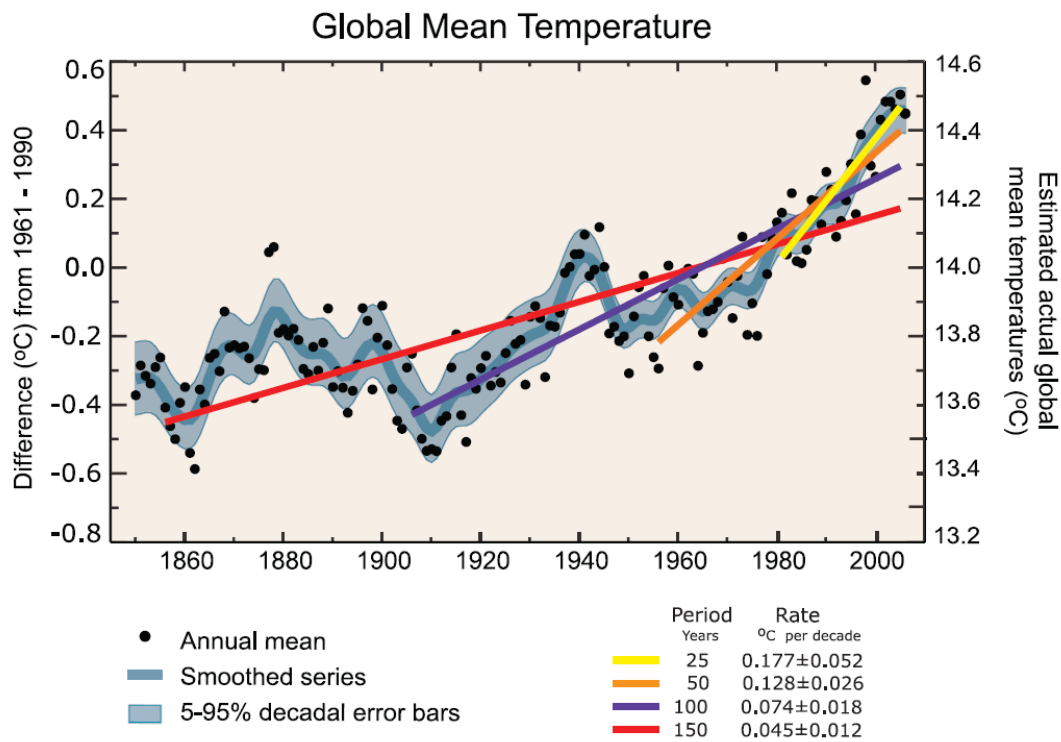


Figure 1.3: The observed annual global mean temperatures (black dots) along with simple fits to the data. The left hand axis shows anomalies relative to the 1961 to 1990 average, and the right hand axis shows the estimated actual global mean temperature. Linear trend fits to the last 25 (yellow), 50 (orange), 100 (purple) and 150 years (red) are shown. The slope for recent periods is greater, indicating accelerated warming. The blue curve shows the smoothed evaluation of the temperature. The decadal 5% to 95% error ranges are indicated in light grey [9].

observations since the 1950s have shown that the troposphere (up to about 10 km) has warmed at a slightly greater rate than the surface, while the stratosphere (about 10 – 30 km) has cooled markedly since 1979. This demonstrates the important role of increased greenhouse gases in the atmosphere and the destroying of the ozone layer [9].

The consequences of global warming include [9]:

- Decrease in the length of river and lake ice seasons
- Reduction of glacial mass
- Retreating of sea ice in the Arctic
- Melting of the Greenland Ice Sheet
- Diminishing of snow coverage in the Northern Hemisphere
- Ocean warming
- Sea level rising due to thermal expansion of the oceans
- Melting of land ice

In comparison to the sea level at the end of the last ice age (approximately 21 000 years ago) the global sea level rose by about 120 m during several millennia and than stabilised between 3 000 and 2 000 years ago. Between 1961 and 2003 the global sea level rose about 1.8 mm per year, but the rate has further increased and is now 3.1 mm per year [10]. This seems to be insignificant, but if one considers that the sea level was stable for several thousand years before the beginning of the industrialisation, the change is enormous. Present-day sea level change is of considerable interest because of its potential impact on human population living in coastal regions or on islands.

The fact that climate change is occurring is obvious. Simulations show that changes will be extreme even if the production of carbon dioxide is stopped immediately. Since greenhouse gases remain several years to decades in the atmosphere warming would continue at a rate of 0.1°C per decade. For the next two decades simulations have predicted increases of 0.2°C per decade up to 4.0°C per decade [4]. The different rates are interlinked but do not depend linearly with the greenhouse gas emission. The warmer our climate becomes, the higher the rate of change. This is because less CO_2 can be stored naturally, and more water vapour is ejected into the atmosphere thereby increasing the greenhouse effect [6].

The aforementioned future climate change makes it clear that the human race has to change its attitude and behaviour towards nature and energy consumption. It is necessary to put a huge effort into finding alternative energy sources to replace or mitigate the current demand for fossil fuel and coal. In addition, society must reduce the consumption of energy wherever possible to decrease the emission of greenhouse gases. Furthermore, our humanity will have to find ways to adapt to the new climatic situation which it will face due to its behaviour now and in the past.

1.2 Architectural Trend

In 1990, the residential, commercial and institutional building sectors were responsible for roughly one-third of the global energy use and associated carbon oxide emission [11, 12]. In these sectors, energy is used for appliances, heating and cooling systems, lighting and all plug loads, including office equipment. In order to reduce the energy consumption and the associated greenhouse gas emission in the building sectors, new technologies aimed at reducing the energy use in building equipment, and reducing heating and cooling energy losses through the building envelope are needed [13].

Improvements in the thermal envelope of buildings can reduce heating requirements by a factor of two to four [14]. Heat transfer through the buildings envelope takes place

at roofs, walls and windows. By controlling the overall thermal transfer value of the building envelope, reductions in heating and cooling requirements can be achieved [13]. The space load of buildings sums up the energy (heat) inputs, like people, electrical equipment and the heat transfer through the buildings envelope into the building. An increase of space load leads to an increase in the chillier load, which corresponds to a higher use of air conditioning [13]. If nothing is changed and temperature will rise by $4,5^{\circ}\text{C}$ the electrical consumption during summer will more than double for northern Europe due to air conditioning and refrigeration [15, 16].

Modern architecture, especially in commercial buildings, is dominated by glass facades. Figure 1.4 shows as an example for glass facades the *Messturm* in Basel, Switzerland. To reduce the energy use of modern buildings it is necessary to use spectral selective and insulating windows, since roughly 7% of the annual energy consumption is tied to fenestration properties [17]. Spectral selective glasses can maximise the transmission of visible sunlight to replace artificial lightning, while minimising cooling requirements from solar heat gain [14, 17]. This is achieved by multilayer coatings on the glass panels which let visible light ($\lambda = 380\text{ nm} - 780\text{ nm}$) through but reflect ultraviolet ($\lambda = 320\text{ nm} - 380\text{ nm}$) and infrared ($\lambda = 780\text{ nm} - 3000\text{ nm}$) radiation. This means, that these coatings have the aim to reduce the ratio of

the total solar radiation transmitted through the glazing to the visible day light transmitted. There are a huge variety of such glasses on the market, but the problem of overheating during summer is not yet solved. One problem is that new buildings are not designed as a complete system, but by different groups which do not interact during the design phase. In addition, architects mainly choose reflecting glass due to aesthetic considerations rather than reduction of solar gain [13]. Another problem is that current sun protection windows on the market are ineffective at filtering infrared radiation and therefore the solar direct radiation τ_e is higher than needed for the same light transmittance τ_v .



Figure 1.4: Example of modern architecture which is dominated by glass facades. The Messturm in Basel, Switzerland is shown here.

1.3 New Coatings for Sun Protection Glasses

A fact that can not be ignored is the man-made climatic change described in the introduction of this thesis. Measures to reduce the amount of CO₂ produced by the use of fossil fuels and the other greenhouse gases is a difficult task we have to face. A sector of high actuality is the building sector as it is responsible for roughly one-third of the global energy use [11, 12].

The subject of this thesis is the development of new coatings for sun protection glasses which reduce the energy input to a building. The theoretically minimised spectral transmittance τ_{min} described in chapter 2.1 was the starting point for the development. A requirement for the new coatings is that they should be made out of standard materials used in industrial production for existing sun protection glasses, to reduce the investigations for the production of those new coatings.

A critical point, that the new developed coatings should fulfil, is the reduction of the energy input by blocking all the incoming infrared light. For this enterprise it is necessary to develop multilayers with a high infrared reflectance. Furthermore, it is very distracting for the human eye, if the day light entering a building is not colour neutral. From this followed for the coatings, the colour of the transmitted light should be colour neutral. As the sun is seldom penetrating perpendicular through a glass facade it is important that improved energy properties as well as the colour neutrality are valid for a large range of incident angles.

The challenge of this thesis is to find a multilayer coating that fulfils these requirements and has a transmittance that is equal to the theoretical minimised transmittance τ_{min} . Besides the finding of a layer stack the interaction between the different layers during the deposition is a crucial point that has to be dealt with. In order to be able to fully optimise the multilayer coating and its components, they have to be deposited and characterised. The characterisation includes optical measurements, as well as surface and chemical analyses.

Chapter 2

Theory of Sun Protection Glasses

Sun protection glasses (SPG) in general consist of two glass panes which are separated by a gas-filled space. A typical sun protection glass system and a schematic diagram for the incident, transmitted, reflected, and absorbed light is shown in figure 2.1. Incident

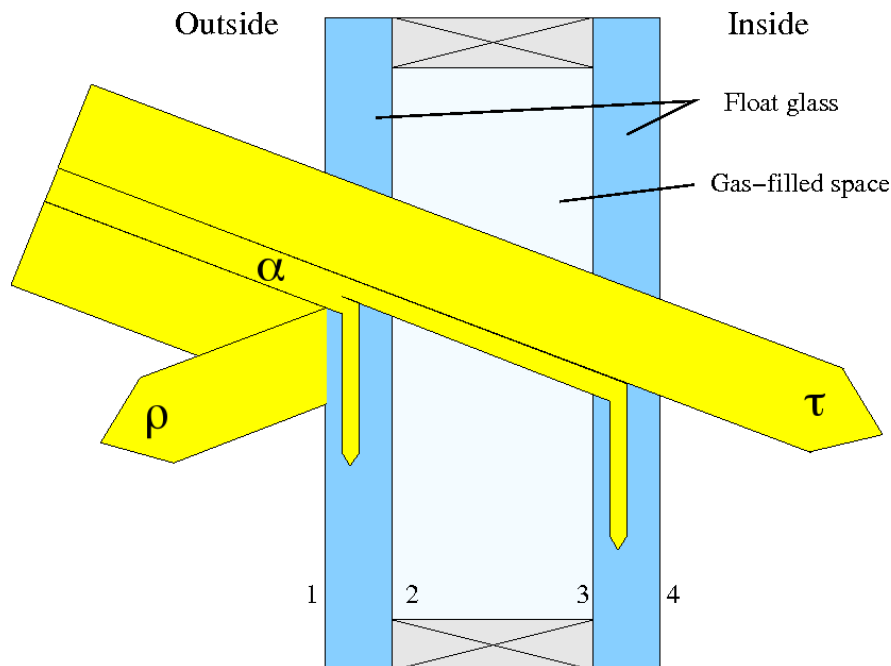


Figure 2.1: Schematic setup of a sun protection glass which in general consist of two glass panes that are separated by a gas-filled space. In yellow the splitting up of the incident light into the three components transmittance τ , reflectance ρ and absorptance α is shown. The numbers one to four show the possible positions for coatings. For simplicity reasons the multi reflections between the glasses are omitted.

light striking a surface is split into transmitted (τ), reflected (ρ) and absorbed (α)

light. The fact that the sum of these three components is equal to one is described in the fundamental relationship known as the radiation distribution equation:

$$\tau + \varrho + \alpha = 1 \quad (2.1)$$

τ transmittance
 ϱ reflectance
 α absorptance

This equation is based on the law of energy conservation. The ratio between these different components can be influenced by coatings on the glass panes. All possible surfaces for coatings are indicated by the numbers at the bottom of the figure 2.1. In practice only the surfaces 2 and 3 are used, as the coatings this way are protected against scratching, oxidation, rain and chemical degradation.

On the whole two coating types are mainly used in the glass industry: so called Low-E glasses (low emissivity glasses) and sun protection glasses. They both have the aim to save energy in common. Low-E glasses reduce the energy consumption during heating, and sun protection glasses lower the required cooling energy. Coatings which reduce the energy consumption of a heating system are referred to in the scientific literature as heat-mirrors since they reflect the heat radiation from the inside of the building, thereby reducing the losses through the glass panes [18]. The heat radiation spectrum wavelengths are significantly larger than the incoming light from the sun as indicated in figure 2.2. An ideal heat-mirror therefore reflects all the radiation from $3 \mu\text{m}$ to larger wavelengths, but transmits all the radiation with wavelengths smaller than $3 \mu\text{m}$ [18, 19]. Whereas sun protection glasses are designed to only transmit the visible spectrum of the solar radiation, and reflect all the radiation with wavelengths greater than 800 nm. Due to this they reduce the cooling load in a building.

2.1 Spectral Transmittance $\tau_{min}(\lambda)$

In his paper “Optimal Spectral Transmittance of Sun Protection Glasses” P. Oelhafen from the University of Basel addresses the problem that current sun protection glasses on the market are not effectively reducing the energy input to a building by the sun [20, 21]. Furthermore he developed a spectral transmittance $\tau_{min}(\lambda)$ that has a minimal solar energy input. Since this thesis is based on the results of these papers they will be summarised in this section.

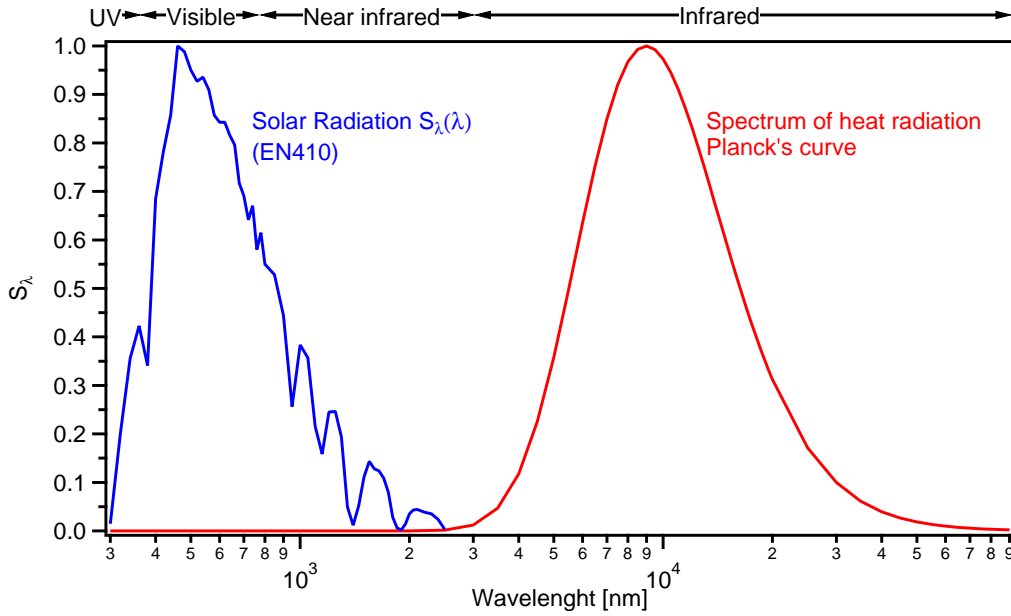


Figure 2.2: Comparison of the radiation spectra of the sun (blue line) and that of a 50° C heat radiator (red line).

With respect to the problems of overheating and increasing cooling loads, the question arises as to whether conventional sun protection glasses (SPG) have already reached their optimum performance. In order to evaluate the capabilities of SPG glass, one needs to know:

1. the performance of currently available sun protection glasses
2. what is the theoretical limit

In order to quantify the first point, the solar direct transmittance¹ τ_e , the light transmittance² τ_v (see appendix A.2) and the total solar energy transmittance factor (solar gain) g of several commercial sun protection glasses were determined as a function of the angle of light incidence φ at the University of Basel [22, 23]. From these parameters, the ratio τ_e/τ_v (energy load coefficient) and g/τ_v were obtained. These ratios are used to describe the energy load by solar radiation normalised to the luminous parameter τ_v .

For the second point, a theoretical spectral transmittance $\tau_{min}(\lambda)$ for sun protection insulating glasses was developed by P. Oelhafen at the University of Basel, Switzerland [20, 21]. The theoretical transmittance is based on standard spectral distributions: such as solar radiation $S_\lambda(\lambda)$, spectral photopic luminous efficiency $V(\lambda)$, standard illuminant $D_{65}(\lambda)$ and the CIE³ colour-matching functions \bar{x}_λ , \bar{y}_λ , \bar{z}_λ (see

¹Solar direct transmittance is the relative amount of solar radiation transmitted by a glazing.

²Light transmittance is the relative amount of day light transmitted through glazing.

³CIE - Commission internationale de l' éclairage

appendix A.1) [24]. The boundary conditions for $\tau_{min}(\lambda)$ where:

1. The ratio $\tau_e(\varphi)/\tau_v(\varphi)$ should be minimised.
2. The condition of colour neutrality for the transmitted light has to be fulfilled, i.e., daylight transmitted through the sun protection glass should be transformed to an attenuated white light, characterised by $a = 0$ and $b = 0$ in the CIE Lab colour space⁴.

In the first step the boundary conditions for colour neutrality was omitted for reasons of simplicity, and the spectral transmittance $\tau(\lambda)$ was restricted to the wavelength range for which the spectral photopic luminous efficiency $V(\lambda)$ is greater than nought. In other words it was restricted to wavelengths the human eye can detect:

$$\tau(\lambda) = c V(\lambda) \quad (2.2)$$

$\tau(\lambda)$	spectral transmittance
λ	wavelength
c	constant
$V(\lambda)$	spectral photopic luminous efficiency

The constant c is to scale the maximum of $\tau(\lambda)$ to a value smaller than one. This spectral transmittance function has a very low energy load coefficient ($\tau_e/\tau_v = 0.231$); however the colour of the transmitted light is very greenish ($a = -44$ (green) and $b = 93$ (yellow)).

By taking colour neutrality in to account, the spectral transmittance $\tau_{min}(\lambda)$ has the following form:

$$\tau_{min}(\lambda) = V(\lambda)^\delta [\alpha \cdot \bar{x} + \beta \cdot \bar{y} + \gamma \cdot \bar{z}] \quad (2.3)$$

$\tau_{min}(\lambda)$	minimised spectral transmittance
δ	constant
α, β, γ	weighting factors
$\bar{x}, \bar{y}, \bar{z}$	CIE colour-matching functions

The weighting factors α , β and γ were determined in such a way that colour neutrality is obtained for the transmitted daylight. The exponent δ , which influences the width of the curve $V(\lambda)$ and therefore the width of the transmitted wavelength range, was

⁴The CIE Lab colour space describes quantitatively the human perception of colours. All colours are given by the coordinates a and b in the ab -colour plane: the a -axis describes colours between green ($-a$) and red ($+a$), the b -axis describes colours between blue ($-b$) and yellow ($+b$). The L -axis is perpendicular to the ab -plane and describes the brightness (luminosity) of the colour.

chosen so that the ratio τ_e/τ_v as a function of δ is minimised. This leads to the final form of the spectral transmittance $\tau_{min}(\lambda)$

$$\tau_{min}(\lambda) = V^{\frac{1}{3}} [\alpha \cdot \bar{x} + \beta \cdot \bar{y} + \gamma \cdot \bar{z}] \quad (2.4)$$

with $\alpha = 0.4544$, $\beta = 0.4501$ and $\gamma = 1.00$. The energy load coefficient of this spectral transmittance is $\tau_e/\tau_v = 0.3341 \approx \frac{1}{3}$. The colour of the transmitted daylight is neutral ($a = 0$ (white) and $b = 0$ (white)).

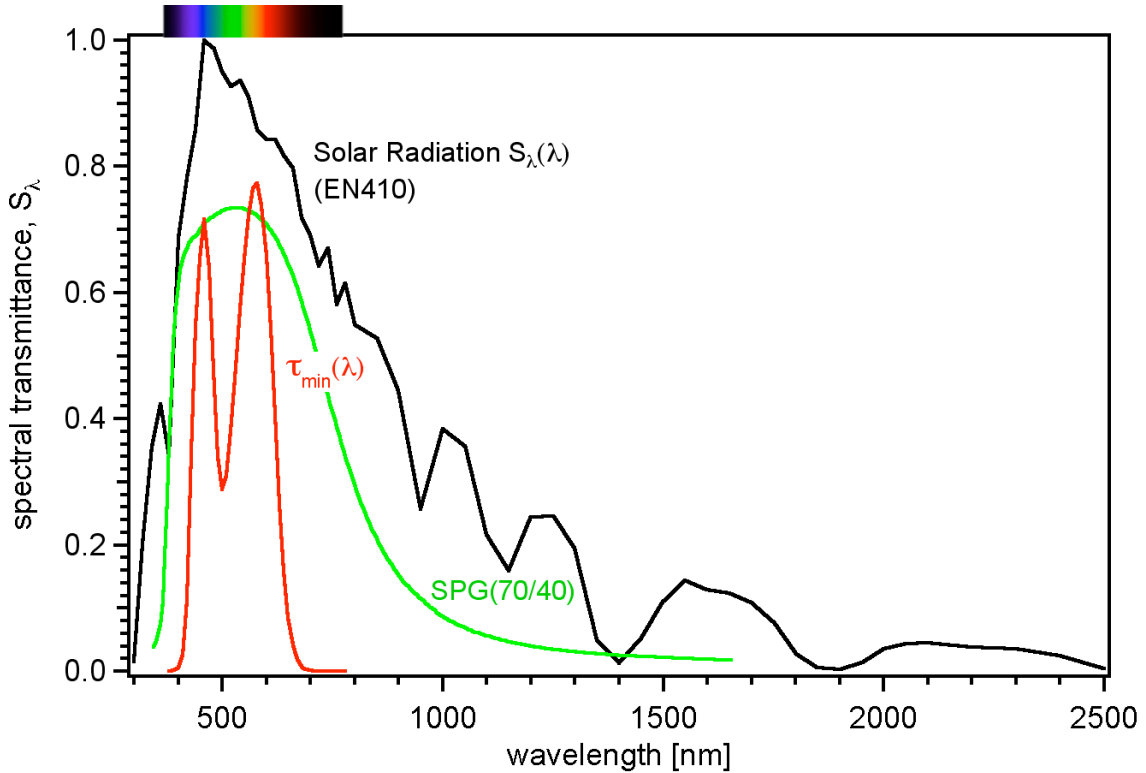


Figure 2.3: Comparison of the spectral transmittance $\tau_{min}(\lambda)$ with a sun protection glass (Glas Trösch AG: Silverstar Combi Neutral 70/40) and the solar spectrum $S_\lambda(\lambda)$ [24]. At the top of the graph the colours show the part of the spectrum the human eye can see.

The solar spectrum $S_\lambda(\lambda)$, the spectral transmittance $\tau_{min}(\lambda)$ and the transmittance for a typical commercial sun protection glass (Glas Trösch AG: Silverstar Combi Neutral 70/40) are shown in figure 2.3. In addition, a colour block indicating the wavelength range of the spectrum which is visible to the human eye is given. The SPG has a $\tau_e/\tau_v = 0.560$ for $\phi = 0^\circ$ as compared to 0.334 of $\tau_{min}(\lambda)$. The reason for the difference in energy load is that τ_{min} has a steeper edge at $\lambda = 780$ nm and therefore less invisible infrared radiation is transmitted. The investigation of several commercial sun protection glasses revealed that this transmission performance is typical. The result of this investigation is summarised in a database [25], where the measured spectra for different angles of light incidence and parameters like colour and energy load are given. The average of the best

25% of the commercial sun protection glasses in the glass database [25] is $\tau_e/\tau_v = 0.48$ for perpendicular light incidence. This is approximately 1.4 times higher than for the theoretical spectral transmittance τ_{min} . Most SPGs even show higher values. This means that the energy load of the interior by direct solar radiation could be reduced by 1/3 at constant light transmittance as compared to the best sun protection glasses presently on the market [22]. This energy reduction would lead to a reduction in cooling loads and would therefore reduce the associated greenhouse gas production. Consequently, by developing a sun protection coating with a spectral transmittance similar to $\tau_{min}(\lambda)$, a significant contribution to minimise climatic changes could be achieved.

2.2 Transparent Conductive Coatings

Transparent, electrically conducting coatings on glass can fulfil a variety of tasks. More than 90% of industrially produced flat glass products using thin film coatings are based on transparent conductive coatings, therefore these have greater economic importance than all other thin films used today [26].

There are two basic concepts to create transparent conductive coatings. They are produced either from semiconductive materials or from metals [27, 28, 29, 30, 31]. All the properties achieved with these coatings are based on the effects of the free electrons in these layers. Their significant distinguishing feature is whether the functions are based on the conduction of the free electrons in the layers, or on their interaction with electromagnetic radiation. The first effect is explained by *Ohm's law*, which states that an electric current flows within the layers as a voltage is supplied. The second effect mainly influences the reflectivity in the wavelength range from solar radiation to the long waves of radio transmission. Currently, the glass industry only utilises metal based coating. Consequently, only these coating materials will be discussed.

In a simplified model for metals, one electron per atom can be released leaving behind a positive metal ion at a lattice site [26]. The released electrons can move freely within the solid and they are called “gas of free electrons” or “plasma”. Although the electrons are free to move, the mobility μ of those electrons is determined by the kind and number of scattering processes through which they are deviated from their course through the metallic lattice. These scattering processes can be caused by structural faults in the layer, like interfaces, or by thermal oscillations of the atoms, known as lattice vibrations. Thin layers have other qualities contributing to the reduction of the mobility. For example scattering processes due to the layer surface condition (rough

or smooth) play an important role. In order to describe the interaction of electrically conductive layers with electromagnetic waves, it is useful to introduce the collision frequency ω_c . It is defined as the reciprocal of the mean collision time τ_c , which is defined as the average period between two scattering events which free electrons encounter on their way through matter.

The propagation of electromagnetic waves in matter is described by *Maxwell's equations* (see appendix B.1) [32]. From these equations it becomes clear that the physical behaviour of electromagnetic radiation in coatings is characterised by the angular frequency ω or the wavelength $\lambda = 2\pi\frac{c}{\omega}$ of the radiation and by the collision frequency ω_c of the free electrons in the different layers. First the two limiting cases $\omega \gg \omega_c$ and $\omega \ll \omega_c$ will be considered.

The first case deals with the behaviour of electromagnetic waves with an angular frequency ω that is much lower than the collision frequency ($\omega \ll \omega_c$). This condition is met by radiation with large wavelengths, i.e., from infrared through radio waves. In this case the incident radiation causes the free electrons in the conductive coating to oscillate collectively with the frequency ω of the incident radiation. Because the frequency ω is much lower than the collision frequency ω_c , the electrons can not transfer all the absorbed radiation energy to the lattice of the solid within the period of one oscillation. As a result, the absorptance α is low. Furthermore, due to the high number of free electrons, the penetration depth d_p of the radiation is so low that the transmittance τ is almost zero. From the radiation distribution equation (2.1) it follows that the amount of reflected radiation in the long wavelength range is very high. This is the reason why transparent conductive coatings are used to produce heat mirrors and sun protection coatings, as they show a high infrared reflectivity.

The second case ($\omega \gg \omega_c$) will now be discussed. In the case of thin films this is valid for the visible part of the spectrum. The frequency of the radiation in the visible part of the spectrum is too high for the free electrons to follow the electromagnetic field due to the inertia of their mass in motion. This is the reason for the high transparency of conductive coatings in the range of short wavelengths. Due to the fundamental relation (eq. 2.1) it follows that a high transmittance τ can only be achieved if both the reflectance ρ and absorptance α are sufficiently small. This shows, that thin metal layers have a high transmittance in the visible range.

For radiation with wavelengths between the two extreme cases described above a transition from low to high reflectance must occur. If we consider small wavelengths, the collection of free electrons starts to oscillate at the frequency of the incident waves. This oscillation of the electrons leads to an increase of the reflection. As the free

electrons can be described by a plasma, this phenomena is called plasma resonance. The shape and position of the spectral reflectance increase is of great importance for transparent conductive coatings, and is called the plasma resonance edge.

The *Drude model*, which was introduced by Paul Drude in 1900, describes the relationship between the electrical conductivity σ and the collision frequency ω_c for metals (see appendix B.2) [33]. The model combines the electrical field of the incident radiation as a driving force, with the equation of motion for electrons in a metal crystal. From this model Drude obtained a relationship between the static value of the conductivity σ_0 and the collision frequency ω_c [34]:

$$\omega_c = \frac{e^2 N}{m_e \sigma_0} \quad (2.5)$$

ω_c	collision frequency
e	electron charge
N	free electrons per unit volume
m_e	mass of electron
σ_0	static value of the conductivity

In thin films the collision frequency ω_c is so high that it is in the visible range. The plasma frequency ω_p which characterises the optical properties of bulk metals is less significant for thin films (see appendix B.3). Furthermore for thick metal layers, having nearly bulk material properties, the collision frequency ω_c is in the infrared and thus has no influence on the optical properties in the visible spectrum. Therefore, for increasing thickness of the layers, the collision frequency shifts from the ultraviolet, through the visible range, and into the infrared. However, with increasing thickness the transparency in the visible range is reduced, since the intensity of electromagnetic waves diminishes in matter.

The spectral properties of matter are determined by a fundamental, material specific quantity known as the complex refractive index \hat{n} :

$$\hat{n}(\lambda) = n(\lambda) + i k(\lambda) \quad (2.6)$$

\hat{n}	complex refractive index
n	real refractive index
k	extinction coefficient
λ	wavelength

In this equation n is the real refractive index and k is the extinction coefficient. The

real refractive index n is the ratio of the velocity v of an electromagnetic wave in the material to the velocity c_0 in vacuum:

$$n(\lambda) = \frac{c_0}{v(\lambda)} \quad (2.7)$$

c_0 speed of light in vacuum
 v speed of light in a material

The extinction coefficient k is a measure of the reduction of the amplitude of the electromagnetic wave during its propagation through matter. Both n and k depend on the wavelength λ of the electromagnetic wave. In the case of silver, the real refractive index is very small and the extinction coefficient increases rapidly with increasing wavelength. At $\lambda = 500$ nm, which is in the green region of the visible spectrum, the refractive index of a thin silver layer is:

$$\hat{n}(500 \text{ nm}) = 0.05 + i 3.5$$

This refractive index of thin silver films in the visible range is mainly determined by the high concentration of free electrons. Furthermore, the optical properties are determined by the structure and the surface roughness of the layers, as this influences the absorptance. In thin layers ($d \approx 20$ nm), which are not ideal (e.g., neither smooth nor uniform in thickness), both electrons and incident radiation are scattered at the interfaces of the separate crystalline structures, and at the surface of the coating. The scattering increases the absorptance, and therefore influences the refractive index \hat{n} .

The refractive index \hat{n} and the collision frequency ω_c are both influenced by structural defects and the surface roughness of the layers. Therefore it is important that thin metallic coatings must be sufficiently smooth and homogeneous in order to achieve a high transmittance in the visible, and a high reflectance in the infrared region of the spectra. When metal such as copper, gold or silver is deposited onto glass or any dielectric layer, the coating goes through a series of rather well defined growth stages before a uniform layer is formed [17]. Experimental analysis of these phenomena and measures to overcome these are described in chapter 5.1.1.

2.3 Optical Filters

Apart from the physical effects based on the properties of free electrons, modern transparent conductive coatings used for industrial applications make use of reflection and

anti-reflection effects based on interference of electromagnetic waves. By covering a thin silver layer with a low-absorptive dielectric layer, the spectral transmittance in the visible can be increased [35, 36]. This increase is based on the phenomena known as constructive and destructive interference. Interference is the superposition of two or more coherent waves that results in an increase or decrease of the amplitude of the waves. Constructive interference is, if the amplitude of the resulting wave is maximised. The prerequisite is that the waves are in phase, i.e., phase shift $\varphi = 0$. They cancel out each other and the amplitude is zero, if the waves have a phase shift of $\varphi = \pi$, which is called destructive interference. A phase shift between two waves is obtained by reflecting a percentage of the incoming wave at the boundaries of a thin film. The percent reflected depends on the material of the thin film, the material which surrounds it, and on the thickness of the film. This phenomena is described by the Fresnel equations which must be slightly modified to be valid for thin films.

2.3.1 Fresnel's Equations for Thin Films

The *Fresnel equations* are derived from Maxwell equations given in the appendix B.1. An electromagnetic wave, as the name implies, consists of an electric field component \vec{E} and a magnetic field component \vec{H} , that vary sinusoidal in strength. The electric and magnetic field are perpendicular to each other, and are also perpendicular to the direction of propagation of the wave, forming an orthogonal right-hand set. The simplest interference system consists of one boundary only, i.e., of an incident material and a single additional material into which the electromagnetic wave travels. At the boundary, the direction of propagation for the reflected wave is reversed, so the orientation of the electric and the magnetic field can not remain the same as in the incident beam, since the right handed set still must be valid. By convention, the orientation of the electric field is kept constant, and the magnetic field is changed [32, 37]. When oblique angles of incidence are considered, it is advisable to split an arbitrary polarised wave into two components. One component having the vectorial electric amplitude aligned (parallel) in the plane of incidence, p-polarised, and one having the vectorial electric amplitude perpendicular (senkrecht) to the plane of incidence, s-polarised.

Snell's law describes the change of angle of incidence θ when going from one material to another:

$$\hat{n}_0 \sin(\theta_0) = \hat{n}_1 \sin(\theta_1)$$

θ angle of incidence

In this equation the index 0 stands for the incoming material and 1 for the material into which the wave travels. The boundary condition for waves traversing across a boundary between two materials is that the components of the electric and the magnetic field along the boundary (tangential components) are continuous [32]. By applying these boundary conditions, the transmission t and reflection r coefficient can be calculated [37, 38, 39]. To simplify the equations two new quantities, the optical admittance η for parallel and perpendicular incidence, are introduced:

$$\eta_p = \frac{n - ik}{\cos(\theta)} \quad (2.8)$$

$$\eta_s = (n - ik) \cos(\theta) \quad (2.9)$$

η optical admittance

Thus, the amplitude coefficients t and r for transmission and reflection, respectively, are calculated to be:

$$t = \frac{2\eta_0}{\eta_0 + \eta_1}$$

$$r = \frac{\eta_0 - \eta_1}{\eta_0 + \eta_1}$$

t transmission coefficient

r reflection coefficient

The transmittance τ is defined as the ratio of the transmitted to the incident irradiance, and the reflectance ρ as the ratio of the reflected to the incident irradiance. This gives for oblique angles of incidence and absorbing materials

$$\tau = \frac{4\eta_0 \text{Re}(\eta_1)}{(\eta_0 + \eta_1)(\eta_0 + \eta_1)^*}$$

$$\rho = \left(\frac{\eta_0 - \eta_1}{\eta_0 + \eta_1} \right) \left(\frac{\eta_0 - \eta_1}{\eta_0 + \eta_1} \right)^*$$

τ transmittance

ρ reflectance

where * denotes complex conjugate. These equations are also true for non-absorbing materials where $k = 0$, and under this circumstance, the equations are greatly simplified.

It is easy to extend this analysis to the case of thin, plane, parallel films on a substrate. The presence of different interfaces means that a number of beams will be produced by

successive reflections, and the properties of the films will be determined by the summation of all these beams. In thin films, interference effects occur for the reflected and the transmitted light since the path difference of the beams is less than the coherence length of the light. For all the interfaces except the one between the substrate into which the wave travels and the last film, waves in the direction of incidence and waves in the opposite direction must be considered. As a wave travels through a layer of thickness d , the phase factor of the wave is changed by $\exp(i\delta)$ for waves travelling in the direction of incidence, and by $\exp(-i\delta)$ for waves moving in the opposite direction, where the phase thickness is:

$$\delta = \frac{2\pi\hat{n} d \cos(\theta)}{\lambda} \quad (2.10)$$

δ phase thickness

d layer thickness

Starting at the substrate the influence on the electric and magnetic components of a wave at each interface must be considered. This leads to the characteristic matrix of each thin film for each wavelength λ

$$\begin{pmatrix} E_a \\ H_a \end{pmatrix} = \begin{bmatrix} \cos(\delta) & \frac{i \sin(\delta)}{\eta_1} \\ i\eta_1 \sin(\delta) & \cos(\delta) \end{bmatrix} \cdot \begin{pmatrix} E_b \\ H_b \end{pmatrix}$$

E electric field component

H magnetic field component

the indices a and b denote the interfaces in the direction of propagation of the wave.

In general, an assembly of q layers is calculated by multiplying the individual matrices of each layer in the correct order

$$\begin{pmatrix} E_a \\ H_a \end{pmatrix} = \left\{ \prod_{r=1}^q \begin{bmatrix} \cos(\delta_r) & \frac{i \sin(\delta_r)}{\eta_r} \\ i\eta_r \sin(\delta_r) & \cos(\delta_r) \end{bmatrix} \right\} \cdot \begin{pmatrix} E_m \\ H_m \end{pmatrix}$$

where m denotes the emergent medium with $H_m = \eta_m E_m$, the phase thickness δ_r is as defined in equation 2.10 and the optical admittance η as defined in equations 2.9 or 2.8 for p- or s-polarised light, respectively. A more convenient form of the characteristic matrix of the assembly is defined as:

$$\begin{pmatrix} B \\ C \end{pmatrix} = \begin{pmatrix} \frac{E_a}{E_m} \\ \frac{H_a}{E_m} \end{pmatrix} = \left\{ \prod_{r=1}^q \begin{bmatrix} \cos(\delta_r) & \frac{i \sin(\delta_r)}{\eta_r} \\ i\eta_r \sin(\delta_r) & \cos(\delta_r) \end{bmatrix} \right\} \cdot \begin{pmatrix} 1 \\ \eta_m \end{pmatrix} \quad (2.11)$$

The amplitude reflection coefficient r and the reflectance ϱ are then defined as:

$$r = \frac{\eta_0 - \frac{C}{B}}{\eta_0 + \frac{C}{B}}$$

$$\varrho = \left(\frac{\eta_0 - \frac{C}{B}}{\eta_0 + \frac{C}{B}} \right) \cdot \left(\frac{\eta_0 - \frac{C}{B}}{\eta_0 + \frac{C}{B}} \right)^*$$

r	reflection coefficient
ϱ	reflectance
C, B	components of the characteristic matrix
η	optical admittance

If the incident medium is transparent, the transmittance τ and absorptance α of a multilayer can be calculated. The above derived equations give the transmittance into the last material, which is in general the glass substrate. If one wants to calculate the transmittance through a coated glass, the last layer with the index m has to be air. By calculating the irradiance I_k at the exit of the assembly, with k interfaces and the incoming irradiance I_i , the transmittance τ is defined as [37]:

$$\tau = \frac{I_k}{I_i} = \frac{\text{Re}(\eta_m) (1 - \varrho)}{\text{Re}(BC^*)}$$

τ	transmittance
I_i	incoming irradiance
I_k	outgoing irradiance

The absorptance α of the layer system can now be calculated, from the radiation distribution, equation 2.1:

$$\alpha = 1 - \varrho - \tau = (1 - \varrho) \left(1 - \frac{\text{Re}(\eta_m)}{\text{Re}(BC^*)} \right)$$

α	absorptance
----------	-------------

With these equations, the optical properties of every multilayer system can be calculated if the thicknesses and the optical constants n and k of each layer are known. Since these calculations must be done for all the wavelengths λ of interest, simulation programs are widely used for the development of thin film multilayer coatings. In order to simulate the optical properties, the material for each layer as well as the layer order must be evaluated. This choice is simplified through the use of optical standards like thin film filters.

2.4 Bandpass Filters

A huge variety of filters with different optical properties is known. The configuration of each optical filter is different, depending on the optical features it should provide. Optical filters having a region of high transmittance bounded on either side by a region of rejection, are called bandpass filters [37]. The simplest form of a bandpass filter is constructed by combining two edge filters, a long-wave and a short-wave pass filter. Long-wave pass filters reflect all the waves shorter than a desired wavelength, and short-wave pass filters reflect all waves having longer wavelengths. By adjusting or choosing the edges between the transmitting and reflecting zone of both filters, the width and the position of a bandpass filter can be varied. Optical filters in general are based on absorption, interference or a combination of both. The filters used for the development of coatings with the spectral transmittance τ_{min} , described in chapter 2.1, combine absorption and interference.

Edge filters based on interference are constructed by depositing a stack of thin films, consisting of two different materials, which should possess a high ratio of refractive indices [40]. The optical thickness of each layer has to be a quarter of the desired wavelength to be reflected ($d = \lambda/4$). The transmittance of such a filter is a series of high and low transmittance zones. The low zones have nearly zero transmittance, whereas the high zones can have up to 100% of transmittance. The explanation for those alternating transmittance zones is, that the thickness of a given layer is not quarter-wave for all wavelengths, especially if multi-reflection occur in one or more layers. It has to be kept in mind, that only quarter-wave layers or layers with an odd multiple of quarter-wave thickness ($d = (2m - 1)\lambda/4$) lead to destructive interference.

Another way to construct an edge filter is to use transparent conductive materials, semiconductor or metal, which have an intrinsic edge at the desired wavelength. The disadvantage of such a filter is, that it has high losses in the pass region due to a relative high reflectivity when the thickness is increased. A flexible filter with a deep rejection zone is best obtained by combining absorption and interference filters. This way the benefits of both filter types are used and some of the disadvantages like transmission side bands can even be removed.

The simplest way to create a bandpass filter is to combine two edge filters as already mentioned above. There are two ways to combine them: The first way is to deposit each filter on one side of the substrate, and these filters are called *double side* filters. In the second case, the *single side* filters, the layer stacks for the two edge filters are deposited on top of each other [41]. The development and the deposition is easier in the first case, since the two edge filters do not influence each other. In the second

case, a matching layer between the two filters is needed. By combining two edge filters, only broad bandpass filters can be created, as the required precision in positioning and the steepness of edges can not be achieved for narrow bandpass filters. To get narrow bandpass filters, the concept has to be changed slightly, and the principle of a Fabry-Perot interferometer has to be used.

A Fabry-Perot interferometer in general consists of two plane, parallel and reflecting surfaces separated by a distance d . This is obtained in thin film technology by a dielectric layer, the so called spacer, which is bound by two metallic reflecting layers, or by a stack of layers with a high reflectance [40, 42]. These two possibilities are shown schematically in figure 2.4. According to the materials they are constructed of, they are called metal-dielectric or all-dielectric bandpass filter, respectively.

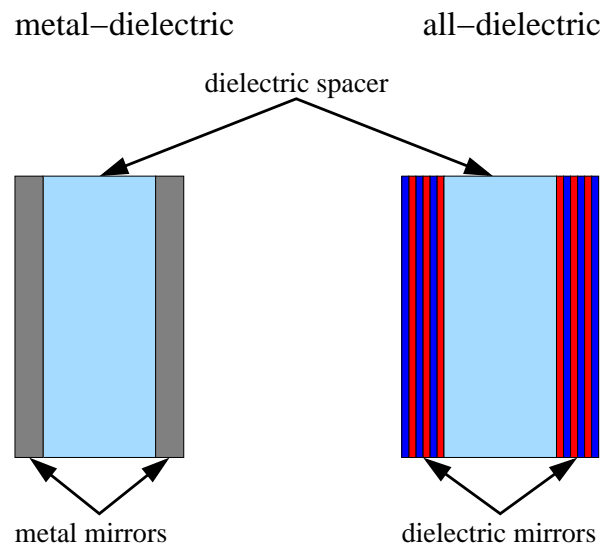


Figure 2.4: Schematic drawings of the two basic possibilities to make a Fabry-Perot filter with thin films. The one on the left hand side is made of two metal layers which are used as mirrors separated by a dielectric spacer. The one on the right hand side has in comparison dielectric multilayer stacks that act as mirrors separated by a thick dielectric spacer.

The optical properties of such thin film Fabry-Perot filters depend on the thickness and the refractive index of the spacer, the materials used for the mirrors and on the roughness of the interfaces between the different layers [42]. Mirrors of the all-dielectric filters must be constructed from stacks of quarter-wave layers. The materials used for the layers must have a large ratio of refractive indices, whereas the spacer must have a refractive index near unity. To obtain a high reflection, the outermost layers must have a high refractive index. In the case of metal-dielectric filters the metal layers must be protected against oxidation. For the protection, a thin dielectric layer is added on the outside [35]. This dielectric layer has another positive effect; it acts as a reflection-reducing layer and increases the transmittance of the filter [17].

By placing two or more filters in series, to form multiple cavity filters, the shape of the transmittance curve can be varied [40, 43]. If the new filter is made of two Fabry-Perot filters in series, as shown in figure 2.5, it is called a double cavity filter. The advantage of combining two filters is that the unique spectra of the constituent filters are superimposed. Using this process, the double peaked curve required for the spectral transmittance τ_{min} as described in chapter 2.1 can be achieved in theory.

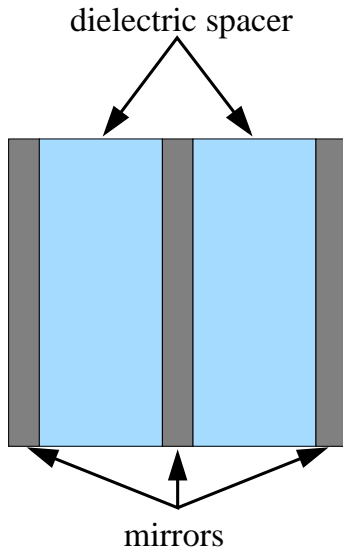


Figure 2.5: Schematic drawing of a double cavity filter, which consists of two Fabry-Perot filters which are placed in series.

Based on this, the spectral transmittance τ_{min} will be realised by using double cavity filters. There are two basic filter configurations; one is a simple metal-dielectric bandpass filter made of silver (Ag) and zinc oxide (ZnO). The other is an enhanced metal-dielectric bandpass filter consisting of silver (Ag) and two dielectric materials, titanium dioxide (TiO_2) and silicon dioxide (SiO_2). The reasons for and the advantages of these choices will be explained in the following sections.

Metal-dielectric filters were in general chosen, as they have the advantage of suppressing long wave sidebands, which are undesirable since they are in the infrared region of the spectrum. Metal mirrors typically utilise silver, copper or gold since they are transparent in the visible part of the spectrum [19, 44, 45]. Silver was chosen for the metal mirrors due to several reasons. Its absorption edge is at a wavelength of $\lambda = 300$ nm and therefore it is colour neutral over the entire visible spectrum [44, 46, 47]. Furthermore thin silver coatings stand out as the superior material on account of their low absorption of luminous and solar radiation [35, 47]. And finally the transmittance in the infrared range is nearly zero [36].

2.4.1 Bandpass Filters with ZnO and Ag

The basic layer sequence for the metal-dielectric bandpass filter based on silver (Ag) and zinc oxide (ZnO) is given in figure 2.6. The combination of silver with zinc oxide was chosen for this coating, since silver sandwiched between ZnO prevails a higher transmittance than if sandwiched between bismuth oxide (Bi_2O_3) layers, for example [45]. Zinc oxide in general has the advantage, that it is a wide band gap semiconductor (3.3 eV), which is transparent in the visible and the infrared spectrum [48, 49]. With $n = 1.88$ the refractive index of zinc oxide is high, in contrast to the low one of silver

with $n = 0.05$ [50]. Another advantage, which is more of industrial interest, ZnO has a high deposition rate if reactively sputtered with dc-power, and its chemical composition is easy to control [51].

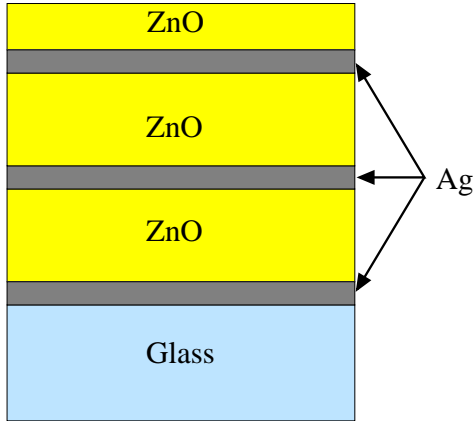


Figure 2.6: Schematic drawing of the double cavity filter, which was used for the realisation of the theoretical spectral transmittance τ_{min} described in chapter 2.1. The layer stack for the metal-dielectric filter is made of silver (Ag) and zinc oxide (ZnO). The thicknesses of the layers are arbitrary.

Compared to the standard double cavity filter given in figure 2.5 the glass substrate and a cover layer of zinc oxide on the last silver mirror were added. The covering zinc oxide layer was added because of the two reasons already mentioned: It should protect the silver layer against oxidation and it is used as an anti-reflecting coating to increase the total transmittance of the filter in the pass band [45]. The thickness of the different layers is subject to adjustments in order to achieve a transmittance which is equal to the desired spectral transmittance τ_{min} . The desired adjustments were done by simulations, which are described in detail in chapter 3.

2.4.2 Enhanced Bandpass Filters with TiO_2 , Ag and SiO_2

The second type of filters investigated in this thesis to realise the spectral transmittance τ_{min} is also a metal-dielectric double cavity filter. The standard filter design was modified since an extra dielectric layer was added to the sequence. The layer sequence is given in figure 2.7 with arbitrary thickness ratios. The idea behind this sequence is to build a multilayer-stack for the mirrors using two layers having high and low refractive indices, as used in the all-dielectric bandpass filters [40]. Instead of using two dielectric materials, silver was chosen for the one with the low refractive index material. Silver has a complex refractive index of $\hat{n} = 0.05 + i 3.5$ at the wavelength $\lambda = 500$ nm. Besides the low real

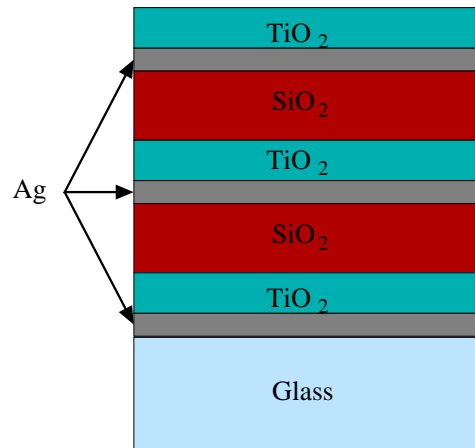


Figure 2.7: The enhanced bandpass filter is made of silver (Ag), titanium dioxide (TiO_2) and silicon dioxide (SiO_2). For achieving a filter with a spectral transmittance like τ_{min} the thickness of the layers, which are arbitrarily given here, were adjusted using a simulation.

refractive index it has the advantage of being electrically conductive and therefore is a good infrared mirror. As second material for the mirror a high index material is needed. For this titanium dioxide having a high refractive index of $n = 3.03$ at $\lambda = 500$ nm was used. This way the ratio of refractive indices of the two materials is high, and they should function as a good mirror. From literature it is known, that TiO_2 and Ag form an improved infrared mirror in combination with a high transmittance in the visible spectral rang [36, 39, 52]. The spacer of this Fabry-Perot filter is made of silicon dioxide, which has a refractive index of $n = 1.55$ at $\lambda = 500$ nm. This value lies between the refractive indices of silver and titanium dioxide used for the mirrors. Furthermore it is close to those of vacuum $n = 1$ and glass $n = 1.53$, which was one of the criteria of the spacer found by theory.

This filter combines the properties of both, a pure metal mirror and a mirror made of materials, which have a high ratio of refractive indices. The advantage of this design is that the silver cuts off the long wave sidebands of the interference filter in the transmittance. In this design the properties of the all-dielectric and the metal-dielectric bandpass filter are combined. This is the reason why it was named enhanced metal-dielectrical filter.

An additional advantage of splitting the mirror layers of the filter into two layers is, that the degree of freedom for the simulations is increased.

Chapter 3

Simulations

Developing a multilayer stack with a given transmittance, such as the spectral transmittance τ_{min} described in chapter 2.1, could be accomplished using the Fresnel equations and the characteristic matrix described in chapter 2.3. However, the analysis effort would be enormous, since the calculations must be repeated over a wide range of wavelengths to obtain a continuous spectrum over the design wavelengths (i.e., 250 nm to 2500 nm). Since multiple layers are required for this project, a closed form solution was abandoned in favour of a simulation program during the design phase of the coatings. As a result, the simulation program TFCalc from Software Spectra, Inc. was selected for modelling the coatings spectral response in this thesis.

3.1 From Theory to Real Multilayers

Before the simulations could be started, the theoretical spectral transmittance τ_{min} had to be translated into target transmittance values for the layer stack. The targets were determined by evaluating equation (2.4) for wavelengths between 250 nm and 800 nm in steps of 5 nm. Each of these values were entered in the target menu of TFCalc, with the same error tolerance i.e., the error tolerance is the inverse of the weighting factor. A decrease of the tolerance value forces the optimisation algorithm to reduce the difference between the target and computed transmittance values. During the development process, the tolerance values for selected targets were changed to obtain the desired steepness of the slopes defined by the spectral transmittance τ_{min} curve.

In addition to the transmittance targets, other targets focusing on the colour values of the transmitted and reflected light were defined. The colour target values also included small error tolerances to increase their weight in comparison to the great number of

transmittance targets. The colour targets were selected such that the colour of the reflected light outside the building is blue ($a < 0, b < 0$) and that the light transmitted is colour neutral ($a = 0, b = 0$). The colour blue for the reflected light was chosen as this is the architectural trend. Furthermore, the two colour criteria were required to be met for a wide range of incident angles.

The optical constants n and k of thin film materials differ from the values found in the literature. For example, the Palik database [53] values are obtained from bulk samples, and thin films have different properties due to surface scattering effects [54]. Furthermore the optical constants depend on the structure of the thin film as well as on the films underneath it. The structure of the films can be influenced by the operating pressure, the deposition power, the composition of background gases and other factors [55, 56, 57, 58]. It is therefore important to use the appropriate optical constants n and k for the multilayer simulations. The optical constants for the thin films were obtained by depositing known thicknesses (i.e., 20 nm to 100 nm) on silicon substrates and measuring the resulting properties using ellipsometry. The values for n and k of the deposited layers were obtained by fitting a model-system to the measured data (see chapter 4.3.3). This was done for all the layer materials used during the development. The optical constants determined by this method were stored in TFCalc as material files which were used in the simulations. Each material file includes the wavelength λ dependency of the n and k values.

The bandpass layer stacks developed in chapter 2.4 were entered in TFCalc as layer sequences for the simulations. The initial layer thicknesses were chosen arbitrary, but were based on realistic thickness ratios. An initial value of 15 nm was used for the silver layers. In contrast, the preliminary metallic oxide values were much thicker (40 nm).

After entering all the known data, the layer thicknesses were varied until the TFCalc program converged on a value that was within the tolerances defined by the target values for the spectral transmittance τ_{min} . There are three computational methods for varying the layer thicknesses. The first is the general search, where the simulation program varies the thicknesses of the individual layers until it finds a layer thickness combination that is within the error tolerance for the target values and the computed curve. In this mode the initial thickness values for the different layers are gradually changed to find an error minimum. In order to receive feasible layer systems with this search mode it is important to enter realistic thicknesses. The second is the global search, where the starting thickness values have minimal influence. In this case the program randomly assigns different thickness combinations and sorts them by the deviation from the target values. The number of iterations, and therefore the combinations is chosen as an input to the software. With this method, different

solutions are found, but they must be optimised by a general search mode. This optimisation often leads to the same result, as the global search finds several solutions near an error minimum. The last method is the manual search, where the thicknesses of the individual layers are changed by hand. This mode was used to make the final fine tuning of a coating layer, or to discover the relationship between material and thickness on a certain feature such as colour of the reflected or transmitted light.

3.2 Evaluation of the Simulated Multilayer Stacks

The above methods resulted in approximately seventy thickness combinations that met the target transmittance value and tolerance criteria. One example is given in figure 3.1 where the simulated transmittance (red line) is obviously not identical to the desired spectral transmittance τ_{min} (black dots). The main discrepancies between the target

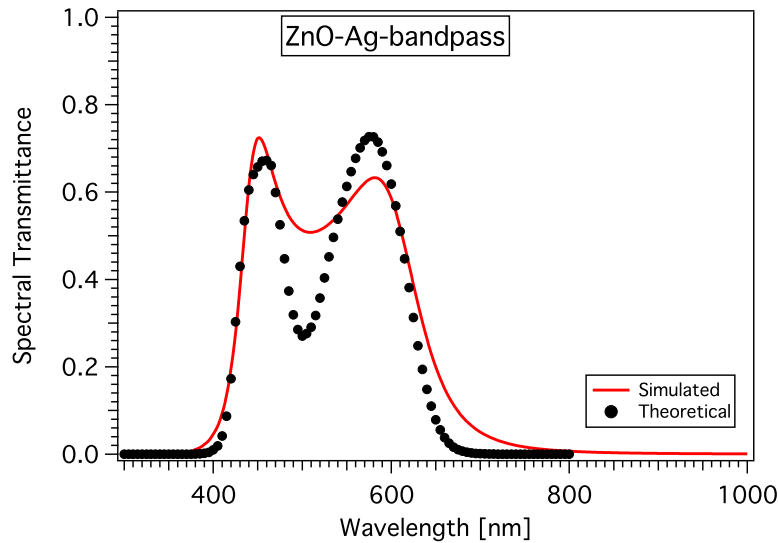


Figure 3.1: Comparison of the simulated transmittance (red curve) and the data entered in TFCalc as targets transmittance values. The simulation suggests that it is not possible to reach the steep edges if only nine layers are used.

transmittance values introduced in chapter 3.1 and the simulated transmittance are at the extreme points, specifically at the peaks and the dip in the middle. Although further adjustment is required, the energetic performance is an improvement compared to the sun protection glasses currently on the market. The energy load coefficient τ_e/τ_v of the simulated spectral transmittance is 0.36, which is less than the value of 0.429 for the best commercial sun protection glass, but not as low as the limit given by the theoretical spectral transmittance τ_{min} , which is 0.334.

In order to develop a commercially feasible layer stack, additional criteria were formulated in cooperation with the Glas Trösch AG (i.e., industrial research partner). The key point was that the ratio of the direct transmittance τ_e and the spectral transmittance τ_v , which is equal to the energy load coefficient τ_e/τ_v should be as closed as possible to the theoretical determined value of 0.334. This criterion is expected to be fulfilled if the simulated transmittance of the multilayer stack is close to the spectral transmittance τ_{min} . However the results of the simulations show that layer stacks containing nine or less different layers can not achieve a transmittance identical to the spectral transmittance τ_{min} . In order to achieve the steepness of the shoulders, additional layers would be needed. However, the thickness of the silver layers can not be reduced below 10 nm, as this represents the lower limit for achieving continuous films using current thin film deposition techniques (see chapter 5.1.1). The smallest value obtained with the simulations for the ratio τ_e/τ_v is 0.337; however, the above additional constraints, such as colour, were not fulfilled.

Another points were that the number of layers should not exceed nine and the total coating thickness should not exceed 200 nm. The nine layer limit was selected since industrial deposition plants have a limited number of cathodes and a single layer may require multiple cathodes (i.e., depending on the layer thickness and the material requirements). Since the goal of this thesis was to develop a commercially viable layer system, the number of layers had to be limited. Fortunately, layer stacks developed with the bandpass theory (see chapter 2.4) require less than nine layers.

Furthermore industrial experience has shown, that multilayer coatings with thicknesses over 200 nm often have stability problems such as poor adhesion and low scratch resistance. However, simulation results suggested that the total thickness must exceed 200 nm, if three silver layers are used. Therefore, to minimise the stability problems associated with stacks exceeding 200 nm, special measures must be introduced, such as “sticking” layers and a “hard covering” layer.

The other criteria focused on the calculated colour appearance of the transmitted and reflected light. Since simulations showed that the colour neutrality of the transmitted light defined in chapter 2.1 can not be reached by all designs, a range of tolerated colour values was defined. Colour coordinates of $|a| < 5$ and $|b| < 5$ were deemed acceptable for transmitted light at small angles of light incidence, since light with values in these ranges is still recognisable as nearly colour neutral by the human eye. Furthermore, colour coordinates of $b \leq 5$ were demanded regardless of the incident angle since the colour yellow is distracting if looked through the coated glass. The criteria for reflected light are that the hue of the colour must be constant with changing angles of incidence,

and the colour should be preferentially blue. In addition the reflected light should not contain any red component, thus $a < 0$.

Two multilayer stacks met both, the above criteria and the goal that the spectral transmittance should be $\tau_v \geq 0.5$. Each of these stacks were based on one of the bandpass previously described in chapter 2.4. These multilayer stacks were used as starting points for the experimental trails described in chapter 5.

3.3 Simulations for Optimisation during Deposition

During deposition, additional simulations were necessary to optimise the multilayer stack because the measured transmittance and reflectance of the deposited layers were not identical to the values predicted by the simulations. The reasons for this are manifold. As previously discussed, the optical constants n and k of the layers strongly depend on their structure and underlying layers. Another problem is determining the exact thickness of thin films, since the thickness can not be measured directly. Layer thickness is determined by measuring deposition rate and time. The deposition rate is calibrated by measuring the time required to deposit a thick layer. After deposition, the thickness is measured by scanning electron microscopy or ellipsometry, and the deposition rate can be calculated. This process would result in small errors if the growth rate of the films were constant for the entire deposition process. However, the growth rate is initially low, and the rate stabilises only after a closed layer of deposited material is formed. Another problem is that the deposition rate of the deposition target changes slowly with time. Since the thickness uncertainties are the same for all layers of one material during several deposition cycles, these errors can be compensated by multiplying the deposition rate of each material by a constant factor. This factor was determined by grouping layers of the same material in the simulation, and then changing the factor of each group until the layer stack had a transmittance that was identical to the measured spectrum of a deposited coating.

After the correct deposition rate for each material was determined, the optical results of coatings were adjusted by fine tuning the individual layer thicknesses. Two methods are available for this process. One is to adjust the layer thicknesses by making a new simulation with the corrected values. The other is to manually change the thicknesses of the layers in the simulation, until the desired transmittance and reflectance are achieved. The advantage of optimising the layer stacks during deposition is that changes are predicted and are carefully chosen. This results in a reduction of both, development time and costs.

Chapter 4

Experimental Methods

In this chapter an introduction to the methods used to characterise the different properties of the samples is given. Further the preparation of the samples is described.

4.1 Preparation of the Samples

The samples were prepared in different high vacuum deposition chambers. A schematic drawing of one of the deposition chambers is shown in the figure 4.1 which is connected

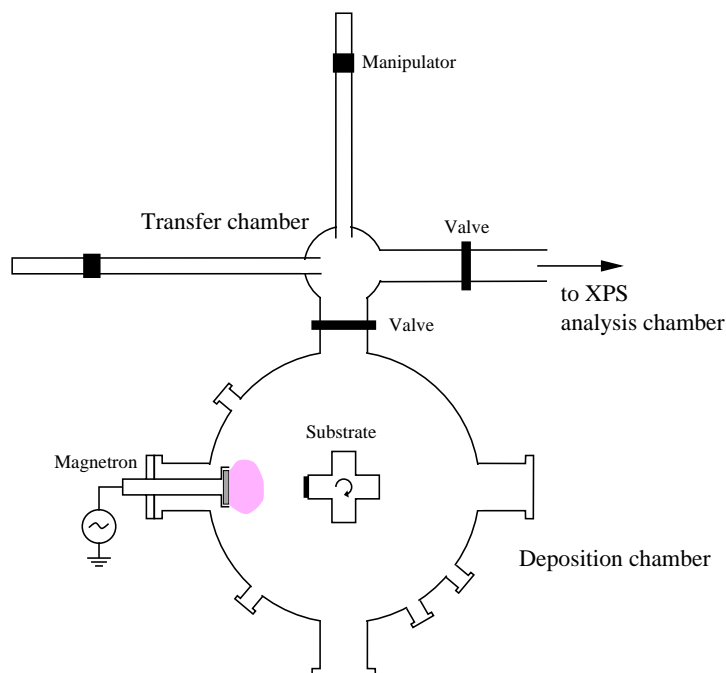


Figure 4.1: Schematic drawing of the transfer system and the deposition chamber. The samples are mounted in the middle of the chamber on a carousel. Due to the different flanges a variety of deposition sources and analyse systems can be mounted. The purple cloud shows the glow discharge of a magnetron during deposition.

through a transfer chamber with the analysis unit. The deposition and the transfer chamber are high vacuum (HV) systems, having a base pressure of $10^{-6} - 10^{-7}$ mbar. The deposition chamber is due to its different flanges very flexible concerning different deposition configurations. In the schematics only one magnetron is mounted, but other sources or the four-point probe could also be attached to it. The samples are positioned in the middle of the chamber on a carrousel and therefore they can be turned to face a deposition source or an analyse system.

The other sputter chamber used for coating of float glass was a laboratory in-line plant at Glas Trösch AG having a base pressure of 10^{-6} mbar. Here the substrate is moved past the deposition unit with a continuous speed. The general configuration and a schematic of an industrial in-line flat glass sputtering plant is given in figure 4.2, which is used for industrial coatings. The cathodes used for the deposition are slightly larger

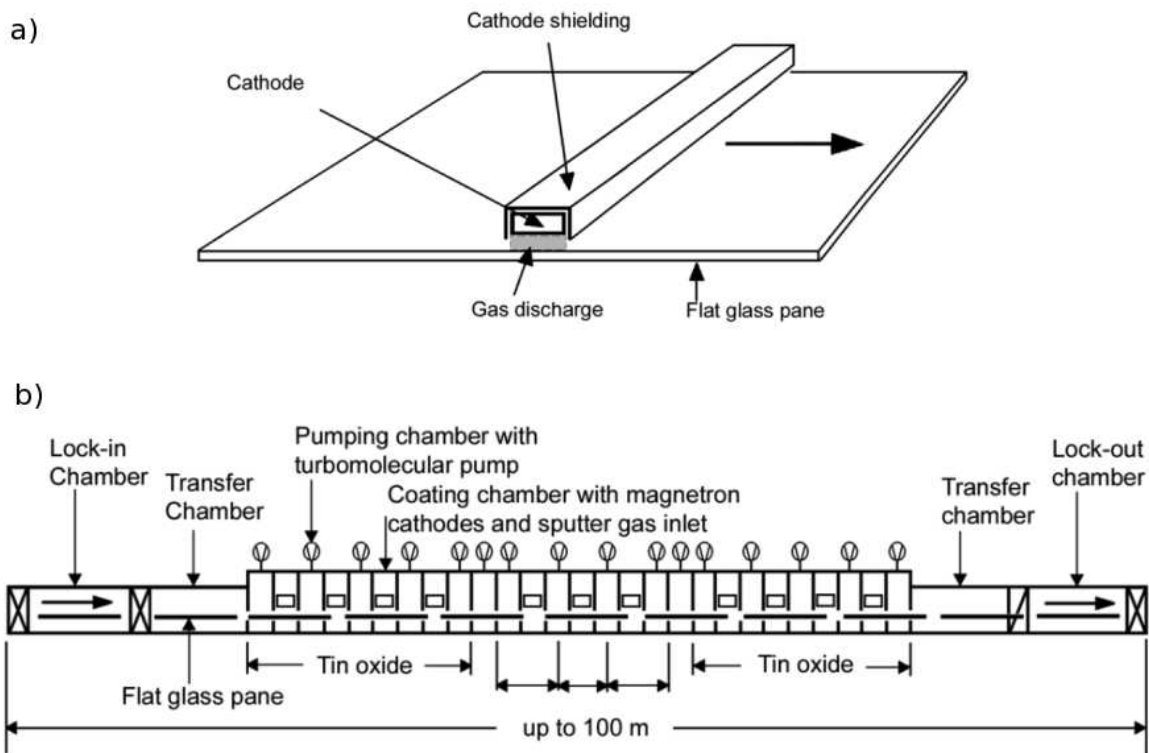


Figure 4.2: a) The principle of dynamic sputtering. The thickness of the deposited material is influenced by the velocity of the glass pane and the deposition rate of the cathode. b) Diagram of an in-line flat glass sputtering plant with magnetron cathodes. The float glass panes move from left to right [26].

than the panes are wide to make sure that the coating is homogenous over the whole area of the glass pane. Between the cathodes containing different materials a pumping unit is mounted to prevent intermixing of the components. A picture of the laboratory in-line plant is shown in figure 4.3.



Figure 4.3: Laboratory in-line plant of the Glas Trösch AG. The glass panes enter the in-line plant on the right side and are moved vertically past the different cathodes for the deposition of the different layers. Each cathode contains a different material. The whole in-line plant has five cathodes.

4.1.1 Different Substrates

Depending on the method used for the characterisation of the optical properties and the growth mechanism of the thin films different substrates were used. The layers that were investigated by photoelectron spectroscopy (see chapter 4.2) and by spectral ellipsometry (see chapter 4.3.3) were deposited on silicon substrates. These substrates were cut out of polished silicon wafers having a (100) lattice orientation. The surface of the wafer is nearly atomically flat on the polished side, this is necessary to be able to deposited flat and homogeneous thin films. Further the silicon substrates are covered with a native oxide film of 2 nm thickness. For photoelectron spectroscopy measurements silicon substrates were used, as it is important to have a good conductivity to avoid charging of the sample. If charging occurs the interpretation of the results is difficult and sometimes even impossible, since the spectra shift is arbitrarily and the positions of the peaks are no longer identical to those given in literature. For spectral ellipsometry it is advisable to have clear and flat interfaces, especially between the substrate and the layers. Further it is important to have a substrate, that is opaque for the wavelength range under investigation. The silicon substrates were cleaned before the deposition in an ultra sonic bath first with acetone and than with ethanol for about ten minutes each. After this chemical cleaning the rests of the solvents were removed by blowing the sample with nitrogen.

For the transmission and reflection measurements the thin layers were deposited on different glass substrates. The glass substrates used were either laboratory glass substrate AF45 from the Präzisions Glas & Optik GmbH of the size $(40 \times 40 \times 0.55)$ mm³ or float glass $(60 \times 100 \times 0.4)$ cm³ produced by the Glas Trösch AG. Both glass substrates were cleaned before the deposition. The AF45 were cleaned with the same ultrasonic treatment as described for the silicon substrates. The float glass was mechanical cleaned with distilled water in a commercial glass cleaning plant [26].

4.1.2 Magnetron Sputtering Deposition

The deposition technique chosen for the thin layers in the multilayer stacks was sputtering, since this has gained greater importance economically than any other flat glass coating technique in use nowadays. World-wide, several 100 million m² of flat glass are coated each year by sputtering and this amount is still increasing [26]. The general setup for sputtering deposition is shown in figure 4.4. It consists of a target, the material that should be deposited, a substrate and a sputtering gas, most of the times argon. The target is negatively charged by a dc power supply so that an electric field

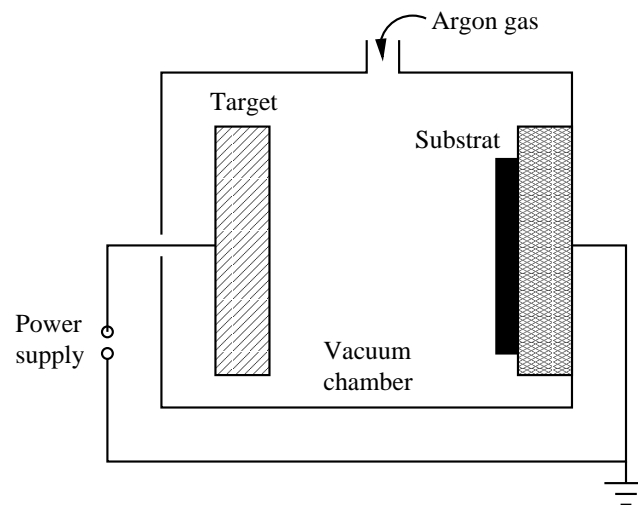


Figure 4.4: Schematic drawing of a general arrangement for sputter depositions. In the easiest case the target is charged by a high negative voltage and therefore acts as a cathode. Whereas the substrate, which is grounded, works as anode. Argon is used as sputtering gas [59].

builds up between the target and the substrate, which is grounded. The electric field is needed to accelerate electrons which in turn collide with argon atoms, breaking some of them up into argon ions and more electrons to produce a glow discharge. The charged particles thus produced are accelerated by the electric field, the electrons tending towards the anode (substrate) causing more ionisation on their way and the argon ions towards the cathode, the target. From the target due to the bombardment with the

argon ions atoms are ejected. The atoms are ejected in random directions and therefore can strike and condensate on the surface of the substrate or on the walls of the vacuum chamber [59].

With this technique all kind of thin films can be produced. The easiest way is to sputter metallic films as only a target of the metal which should be deposited is needed. Metallic compounds like oxides or nitrides can be deposited by reactive sputtering. In this method a metal target is sputtered in a gas mixture containing argon, as sputtering gas, and other gases like oxygen or nitrogen as reactive gasses. The atoms ejected from the target react chemically with the reaction gases on their way to the substrate or the chamber walls.

Another method to deposit insulating films from targets, that are weakly conductive or insulating, is to use rf sputtering (radio frequency sputtering). Here a power supply is used that alternates the voltage at a frequency of approximately 10 MHz, so that the target is alternately bombarded by ions and electrons to avoid that the target is getting charged and rejects the incoming argon ions. Due to their huge mass the ions can not follow the rf frequency and are accelerated towards the target. The electrons are light enough to follow the rf frequency and neutralise the charge building up on the target. A charging of the target would lead to a break down of the glow discharge and with it the deposition would also stop.

For the deposition of the thin films investigated in this work magnetically enhanced sputtering systems, so called magnetrons, were used. By using a magnetic field the efficiency of the electrons in ionising the argon atoms is increased by trapping the electrons near the target. A schematic drawing of the configuration of a planar magnetron, as used in the in-line deposition chamber, is given in figure 4.5. This figure also shows a picture of two magnetrons in operation. In some of the experiments performed the targets and the magnets were circular and not rectangular as in figure 4.5 shown, but the principle is the same. The magnets are located behind the target and cause a racetrack or ring shaped erosion zone. The advantage of magnetrons is, that the deposition rate is higher, they work at lower pressures and the deposition is focused mainly in one direction. Due to this the deposition rate is increased when using the same power to drive the magnetron, if the substrate is positioned in the sputtering direction. The disadvantage of magnetron sputtering is, that the erosion is localised due to the magnetic field lines, which causes the deposition rate to vary with operation time, and that only a small part of the target is used.

The targets used to deposit the thin films in this work, were titanium, silicon, silver, zinc and SiSPA (80 – 95% silicon and 5 – 20% aluminium) which were sputtered with

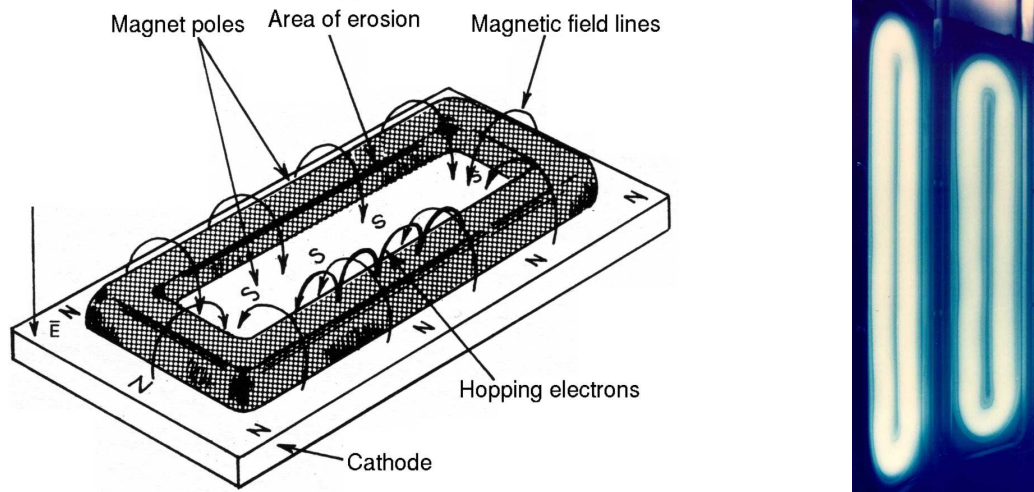


Figure 4.5: On the left hand side a schematic drawing of a planar magnetron sputtering configuration is shown [59]. The cathode is the target. The magnets are located under the cathode and are not shown. The dark grey part shows the glow discharge which is located over the area of erosion. On the right hand side a picture of two magnetrons in operation is shown [60].

argon as sputtering gas. If an oxide or a nitride layer was sputtered oxygen or nitrogen gas, respectively, was let in the chamber controlled by mass-flow controllers. For the power supplies dc, pulsed-dc and rf generators were used.

4.1.3 Thickness Monitoring

The thickness of the deposited layers was determined during the deposition by a quartz crystal microbalance or by the deposition time, if the deposition rate was known. To control, if the determined thicknesses correspond to reality, a thick layer was deposited and then the thickness was determined by ellipsometry or scanning electron microscopy measurements as described later in this chapter. The thickness determined this way was used to calibrate the deposition time or to find a calibration factor for the quartz crystal microbalance.

With the quartz crystal microbalance the deposited thickness can not be measured directly. Instead the fundamental frequency ν of a quartz crystal is measured. This frequency depends on the amount of material deposited on the quartz crystal. By measuring the frequency ν the deposited thickness T can be calculated by using the *Sauerbrey equation* [61]:

$$T = \left(\frac{N_q \rho_q}{\rho_f \nu_q^2} \right) (\nu_c - \nu_q)$$

T	film thickness (cm/s)
N_q	frequency constant for AT-cut quartz crystal (Hz cm)
ρ_q	density of quartz (g/cm ³)
ρ_f	density of film (g/cm ³)
ν_q	oscillation frequency for uncoated quartz (Hz)
ν_c	oscillation frequency for coated quartz (Hz)

The oscillation of the quartz is measured by a frequency counter (HP 5334B), which is connected to a computer via GPIB interface. An in-house written labview program is used to read out and plot the data. Like this the deposition rate and the stability of the deposition can be determined and controlled.

4.2 Photoelectron Spectroscopy

Photoelectron spectroscopy (PES), also called Electron Spectroscopy for Chemical Analysis (ESCA), is an old experimental technique, which is nowadays in principle performed in the same way as hundred years ago. It is based on the photoelectric effect which was detected by Heinrich Rudolf Hertz in 1887 [62] and was 1905 mathematically described by Albert Einstein, for which Einstein got the Nobel Prize in 1921 [63]. The *photoelectric effect* describes that photons of radiation, that are focused on the sample, excite electrons in the sample, which are then emitted. This is only the case, if the energy of the photons is higher than the work function Φ of the specific material under investigation. The kinetic energy of the ejected electrons is then determined by an electrostatic analyser. The energy of the impinging photon $h\nu$, the kinetic energy of the photoelectron E_{kin} and the work function Φ of the sample are connected to the binding energy E_B of the electron through the following relation [64, 65]:

$$E_B = h\nu - \Phi - E_{kin}$$

E_B	binding energy
h	Planck constant
ν	frequency of the photon
Φ	work function
E_{kin}	kinetic energy of the photoelectrons

The principle setup of a PES experiment is depicted in figure 4.6. The photon source can either be a gas discharge lamp, an X-ray tube or a synchrotron radiation source. By using an X-ray tube as photon source K. Siegbahn was able to perform high resolution electron spectroscopy [66]. This was awarded with the Nobel Prize in the year 1981.

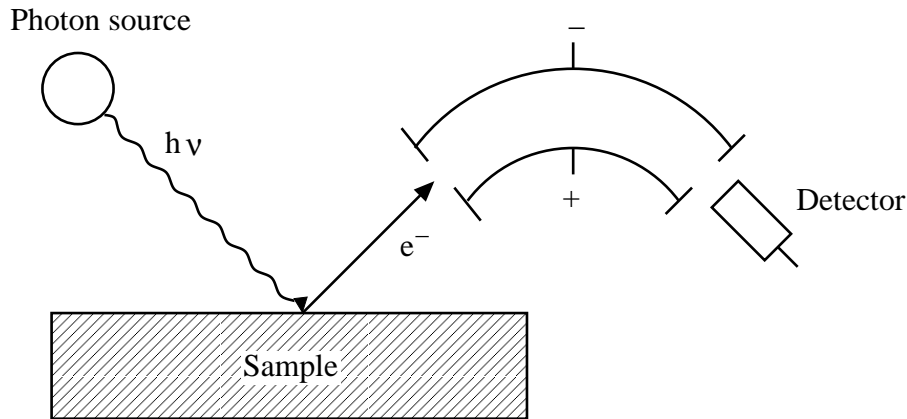


Figure 4.6: Schematic drawing of a photoelectron spectroscopy experiment. The photon source can be a gas discharge lamp, an X-ray tube or a synchrotron radiation source. The electrons are detected by an electrostatic analyser [65].

The important parameter which is measured is the kinetic energy of the photoemitted electrons. If the energy distribution of the emitted electrons is plotted as shown in figure 4.7, their number per energy interval gives a replica of the electron energy distribution in the solid under investigation. This is an attractive feature of PES, and this can be used to obtain different kinds of information, like the electronic structure, chemical bonds, elemental compositions, conductivity and others.

Solid samples have two main electronic features, the core levels and the valence band. The core levels are the electrons in the inner shells of the atom and the valence band are the electrons in the outermost shell, which can freely move and give rise to conductivity. In metals the Fermi energy E_F is at the top of the valence band, as shown in figure 4.7, and has a separation Φ from the vacuum level E_{vac} . The Fermi energy is taken in solids as the natural zero. Figure 4.7 shows schematically the relation between the energy-levels diagram of the sample and the energy distribution spectrum of photoemitted electrons. If photo absorption takes place in a core level with binding energy E_B the photoelectrons can be detected with a kinetic energy $E_{kin} = h\nu - \Phi - E_B$ in the vacuum. Although the physical reference in solids is E_F , the kinetic energy of the electrons in vacuum is measured in respect to the vacuum level E_{vac} . For the interpretation of photoelectron experiments the three-step model has proven to be extremely useful. This model breaks the PES experiment into three steps:

1. The photon is absorbed by the solid and an electron is excited.
2. This excited electron travels through the solid to the surface.
3. After travelling through the solid the electron escapes through the surface into vacuum where it is detected.

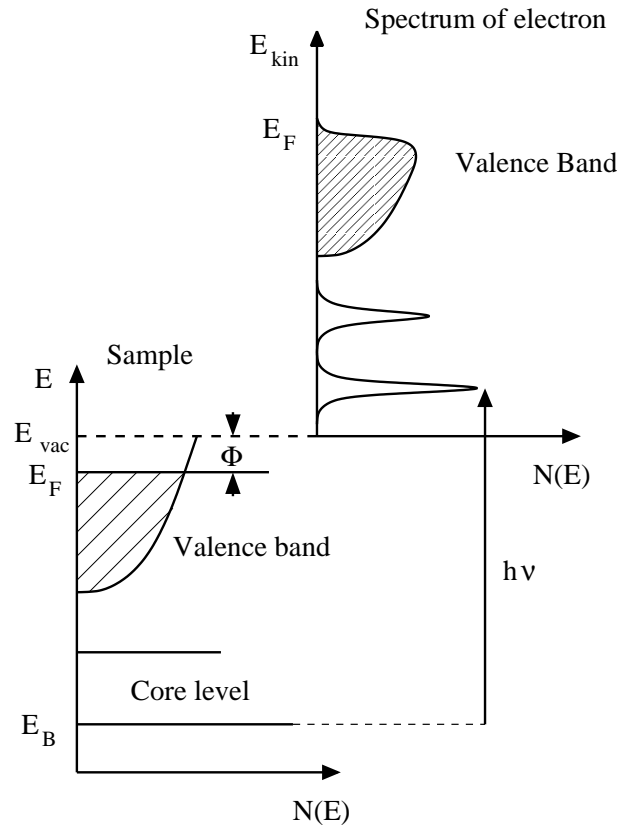


Figure 4.7: Relation between the energy levels in a solid sample and the electron energy distribution spectrum produced by photons of energy $h\nu$. E_B is the binding energy of the electrons, which in solids is referred to the Fermi level E_F [65].

One important parameter of photoelectron spectroscopy is the electron escape depth. It determines the distance perpendicular to the surface of the sample for which photoelectrons still manage to penetrate to the surface with a high enough energy to reach the analyser and to be counted. Electrons travelling through a solid encounter electron-electron and electron-phonon collisions. The energy lost due to these collisions is proportional to the dielectric function $\varepsilon(\omega)$, which is a characteristic property of every material. So the escape depth depends on the material under investigation and is only of the order of a few Ångström [65]. This means that a spectrum of a solid measured by PES only involves electrons from a very thin layer at the surface of the sample. Due to this circumstance photoelectron spectroscopy is a surface sensitive method.

The region of the spectrum, presented in figure 4.7, which ought to be investigated in detail can be chosen by changing the photon source. Using photons of the ultraviolet region (UPS), having energies of 5 eV to 100 eV, the features of the valence-band can be measured with a high sensitivity and a high resolution. For this usually helium discharge lamps are used. To study the core-level region and the valence-band a source is used, which provides high energetic photons in the X-ray region (XPS), with ener-

gies of several hundred to thousand eV. However the resolution is about one order of magnitude worse than that of UPS. The advantage of XPS is that a very large number of core-levels are accessible, and thus makes it an useful technique in many fields, like chemistry and material science.

When solids are investigated it is of interest to find out in which chemical state the atoms in the solid are. This can be done by measuring the changes in binding energy, this difference is called the chemical shift. If the metal state and an oxide of the same element are compared, this chemical shift can be easily explained by using a very simplified model. In the metal the electrons of the outermost shell form a band, the valance band. In the valance band the wave function of the electrons is only partly located at the site of a particular atom. In the oxide each atom donates his outermost electrons to the oxygen atoms. Therefore the outermost electrons have no part of their wave function near the metal atom. So the electrons in the inner shells of the atom in the oxide case see a stronger Coulomb interaction than in the metallic case. This leads to a higher binding energy of the electrons in the inner shells in the oxide than in the metal and a chemical shift between the two compounds is observed. This is not only valid for oxides, but also for all other chemical and structural changes, but the sign and the value of the shift are different for every electron configuration and therefore for every material.

PES Setup

The PES setup (Leybold EA10N) used for the measurements is given in figure 4.8. It is connected through a transfer system with the deposition chamber. Connecting the deposition chamber with the analyse chamber has the advantage that the sample stays under vacuum conditions. This makes it possible to measure the surface as it was deposited without being contaminated. The PES analyse chamber is an ultra high vacuum (UHV) chamber in comparison to the deposition and the transfer chamber, with a base pressure of $2 \cdot 10^{-10}$ mbar. For the XPS measurements a Mg K_α photon source¹ with photon energy of $h\nu = 1253.6$ eV was used. Additionally, for the UPS-measurements a helium-discharge lamp with photon energies of $h\nu_{\text{HeI}} = 21.2$ eV was available. For the calibration of the binding energy the $4f$ doublet, due to spin-orbit coupling, of a clean gold sample was measured. The $4f_{7/2}$ line of gold has a binding energy of 84.0 eV.

The electron detection consists of a hemispherical energy analyser and a multichannel electron detector. The hemispherical analyser performs the spectroscopic energy mea-

¹Characteristic line of the X-ray spectrum of magnesium (K_α -line)

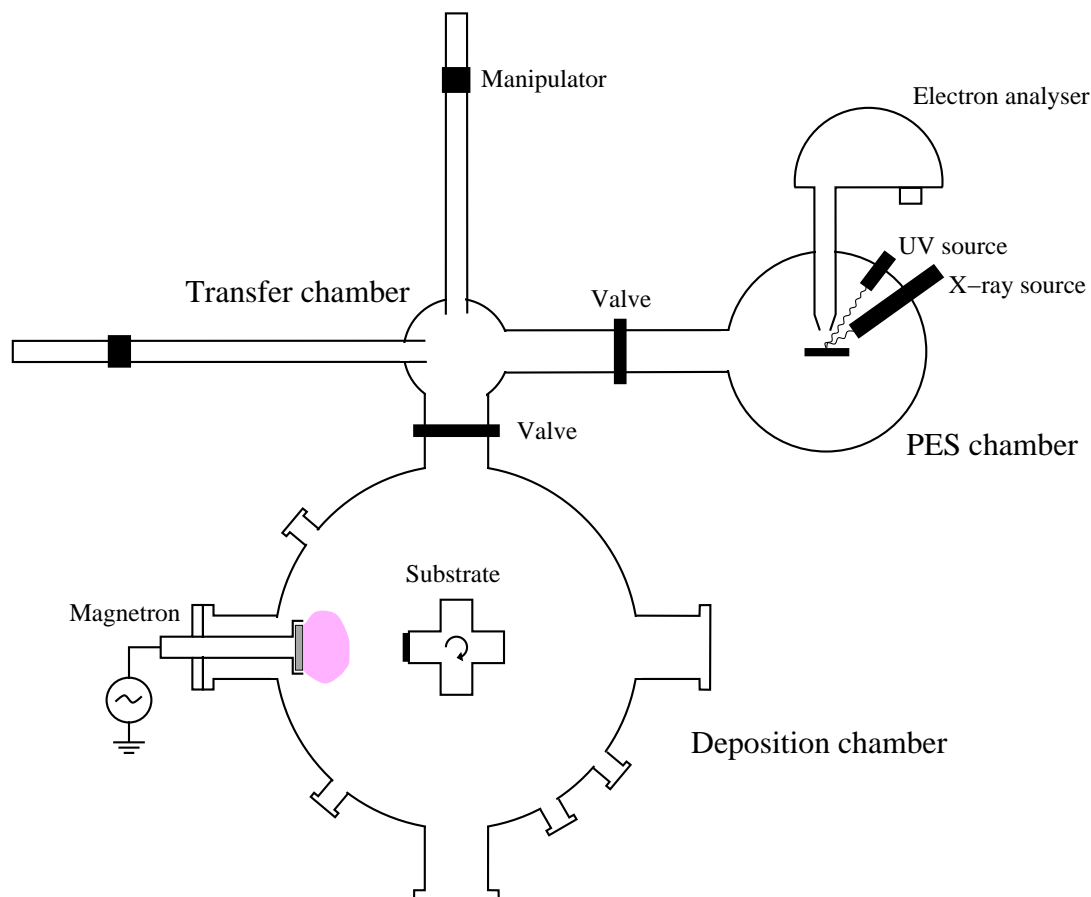


Figure 4.8: Schematic drawing of the PES analysis chamber, the transfer system and the deposition chamber. The PES chamber contains two photon sources, an X-ray and an UV source, and the electron analyser. The deposition chamber was described in chapter 4.1

surement, due to energy dispersion. The emitted electrons enter the analyser through an entrance slit and are then deflected to elliptical trajectories by the radial electric field between the outer and inner hemisphere. Only particles with kinetic energy in a certain energy interval are able to pass the full deflection angle to the exit slit and will be counted by the detector.

For some of the measurements a different PES setup was used a VG ESCA-LAB 210 system, which will be referenced by ESCA III. The general setup of both photoelectron spectrometers is very similar. They both consist of a deposition chamber which is connected by a transfer chamber to the main analyse unite. One of the important differences is that the deposition chamber of ESCA III is a ultra high vacuum (UHV) chamber with a background pressure of around $2 \cdot 10^{-8}$ mbar. The other difference is that the photon source is a monochromatic Al K_{α} photon source² with a photon energy of $h\nu = 1486.6$ eV. The advantage of using a monochromatic X-ray source is that the resolution is higher compared to measurements with non-monochromatic X-rays.

²Characteristic line of the X-ray spectrum of aluminium (K_{α} -line)

4.3 Optical Measurements

To determine the optical properties, like transmittance and reflectance of thin films and multilayer stacks or the optical constants n and k of thin films different optical measurement techniques were used.

4.3.1 Spectrophotometer

Transmission and reflectivity measurements are carried out using the UV–Vis–IR-spectrophotometer³ *Cary 5* from Varian. The measuring range of this spectrophotometer is 250 nm to 2500 nm. It is equipped with an Ulbricht sphere⁴ with a diameter of 110 mm, which is coated from the inside with PTFE (Poly Tetra Fluoro Ethylene, known as Teflon). PTFE is used as it has a high, nearly 100%, reflectance over the working wavelength range of the spectrophotometer and it is assumed to have a perfect lambertian diffuse reflectivity.

A standard PTFE sample with a known reflectance is used to calibrate the system to be able to give absolute values. The calibration is done in two steps. First the background intensity $I_{background}$ is measured, by blocking the entrance slit of the Ulbricht sphere. In the second step the intensity $I_{reference}$ with the PTFE reference plate mounted on the sample port for reflectance measurements is determined. The measured signal of a sample is then calibrated by the following formula [67]:

$$\varrho(\lambda) = C(\lambda) \cdot \frac{I_{sample} - I_{background}}{I_{reference} - I_{background}}$$

$\varrho(\lambda)$	wavelength dependent reflectance
$C(\lambda)$	absolute reflectance of the PTFE reference
I_{sample}	measured signal
$I_{background}$	background intensity
$I_{reference}$	intensity with the PTFE reference plate

The same equation is valid for the transmittance. For transmittance measurements the sample is mounted in front of the entrance slit, in the case of reflectance measurements the sample is mounted on the opposite side of the Ulbricht sphere facing the entrance slit.

³ultraviolet–visible–infrared

⁴An Ulbricht sphere is a hollow sphere with a diffusely reflecting internal surface, with two small openings (ports) for introducing light. The arrangement causes many diffuse reflections of the introduced light before it reaches a detector, so that the light flux becomes very uniform at the detector, and nearly independent of the spatial and polarisation properties of the introduced light.

4.3.2 Window Stand

For the development of coatings for architectural applications it is important to know the changes of the transmittance and reflectance for different incident angles of the light. It is also important to know these values of existing sun protection insulating glasses. Knowing the transmittance and the reflectance, the energetic properties and the colour changes can be calculated. To measure commercial sized (60 cm × 120 cm) insulating glasses a new measuring setup was developed at the University of Basel by R. Steiner and P. Oelhafen [22]. In figure 4.9 the general setup used to investigate commercial insulating glasses is shown.

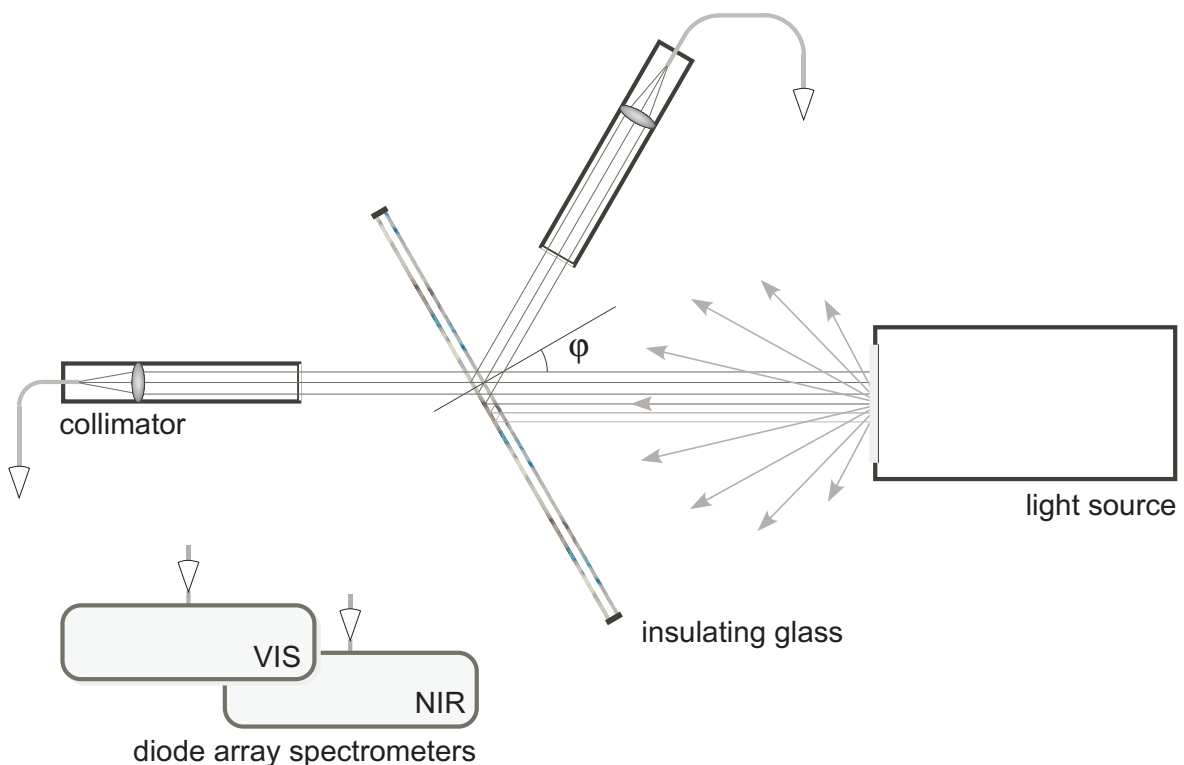


Figure 4.9: Schematic drawing of the measuring stand used to determine the optical properties angle dependent of insulating glasses [22].

For the sizes of commercial insulating glasses an Ulbricht sphere is not feasible, which is necessary to also take the light into account that was internally reflected in the insulating glass. Another reason is to measure all the components of the light since light is scattered in all directions if the surface is not atomically flat. To overcome these problems the principle was inverted. The light source in this setup sends diffuse light and the collimator only focuses the light that enters parallel on the quartz fiber bundle attached to it. The quartz fiber is connected to an ultra violet to visible and a near infrared diode array spectrometer. For measuring the angle dependance of the transmittance the collimator and the light source are aligned and the insulating glass

is rotated about given angles. In the case of reflectance measurements the collimator and the insulating glass is moved, due to the fact that the reflection angle changes simultaneously with the incident angle (i.e., the angle of incidence is equal to the angle of emergence) [22].

With this experimental setup the transmittance and the reflectance, taking also into account the internal reflectance between the two glass panes, can be measured for the wavelength range 350 nm to 1650 nm and angles of incidence of 0° to 75° or 15° to 75° for transmittance and reflectance, respectively. The calibration for the reflectance is done with a SiO_2 coated aluminium reference mirror with a known reflectance. By adapting the sample holder also samples down to the size of $5 \text{ cm} \times 10 \text{ cm}$ could be measured for several angles of incidence.

For the window stand the reproducibility of the measured spectral transmittance and reflectance data is of the order of $\pm 3 \cdot 10^{-3}$. This leads to absolute accuracies of the spectral transmittance and reflectance values of $\pm 7.5 \cdot 10^{-3}$ and $\pm 1.5 \cdot 10^{-2}$, respectively [22].

4.3.3 Spectral Ellipsometry

Ellipsometry is a reflectance measurement using polarised radiation to get the ratio of reflectance in the selected direction perpendicular (r_s) and parallel (r_p) to the plane of incidence and difference of phase ($\delta_p - \delta_s$), that is connected with the reflection. This gives the possibility to derive the complex dielectric constant or the thickness of the layer or even the combination of both.

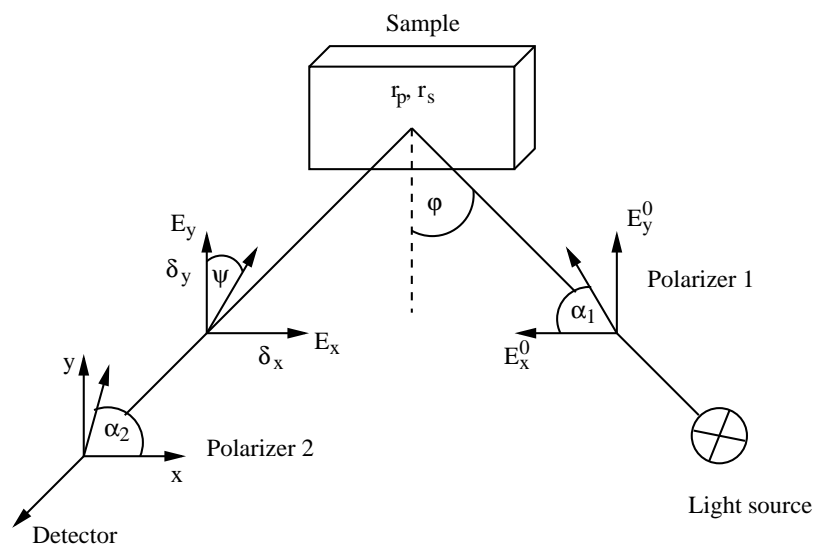


Figure 4.10: Basic arrangements of a spectral ellipsometer showing the components of the electrical field and the different angles needed to describe the changes [68].

The schematic arrangement of a photometrical ellipsometer is given in figure 4.10. An ellipsometer uses a polariser between the sample and the light source to generate linearly polarised light. A second polariser is mounted between the sample and the detector and is called analyser. The first polariser is fixed whereas the second is rotating around the optical axis. The intensity flux is observed which passed the analyser in dependence of the azimuth angle with a suitable detector.

For the evaluation of data measured by ellipsometry, the two ellipsometric parameters $\tan(\psi)$ and Δ are defined. They are connected to the ratio of the reflection coefficients for parallel (p) and perpendicular (s) polarisation. This ratio can be written in general as [68]:

$$\begin{aligned}\varrho &= \frac{r_p}{r_s} \\ \varrho &= \frac{|r_p|}{|r_s|} \exp(i(\delta_p - \delta_s)) \\ \varrho &= \tan(\psi) \exp(i \Delta)\end{aligned}$$

r_p	reflection coefficient with parallel polarisation (p)
r_s	reflection coefficient with perpendicular polarisation (s)
δ	phase of the light
$\tan(\psi)$	relative attenuation of the p- and s-polarised components
Δ	relative phase shift

Thus the relative attenuation of the p- and s-polarised components are represented by $\tan(\psi)$ and the relative phase shift introduced by the reflection on the surface by Δ , or in detail:

$$\begin{aligned}\tan(\psi) &= \frac{|r_p|}{|r_s|} \\ \Delta &= (\delta_p - \delta_s)\end{aligned}$$

If thin layers or a multilayer system on a substrate are investigated the optical constants can not be calculated directly from the measured ratio ϱ . Instead, the optical properties have to be determined by fitting Δ and ψ of an optical model iteratively to the measured data. But one has to keep in mind that not every model which fits the measured data corresponds to the reality.

The ellipsometer used for the measurements is a *Variable Angle Spectroscopic Ellipsometer* (VASE), a SE800/850 from SENTECH Instruments GmbH. It is equipped with a xenon lamp and a CCD spectrometer for measurements in the visible and a

Fourier transform spectrometer for the near infrared. The total wavelength range is therefore 350 nm – 2300 nm. The angle of incidence can be varied between 40° and 80°.

4.4 Resistivity Measurements

The optical properties of a thin film system depend on the quantities electrical conductivity σ and mobility μ of the electrons as described in chapter 2.2. Therefore measuring the resistivity ϱ , the reciprocal of the conductivity σ , gives clues concerning the optical properties, i.e., metal or oxide, of the thin film system. If a variation of resistance is found changes to the optical properties can be predicted. The resistance of thin films can not be measured directly, as it depends on the thickness of the film. Instead the sheet resistance R_{\square} is determined by measurements. The sheet resistance R_{\square} describes the resistance of a current that flows along the plane of the sheet and not perpendicular to it. To measure it the four-point method, which is schematically shown in figure 4.11, was used. It consists of four electrodes, which are aligned in one row and

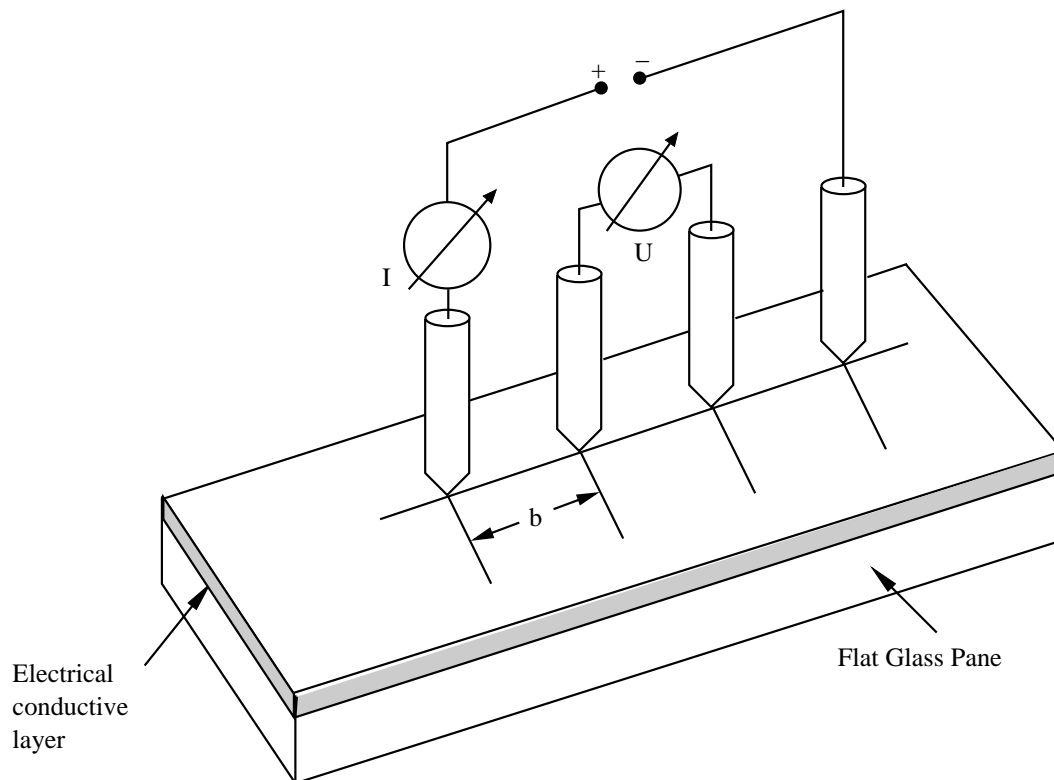


Figure 4.11: Schematic drawing of a four-point method to determine the sheet resistance R_{\square} of thin layers [26].

are separated by the distance b , which is constant for all four electrodes. Through the outer two electrodes a current I is running, while the inner two electrodes measure the

voltage U . The sheet resistance is connected to the conductivity σ and the resistivity ϱ through the following equation [26]:

$$R_{\square} = \frac{\varrho}{d} = \frac{1}{\sigma d}$$

In order to get a relation between the measured quantities current I and voltage U it is necessary to investigate the resistivity ϱ of the four-point method. When the probes are placed on a material of semi-infinite volume, the resistivity is given by [69, 70, 71]:

$$\varrho = \frac{U}{I} \cdot \frac{2\pi}{\frac{1}{b_1} + \frac{1}{b_3} - \frac{1}{b_1+b_2} - \frac{1}{b_2+b_3}}$$

U measured voltage

I measured current

b_i distance between the different probes

If $b_1 = b_2 = b_3 = b$, the equation simplifies to:

$$\varrho = \frac{U}{I} \cdot 2\pi b$$

If the layer which should be investigated is very thin compared to the dimensions of the sample and it is resting on an insulating support, the equation for the resistance becomes [69]:

$$\varrho = \frac{U}{I} \cdot \frac{d\pi}{\ln(2)}$$

d thickness of the layer

This leads to the following relation for the sheet resistance R_{\square} , if the layer thickness is small compared to the distance between the probes and the dimensions of the sample [26, 69, 70, 71]:

$$\begin{aligned} R_{\square} &= \frac{\varrho}{d} \\ &= \frac{U}{I} \cdot \frac{\pi}{\ln(2)} \\ R_{\square} &= 4.532 \frac{U}{I} \end{aligned}$$

R_{\square} sheet resistance

U measured voltage

I measured current

From this definition of the sheet resistance R_{\square} it becomes obvious that the sheet resistance R_{\square} is reduced if the layer thickness d is increased. This is only true, if the layer is homogeneous and continuous. For very thin metal layers this is not always fulfilled. The advantage of this method is that the unknown contact resistance between the electrodes and the sample does not have to be taken into account, as it evens itself out due to the arrangement of the electrodes.

For the measurements described in this thesis two arrangements of the four-point method were used. The basic setup was as the just described (see figure 4.11). The difference is, one was adapted to perform resistance measurements in-situ in the vacuum chamber directly after deposition. The other was used for ex-situ measurements of the whole layer stack after deposition. For the in-situ measurements the head with the electrodes of the four-point method was mounted on a vacuum manipulator in order to be able to press the electrodes in vacuum on the sample directly after the deposition while it was still in the vacuum chamber. The electrical contacts are feed through to the outside of the vacuum chamber and were connected with the measuring device. The four-point arrangement used for the in-situ measurements was the SDKR-13 of NAGY Messsysteme GmbH with a distance of 1.3 mm between the electrodes. For the ex-situ measurements the four-point electrode SP4-62180TRS from Signatone with a electrode distance of 1.59 mm in combination with the measuring system SD-510 from the NAGY Messsysteme GmbH was used.

4.5 Scanning Electron Microscopy

Scanning electron microscopy (SEM) is used to image the topography of the surface of the deposited layers and to check the thickness of the different layers. The principle of a scanning electron microscope is schematically shown in figure 4.12 and is the following [72]: electrons are emitted from a tungsten filament cathode of an electron gun and are accelerated and focused on the sample by magnetic lenses. These electrons are called primary electrons. The interaction of the primary electron beam with the sample results in the reflection of high-energy electrons by elastic scattering (Backscattered Electrons BSE), emission of secondary electrons (SE) by inelastic scattering and the emission of electromagnetic radiation. Measuring the intensity of those signals different properties of the sample can be obtained. By deflecting the beam of the primary electrons horizontally and vertically a rectangular area of the sample surface can be scanned.

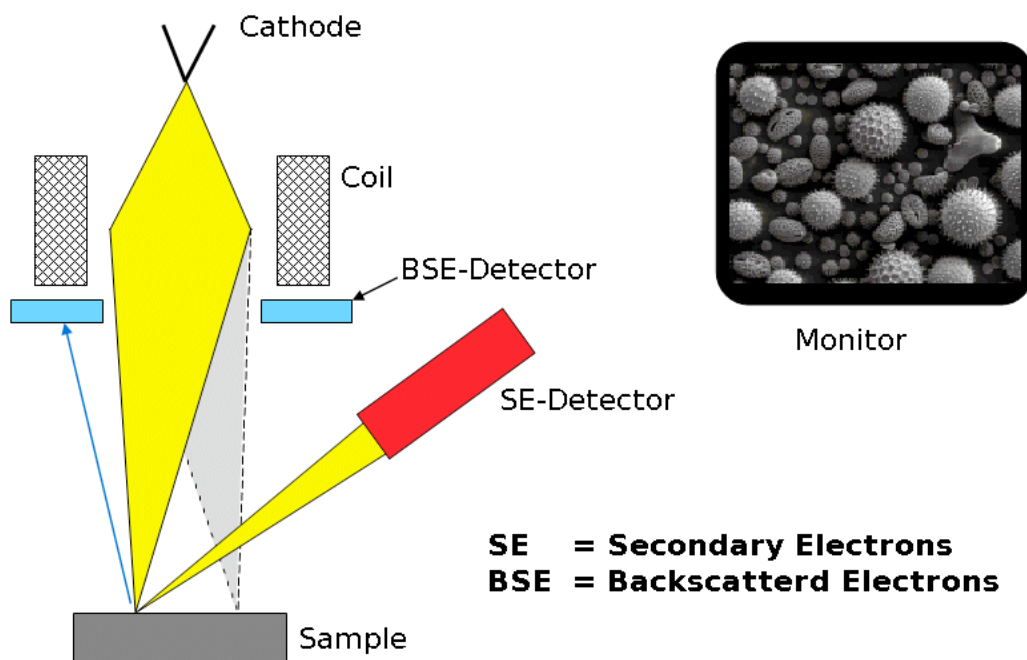


Figure 4.12: Schematic drawing of scanning electron microscope showing the positions of the different detectors for measuring backscattered electrons (BSE) and secondary electrons (SE) [72].

Secondary electrons have a low energy (a few eV) and are coming from the surface of the sample. Like this a high-resolution image of the topography of the sample can be gained. Backscattered electrons have an energy of several keV and provide information about the distribution of the different elements in the surface layer of the sample. The intensity of the signal depends on the atomic number of the material. Heavy elements appear as bright areas as they are well scattering whereas dark areas correspond to light elements.

With this method the surface of the deposited films and the growth mode of different materials depending on the under laying layers were investigated. Measurements to investigate the interfaces between the layers or to determine the thickness were done by high resolution cross-section measurements. For these measurements the samples were halved and the breaking edge was investigated. The measurements presented in this thesis were done with a Hitachi S-4800 SEM at the Zentrum für Mikroskopie of the University of Basel.

Chapter 5

Results

In this chapter the experimental investigations performed in order to optimise the different layer interfaces are discussed. Also the results achieved for transmittance and reflectance as well as the energetic properties of the developed multilayer stacks are presented and discussed.

5.1 The Different Interfaces

For the development and realisation of multilayer stacks with precise optical characteristics it is important to have well defined interfaces between the different thin film layers of the stack. This is due to the fact, that interference is not guaranteed, if the interfaces between the different layers are not clearly defined. A basic prerequisite for interference effects of light are abrupt and ideally flat interfaces. Furthermore it is important, that the different materials are not intermixing or reacting at the interfaces, as well defined changes in the optical constants and the correct ratio between them is necessary in order to get the desired and calculated optical behaviour [73]. Since the multilayer stacks developed for the coating should have a low τ_e/τ_v ratio, based partly on interference effects, it was necessary to check the interfaces between the layers. In several cases an optimisation of the interface was needed.

An effective tool for checking the chemical state of the different materials at an interface is X-ray photoelectron spectroscopy (XPS) and ultraviolet photoelectron spectroscopy (UPS). If the growth of metallic layers are investigated in-situ specific resistivity measurements give evidence concerning the thickness necessary to get a continuous film. Measuring the specific resistivity as a function of the amount of material deposited shows the development of the growing film.

The crucial layers in the development and the deposition of a multilayer coating for sun protection glasses are the thin silver layers, since silver forms islands when deposited on a dielectric, and is easily oxidised. For this reason the silver in combination with dielectric layers are investigated in detail in the following two sections.

5.1.1 Silver on a Dielectric Layer

The growth of thin silver films on dielectric layers is a subject of great interest, as many optical filters, low emissivity coatings, and sun protection coatings are made of thin metallic and dielectric films [37, 74, 75]. Considerable effort has been made by many scientific groups to understand and to improve the film adhesion and the optical and mechanical properties of thin metallic films. Various techniques have been suggested to influence the growth, including direct ion impact [76], simultaneous ion implantation [77], island fragmentation [78, 79], adatom sputtering [80], and removing surface contaminations [81]. In this thesis the influence of ion induced point defects as nucleation sites for silver has been investigated [82].

For the investigation of the influence of ion induced point defects, silicon substrates were thermally oxidised to have a thick layer of silicon oxide at the surface of the samples. The thickness of the thermal oxide layer was determined to be 4 nm by spectroscopic ellipsometry. The choice of the substrates is based on different facts. One reason is, that the thermally grown silicon oxide has a very low roughness and therefore an influence on the growth of silver can be excluded. The second one is, that the design of the enhanced metal-dielectric bandpass requires the deposition of silver on the spacer which is made of silicon dioxide.

After cleaning the substrates with the standard process described in chapter 4.1, they were mounted on a sample holder in the deposition chamber of ESCA III having a background pressure of $2 \cdot 10^{-8}$ mbar. To produce the ion induced point defects the sample holder was used as a cathode which was driven by a rf power of 30 W at a frequency of 13.56 MHz in an argon atmosphere of $2 \cdot 10^{-2}$ mbar. During the plasma treatment the self-bias voltage of the sample was around $U_{Bias} \approx 200$ V.

The treatment was performed for different time intervals. After this treatment of the silicon samples silver was deposited stepwise on the sample by dc magnetron sputtering from a pure silver target with argon as processing gas. The total pressure during the silver deposition was $5 \cdot 10^{-3}$ mbar. The deposition rate of the silver was controlled by a quartz crystal monitor and was kept constant. After the deposition the sheet resistivity was measured with the in-situ four-point method described in chapter 4.4. Further the

evolution of the valance band spectra was determined by UPS measurements in the PES chamber of ESCA III.

In order to find the sufficient duration of the argon plasma treatment of the silicon dioxide surface, the island number density of a 3 ML (mono layer) silver coverage was investigated.

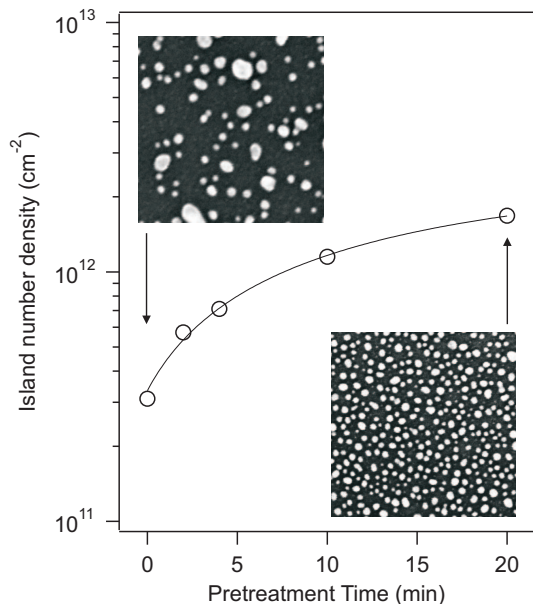


Figure 5.1: Silver island density as a function of duration of the plasma treatment when 3 ML of silver were deposited. The insets show SEM images of Ag deposition on a untreated (top left) and a substrate treated for 20 min (bottom right). The image size is $300 \times 300 \text{ nm}^2$. [82]

and a plasma treated (b) substrate. The spectra at the bottom of the figure represent the silicon substrate with the silicon dioxide surface. The broad peak around 8 eV is related to excitations of the oxygen 2p band. The deposition of silver leads to the formation of a new band at approximately 6 eV. This belongs to the 4d-band of silver which gets more pronounced with the amount of silver deposited. At the same time the contribution of the oxygen 2p band decreases, as the silver layer becomes dense. Another feature, which indicates that a silver layer is forming, is the appearance of a Fermi edge at 0 eV. The Fermi edge becomes more pronounced with increasing amounts of silver. After the deposition of 14 nm silver the spectra are identical to a measured spectrum of bulk silver which was measured but is not shown here. Comparing the development of the spectra for the virgin and the plasma treated substrate show, that the building up of the silver 4d-band is more pronounced for the case of the

investigated. The evolution of the island number density, given in figure 5.1, shows that it increases with pre treatment time, but the longer the treatment, the smaller the relative change of the island number density becomes. The insets in figure 5.1 are SEM images showing the Ag island density for a virgin substrate and a substrate, which was treated with an argon plasma for 20 min. Comparing the two SEM images shows, that the mean island size of silver has decreased due to the plasma treatment, while the island density has increased. This indicates a more homogeneous film nucleation, which is probably based on an increased concentration of nucleation sites induced by the low energy bombardment with argon ions.

Figure 5.2 shows the development of the valance band spectra measured by UPS using the HeI-line, when the amount of silver deposited is slowly increased on a virgin (a)

plasma treatment. This implies, that after the plasma treatment the coverage of the silver film, for the same amount of deposited silver, is higher which signifies an earlier coalescence.

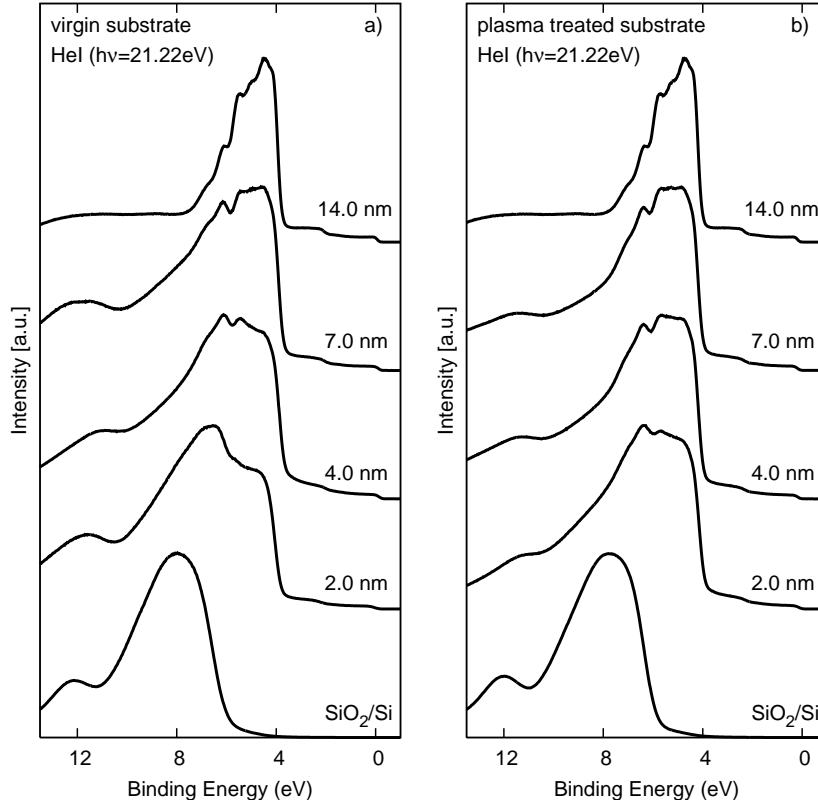


Figure 5.2: Evolution of the valence band spectra (HeI) as a function of the amount of silver deposited on a virgin (a) and a plasma treated (b) substrate. [82]

The shape of the valence band spectra further shows, that on both substrates the deposited silver is not oxidised. If the silver would be oxidised, the HeI spectrum would show two additional peaks at about 2 eV and 3 eV, which are not present in the measured spectra [83, 84].

The changes to the silicon dioxide surface induced by the plasma treatment were investigated by angle-resolved XPS measurements. The results are presented in figure 5.3, where high resolution core level spectra of the Si $2p$ region are shown. The topmost spectrum in both graphs correspond to normal emission. For the virgin substrate (a) three components can be identified: the $2p_{3/2}$ doublet (Si^0) of pure silicon at a binding energy of 99.0 eV with a spin-orbit splitting of 0.6 eV and two lines located at 100.5 eV and 103.3 eV corresponding to silicon in Si^{+1} and Si^{+4} oxidation states, respectively. The Si^{+4} state belongs to the SiO_2 layer, whereas the Si^{+1} corresponds to a suboxide.

When the detection angle is increased the intensity of the doublet at 99.0 eV corresponding to the pure silicon substrate and the peak at 100.5 eV belonging to the

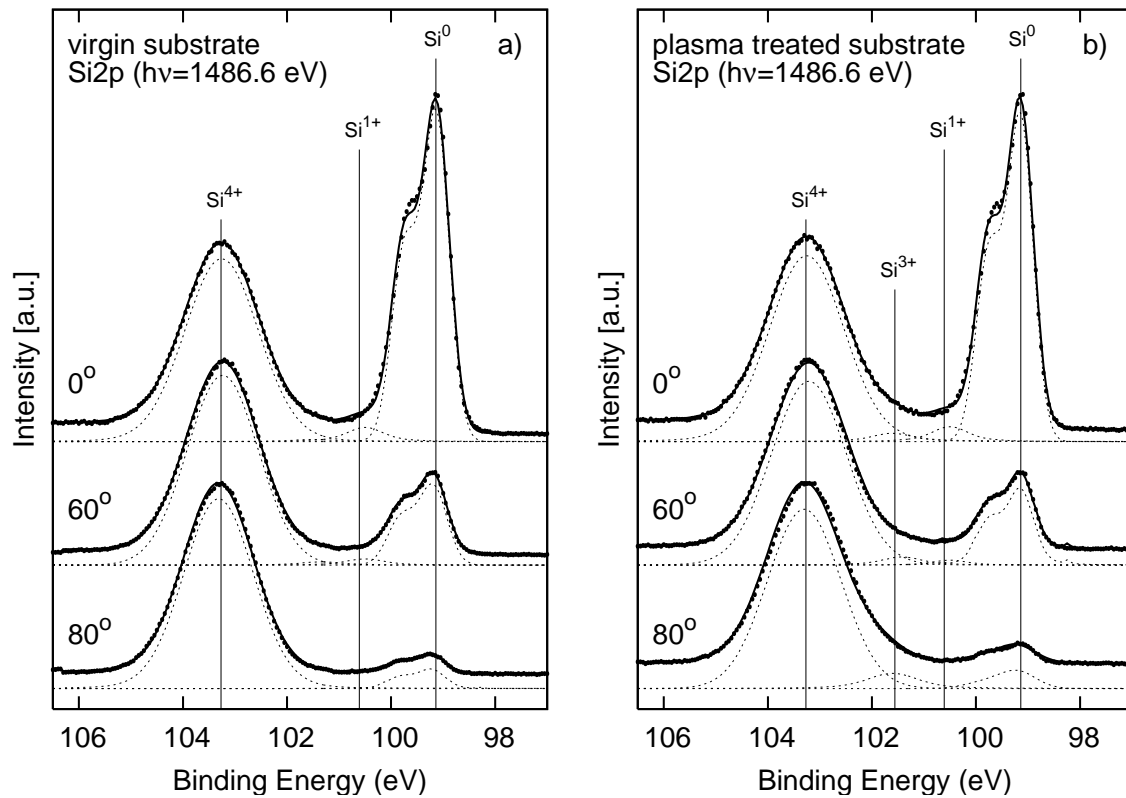


Figure 5.3: The Si 2p core level measured angle-resolved by XPS on (a) a virgin silicon substrate with 4 nm thermal oxide and (b) after a 20 min argon plasma treatment. Dashed lines represent the chemically shifted components after core line decomposition. [82]

suboxide Si⁺¹ decrease. This is expected, since an increase of the detection angle results in a decrease of the penetration depth and therefore the information depth also decreases. The measured intensities therefore correspond to the chemical composition of the surface. The decrease of the Si⁺¹ component indicates that this suboxide exists at the interface between the silicon substrate and the silicon dioxide surface layer. In the case of the plasma treated surface (b) another peak in the spectra is visible. This peak is located at 101.6 eV and corresponds to the Si⁺³ oxidation state another suboxide. An increasing contribution of this peak with increasing detection angle indicates that the Si⁺³ oxidation state is only on the surface of the silicon dioxide. An explanation for this phenomenon is, that the defects created by the ion impact are neutral (F_S) or charged (F_S^+) vacancies created by removing neutral oxygen atoms. Venables et al. [85] state that silver atoms are strongly bound to vacancies, which leads to an enhanced nucleation of the films. This is in good agreement with the observations made by UPS.

Another method to investigate the influence of the plasma treatment of the substrate on the growth of silver is to measure the sheet resistance. The sheet resistance for the increasing silver deposit on the samples further supports the observations of earlier

nucleation. In both cases the specific resistivity depends strongly on the amount of silver deposited, see figure 5.4. The percolation threshold is found to be at ~ 4.8 nm and ~ 3.5 nm for the virgin and the plasma treated silicon dioxide, respectively. Below the percolation threshold no resistance can be measured as the deposited silver forms separated and therefore isolated islands on the substrate. With the increasing amount of silver deposited the islands grow in size, coalescence of islands occurs, and continuous conducting paths are formed. Between 5 nm and 10 nm the resistivity decreases rapidly with increasing layer thickness for both substrates. It may be assumed, that for this range of thickness the deposited silver does not yet form a continuous film, but an interlinking network of islands. This is supported by the results obtained by UPS (see figure 5.2), as the information depth of HeI irradiation is about 0.5 nm and the spectra for 7 nm still shows contributions from the oxide substrate. Further deposition of silver leads to a monotonous decrease of the resistivity approaching the bulk value of $1.6 \mu\Omega\text{cm}$ for silver. For the whole thickness range examined the resistivity values of the plasma treated substrate are lower than those of the virgin substrate. This indicates, that silver on the plasma treated substrate shows a growth behaviour which leads earlier to metallic layers.

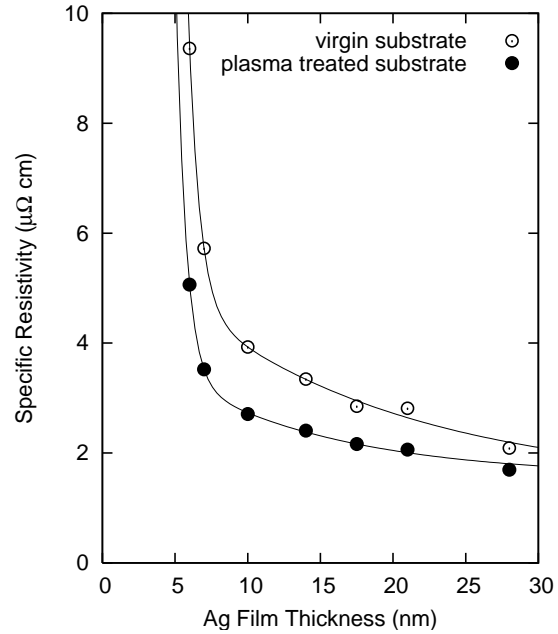


Figure 5.4: Specific resistivity as a function of the silver deposited on a virgin or a plasma treated substrate. The given lines are guides for the eye [82].

It should further be noted, that at a thickness of 14 nm the UPS spectra are identical to the one measured on a bulk sample, but the resistivity has not reached the bulk value ($1.6 \mu\Omega\text{cm}$) even at 30 nm. The resistivity values for the virgin and the plasma treated substrates are $3.3 \mu\Omega\text{cm}$ and $2.4 \mu\Omega\text{cm}$, respectively, for 30 nm of silver. The difference can be explained by the fact that electron scattering is much higher in thin films when the geometrical dimensions become comparable to the electron mean free path [26]. Additional, scattering of electrons on grain boundaries may significantly contribute to the resistivity of the silver layers.

Further the surface roughness, defined as the arithmetic average of the absolute values of the surface height deviation, was investigated by atomic force microscopy (AFM). If

the same amount of material was deposited a higher surface roughness implies that the electron mean free path has decreased as scattering is enhanced in narrow conduction paths between the different grains. The surface roughness for 14 nm thick silver films measured by AFM was about 2.1 nm if deposited on the virgin oxide films and 1.9 nm for the films deposited after the plasma treatment.

This study shows, that by pre-treating the silicon dioxide surface the growth and therefore the optical and mechanical properties of silver layers can be improved. Another possibility to improve the silver growth is to introduce a very thin sticking layer like zinc oxide, which itself has no influence on the optical characteristics of the hole multilayer, but on the growth mechanism and therefore on the optical properties of the silver layer [45]. One can add small amounts of a different material, e.g. antimony, indium, or platinum, in order to act as surfactant for the growth of silver films [86]. These can be added to the deposition by mixing the surfactant material into the silver target, by using a segmented target, or by focussing two magnetrons on the sample. Further investigation is needed to determine, which of these possibilities will ultimately be best suited.

5.1.2 Metal Oxides on Silver Layers

In multilayer coatings used for optical filters, heat mirrors, or sun protection glasses the metal layers, often silver, are covered most of the time with an oxide layer. In the case of the bandpass filters, described in chapter 2.4, silver is covered either by titanium dioxide or by zinc oxide. The metal oxide films have to be deposited by reactive sputtering from metal or suboxide targets in an atmosphere containing oxygen in order to get stoichiometric films with ideal optical properties [87]. During the initial phase of deposition, until a continuous layer of the metal oxide is formed, the underlying silver layer will be exposed to the gas mixture containing oxygen. Silver is a metal which may easily be oxidised, especially if the thin films are freshly sputtered [31, 46, 88, 89, 90]. The optical constants of silver oxide generally differ from those of the silver, i.e. the values for n are higher whereas the values for k are lower for silver oxide compared to pure silver [53, 91, 92]. This means silver is losing its ability to reflect infrared radiation due to oxidation and thus it is of lesser use for sun protection coatings on glass panes [88].

The phenomenon that silver is oxidised during the deposition of the metal oxide covering layer by reactive sputtering is well discussed in literature. Martin-Palma et al. investigated the influence of nickel chromium (NiCr) as a protection layer for silver, when silver is sandwiched between two tin dioxide (SnO_2) layers [88]. They found,

that the transmittance in the visible range (300 nm – 800 nm) is about (10% – 20%) lower, when the NiCr protection film is omitted. Furthermore, they found the infrared reflectance is very low and nearly equal to that of the uncoated glass. As an alternative to nickel chromium as a protection film, silicon nitride (Si_3N_4) could be used, which has the further advantage of being more durable [93]. Another possibility to prevent the oxidation of silver is to use silver alloys showing similar properties as a pure silver layer, after being partly oxidised [31]. A third possibility is to add the same amount of hydrogen as oxygen to the gas mixture used for the reactive sputtering of the metal oxide layers [89]. The problem with these methods is, they either need an extra material or they need hydrogen, that forms an explosive mixture with oxygen.

For the multilayer coatings described in this thesis the aim was to find a solution for the protection of the silver layers, that has little to no influence on the optical properties of the whole multilayer coating. The idea was to use a thin titanium layer to protect the silver. The thickness was chosen in such a way, that the titanium layer would be completely oxidised during the following deposition of the titanium dioxide and therefore should have no influence on the optical behaviour of the coating. This is the case, when the sum of the thicknesses of titanium and titanium dioxide is equal to the thickness determined by the simulations for the pure titanium dioxide layer.

For the verification of this method, silver was deposited on cleaned silicon samples by magnetron sputtering at a total pressure of $6.3 \cdot 10^{-3}$ mbar in a pure argon atmosphere. After the deposition the chemical composition of the layer was investigated by XPS measurements. The bottom curves in both graphs of figure 5.5 show the $3d$ core-level of the deposited silver layers having a thickness of 15 nm and 23 nm, respectively. The position of the $3d_{5/2}$ peak of the doublet is at a binding energy of 368.2 eV, which is identical to the silver peak measured on a clean bulk silver sample and to the values given in literature. As only one doublet is needed for the representation of the core line, it may be concluded that the silver layer is not oxidised.

In order to investigate the influence of a thin titanium buffer layer, titanium dioxide was deposited on the silver layers by reactive sputtering either directly, or after the deposition of a 2 nm titanium layer. Titanium dioxide was sputtered from a pure titanium target in a gas mixture containing argon and oxygen at a total pressure of $6.2 \cdot 10^{-3}$ mbar. The partial pressures of argon and oxygen were $p_{\text{Ar}} = 6.0 \cdot 10^{-3}$ mbar and $p_{\text{O}_2} = 1.1 \cdot 10^{-3}$ mbar, respectively. For the deposition a magnetron driven by pulsed dc was used, with a power of 50 W and a pulse frequency of 100 kHz. The 2 nm titanium layer was deposited in a pure argon atmosphere having a total pressure of $p_{\text{total}} = 6.0 \cdot 10^{-3}$ mbar. The settings of the pulsed dc-power supply were identical to the ones used for titanium dioxide ($P = 50$ W, $f_p = 100$ kHz).

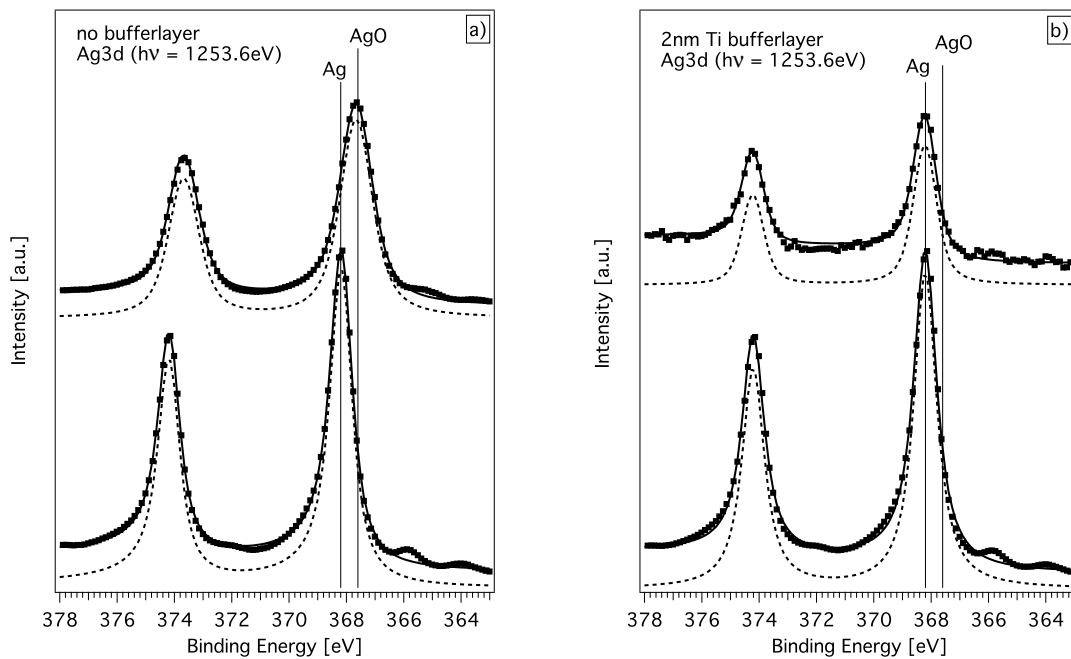


Figure 5.5: Silver 3*d* core level measured by XPS. The bottom spectra in both graphs belong to the freshly sputtered silver layers. The upper spectra were measured after the deposition of titanium dioxide on the silver layer either (a) directly, or (b) after first depositing a 2 nm titanium layer. The dots represent the measured values, the dashed lines the doublet obtained through fitting and the continuous line the sum of the fitted doublet and the background signal.

The upper curve in figure 5.5 (a) shows, that the chemical state of the silver layer is changed after the direct deposition of titanium dioxide onto the silver layer. The doublet is shifted to smaller binding energies. The position of the silver 3*d*_{5/2} peak after the deposition of the titanium dioxide is shifted by 0.6 eV to the position of silver oxide at 367.6 eV. From this measurement it is not possible to determine, if the whole silver layer is oxidised or if it is only oxidised at the surface of the interface. The reason is, that the information depth of the XPS signal is only a few Ångström and the thickness of the titanium dioxide layer is around 5 nm. Hence only a few Nanometer of the underlying silver can be investigated. But it can be concluded that the surface is fully oxidised, as only one doublet was needed for the representation of the measured spectrum.

To avoid the oxidation of the silver layer a buffer layer of pure titanium was introduced. The silver layer (lower curve) in figure 5.5 (b) was deposited at the same conditions as in the first case described and measured by XPS. After this a 2 nm thick layer of titanium was deposited in a pure argon atmosphere. Without interrupting the plasma the titanium dioxide layer was deposited by adding oxygen to the sputtering atmosphere in the deposition chamber. The oxygen was added by opening the gas inlet while the deposition was running. The upper curve in figure 5.5 (b) shows the measured Ag 3*d*

spectrum after the deposition of a 5 nm thick TiO_2 layer on top of a 2 nm titanium buffer layer. The measurements shows that the silver layer is not oxidised after the deposition of the titanium and the titanium dioxide layer, as the position and the line splitting of the doublet has not changed. Further the fitting of the spectrum leads only to one component, indicating that the layer is not even partly oxidised. The signal of the silver layer is very weak, as the thickness of the total covering layer is of the same order as the information depth of the XPS measurement.

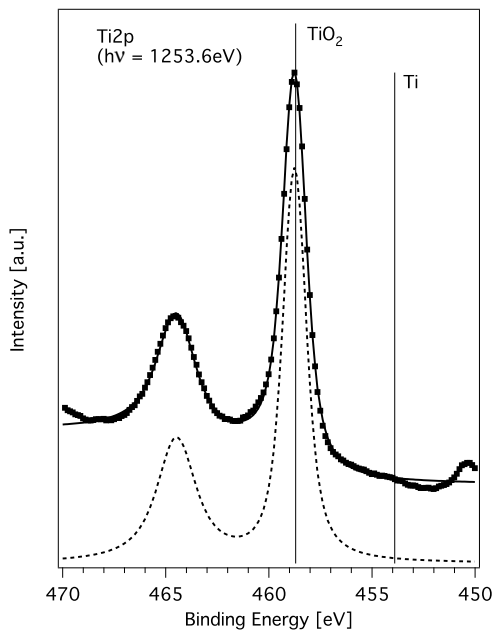


Figure 5.6: Titanium $2p$ core level measured by XPS after depositing 2 nm of pure titanium and then adding a 5 nm thick titanium dioxide layer by reactive sputtering in an atmosphere containing argon and oxygen. The dots represent the measured values, the dashed lines the doublet obtained through fitting and the continuous line the sum of the fitted doublet and the background signal.

oxide is an insulator. With this method it is relative simple to monitor the chemical state of the silver and to recognise when changes appear. Reasons for changes could be a variations of the deposition rate or the gas concentrations. The disadvantage of measuring the sheet resistance is, that it is not possible to check if the buffer layer is completely or only partly oxidised, in order to have no influence on the optical properties of the complete layer. The advantage is, that it can easily be performed on samples deposited on glass and it is possible to control during or after the deposition with the in-situ or the ex-situ four-point method, respectively.

Besides the fact that it was possible to prevent the oxidation of the silver layer it is of interest to know the chemical state of the titanium buffer layer. In figure 5.6 the measured $2p$ core level of titanium and the composition of the spectrum are given. The $2p_{3/2}$ peak is at a binding energy of 458.7 eV corresponding to the position of titanium dioxide. Further there is no contribution at 453.9 eV, the peak position belonging to pure titanium. This indicates, that the titanium buffer layer was completely oxidised during the following reactive titanium dioxide deposition.

Another way to check if a buffer layer is sufficient for the protection of the silver layers is, to measure the sheet resistance of a coating. In figure 5.7 the sheet resistance of a multilayer coating with different thicknesses of the titanium buffer layer is shown. When the silver is partly or completely oxidised, the resistance becomes very high, as silver

Another experimental method is to compare the transmittance of different coatings, where only the thickness of the buffer layer was varied. If the total transmittance is reduced the buffer layer is too thick and not oxidised. Furthermore, changes in the infrared properties indicate that the silver layer was partly oxidised as the thickness of the buffer layer was too thin to protect the silver from oxidising.

The experiments described in this section have shown, that silver layers can be protected against oxidation during the reactive deposition of the following metal oxide by first depositing a very thin metal layer. This buffer layer is later oxidised during the deposition of the oxide. The advantage of this method is that the buffer layer has no influence on the optical properties, as long as it consists of the same metal as the following metal oxide.

This method to protect silver layers has only been proven for titanium, but it is expected to work with other metallic oxides, if they are deposited by reactive sputtering. Only the thickness of the buffer layer is expected to vary for different metals.

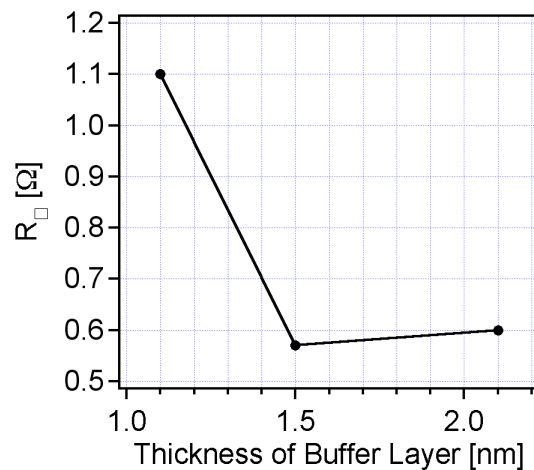


Figure 5.7: The sheet resistivity is very sensitive concerning the oxidation of the silver layer which strongly depends on the thickness of the buffering titanium layer. The titanium layer prevents the oxidation of the underlying silver layer.

5.2 Multilayer Coatings

In the first part of this chapter investigations concerning the interface between two layers were described. The following part will deal with the experimental realisation of the multilayer coatings developed theoretically in chapter 2 and optimised by simulations in chapter 3. The coatings described here were deposited in the in-line plant (see figure 4.3) on float glass of 4 mm thickness. For the deposition titanium oxide (TiO_x), zinc (Zn), silver (Ag) and SiSPA-targets were used, which were reactively sputtered to obtain oxides when needed. SiSPA is a mixture of silicon (Si) and aluminium (Al), at a ratio of around 80 – 95% Si and 5 – 20% Al [94, 95]. It was used as it has nearly the same optical properties as silicon dioxide if reactively sputtered, and the deposition itself is causing less problems, like charging and arcing. In the following it is referred

to as silicon dioxide. The combination of the targets used for the deposition varied with the design of the multilayer stacks. The coated glass was then investigated by the methods described in chapter 4 to fully characterise the optical and energetic properties of the deposited coating and to determine the colour appearance of the coated glass in transmission as well as reflection.

5.2.1 Design with TiO_2 , Ag and SiO_2

The first design realised was the enhanced metal-dielectric bandpass, described in chapter 2.4.2 in detail. The speciality of this bandpass filter is, that it combines the advantages of a metal-dielectric filter with those of an all-dielectric filter. Figure 5.8 shows a schematic drawing of the multilayer stack, which is giving the order but not the thicknesses of the layers used for the deposition. Compared to the stack given in the theoretical part of this thesis (see figure 2.7), which was used for the basic simulations, some additional layers were added.

The first change added to the multilayer stack is based on the experimental results concerning the layers surrounding silver, which were obtained in the experiments described in chapter 5.1. The modification was to introduce thin titanium layers on top of each silver layer to protect silver against oxidation during the reactive sputtering process of the following titanium dioxide layer. Details concerning the interface silver/titanium dioxide with the included titanium buffer layer are given in chapter 5.1.2. It is not necessary to take these layers into account during the simulations, as the titanium is completely oxidised during the deposition of the titanium dioxide. Due to this fact the layer thicknesses of the titanium oxide layers are reduced by the thickness of the titanium layer, when the deposition plan is composed.

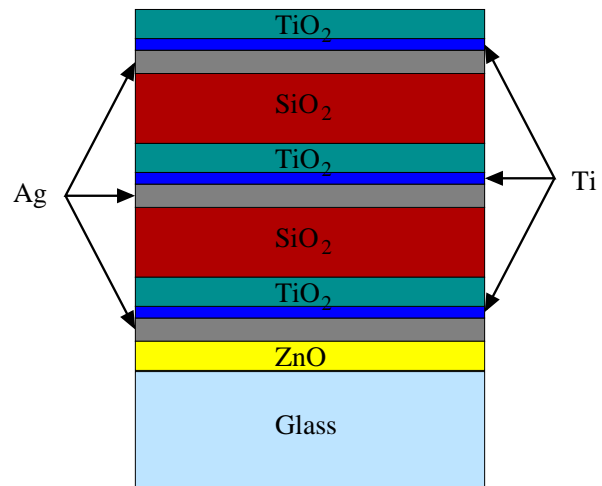


Figure 5.8: The enhanced bandpass filter, where a zinc oxide layer between the glass and the first silver was introduced. Further the titanium dioxide layer was split up into a titanium and a titanium dioxide layer. The titanium layers are oxidised during the following deposition of the titanium dioxide layers.

The second change compared to the layer stack given in figure 2.7 is the thin zinc oxide layer between the first silver layer and the float glass. This layer is needed as the mechanical stability of coatings is very low, if silver is directly deposited on glass. The

reason for this is, the sticking coefficient of silver on glass is not very high [45, 96, 97]. To overcome this problem a thin zinc oxide (ZnO) layer of 5.5 nm was introduced in the design of the enhanced bandpass filter. The influence of this zinc oxide layer on the optical properties of the multilayer coating can be neglected as it is very thin and transparent in the visible range.

Even after these changes the basic concept of the enhanced metal-dielectric bandpass filter is unchanged. The mirrors for the double cavity Fabry-Perot filter are formed by the silver and titanium dioxide layers, having a high ratio between their refractive indices. On the other hand using a mirror containing a metal layer leads to a high infrared reflectance. The spacer needed to separate the mirrors is made of silicon dioxide which has a refractive index between the indices of the other two materials.

In the table below the thicknesses of the different layers in nm, obtained from the simulations, are given. As a first approach these were deposited on a 4 mm float glass:

Glass	ZnO	Ag	Ti	TiO ₂	SiO ₂	Ag	Ti	TiO ₂	SiO ₂	Ag	Ti	TiO ₂
	5.5	17.8	2.1	46.6	11.4	16.2	2.1	50.0	9.2	24.6	2.1	30.1

The measured spectral transmittance for this coating is given in figure 5.9 by the red curve. Comparing the measured transmittance with the theoretical spectral transmittance $\tau_{min}(\lambda)$ (black, dotted curve) shows clearly, that the coating is not yet reaching the theoretical curve. On the one hand the measured transmittance is shifted to larger wavelengths and on the other hand it is too broad compared to the theoretical curve. The light transmittance for perpendicular incidence was measured to be $\tau_v = 0.549$ and the solar direct transmittance to $\tau_e = 0.217$, which leads to an energy load coefficient of $\tau_e/\tau_v = 0.398$. Therefore the theoretical goal of 0.334 is not reached yet. The energy load coefficient τ_e/τ_v turns out to be of this magnitude, because the coating is not sufficiently reflecting the near infrared radiation between 700 nm and 800 nm.

The obtained colour values for perpendicular incidence of the transmitted light are $a = -1.9$ and $b = -2.2$ in the Lab CIE colour system, which are in the range of the tolerated values defined earlier in chapter 3, where $|a|$ and $|b|$ should be less than five. The reflected light has a blue-greenish colour given by the values $a = -17.0$ and $b = 1.5$ in the Lab CIE colour system.

The specific resistivity of this multilayer coating has been measured by the ex-situ four-point method. It turned out to be $\rho = 4.80 \Omega\text{cm}$. As the total thickness of the silver layers of this multilayer stack is $d_{total} = 58.6 \text{ nm}$ the measured specific resistivity is based on experience too high. This leads to the conclusion, that the silver is either not growing in dense layers, but as interlinking islands or it is partly oxidised during

the deposition of the titanium dioxide layers. In the first case the optical constants should differ to those used in the simulations, due to the fact that interlinking island reveal more scattering effects [45]. In the second case the thickness of the silver layer is unequal to the simulated one. As silver was deposited directly on the silicon dioxide layers, it is suspected that the case of interlinking islands is more realistic, especially as titanium buffer layers have already been introduced. To overcome this problem thin layers ($d = 5.5$ nm) of zinc oxide (ZnO) are introduced underneath each silver layer, as silver forms flat and dense layers on zinc oxide [98]. An alternative solution would have been to use the plasma treatment described in chapter 5.1.1, but this was not implemented in the in-line deposition plant. After the introduction of the zinc oxide layers the specific resistivity of the multilayer was reduced to $\rho = 4.68$ Ωcm , but the theoretical transmittance τ_{min} was still not reached.

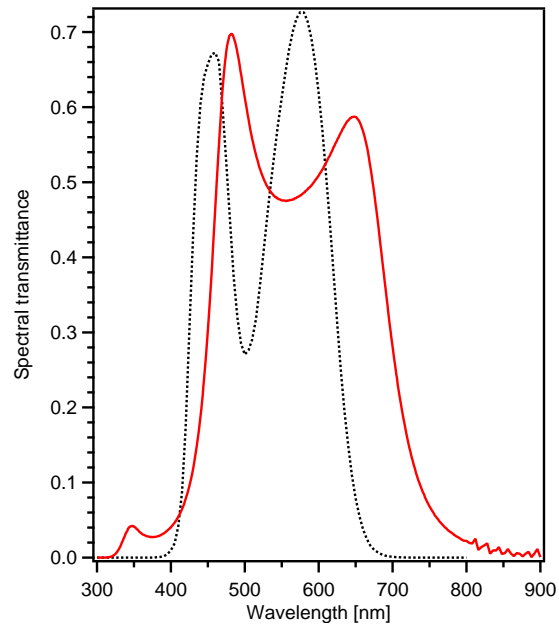


Figure 5.9: The red line shows the spectral transmittance of the multilayer coating made of TiO_2 , SiO_2 and Ag with a thin ZnO layer between the glass and the first silver layer to increase the sticking coefficient. The black dashed curve is the theoretical spectral transmittance introduced in chapter 2.1.

Since not only the optical properties of silver depend on the underlying layers further simulations were needed. After several iteration steps of the thicknesses of different layers the measured spectral transmittance shown in figure 5.10 by the red curve was obtained. Comparing the measured spectral transmittance with the theoretical transmittance $\tau_{min}(\lambda)$, represented by the black dotted curve (Figure 5.10), shows, that the shape of the two curves is quite similar. The measured transmittance is still broader than the theoretical aim and therefore contributes unwanted spectral energy in the red part of the spectrum ($\lambda = 680$ nm – 800 nm). Although this coating seems to have a transmittance that is closer to the given theoretical transmittance than the one described before (figure 5.9), the energy load coefficient was not reduced. The energy load coefficient is still $\tau_e/\tau_v = 0.397$. The reason for this is, that on one hand the solar direct transmittance was reduced by 10% to $\tau_e = 0.200$, which is an improvement, but on the other hand the light transmittance of this coating is $\tau_v = 0.504$ for perpendicular incidence, which means that τ_v is also reduced by a factor of 10%.

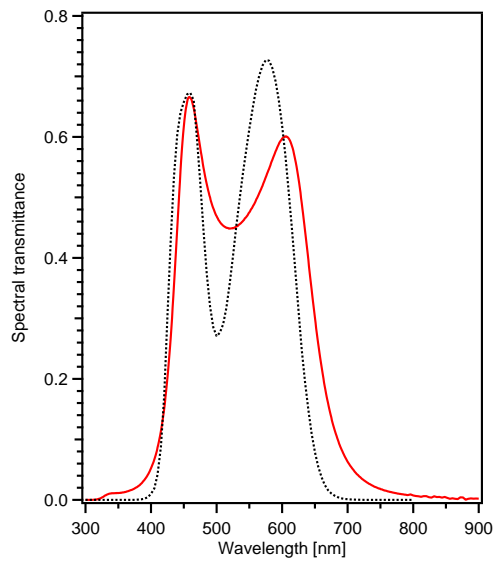


Figure 5.10: The red line shows the spectral transmittance after inserting a thin layer of ZnO under each Ag layer and adapting the layer thicknesses in order that the sample reaches the theoretical spectral transmittance (black, dotted line).

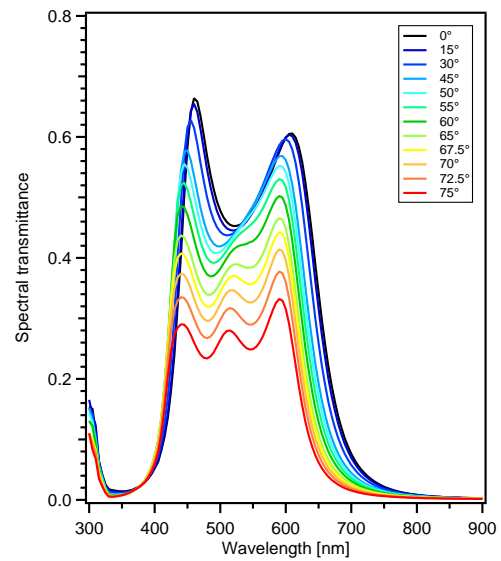


Figure 5.11: The angular dependence of the spectral transmittance of a multilayer design with TiO₂, Ag, SiO₂ and ZnO as a bounding layer. The different colours give the spectral transmittance for the different angles given in the graph. The increase of the transmittance for $\lambda < 350$ nm is an instrumental artefact.

In figure 5.11 the development of the transmittance for different angles of light incidence is shown. It becomes clear, that for small angles, i.e., nearly normal incidence, the shape of the transmittance and therefore the properties of the sun protection glass are hardly changing. Although the shape of the transmittance changes with varying angles the slopes are not losing their steepness. The slope at around 400 nm is not changing at all and the one towards the infrared radiation shifts to smaller wavelengths, which leads to a reduction of the energy load coefficient. The evolution of the energy load coefficient versus the angle of light incidence is given in figure 5.12. The green curve shows that the energy load coefficient is decreasing with increasing angle of light incidence. Further the figure shows the evolution of the light transmittance $\tau_v(\varphi)$ (blue curve) and the solar direct transmittance $\tau_e(\varphi)$ (red curve).

Although the transmittance of the coating is not identical to the theoretical transmittance τ_{min} and therefore the energy load coefficient is still larger than the aim of 0.334, it is still an improvement in comparison to the existing sun protection glasses on the market, nowadays. As already mentioned most of the commercial sun protection glasses consisting of two glass panes have an energy load coefficient that is greater than 0.48 independent of the light transmittance. Having an energy load coefficient $\tau_e(\varphi)/\tau_v(\varphi)$ less than 0.4 for all angles of light incidence, this coating is already an improvement. By adding another glass pane to form a sun protection glass the energy load coefficient

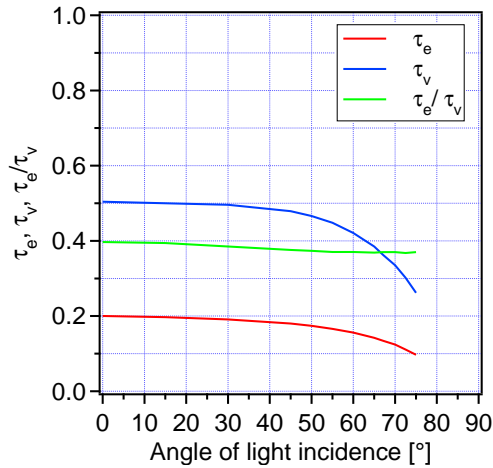


Figure 5.12: The evolution of the light transmittance τ_v (blue), solar direct transmittance τ_e (red) and the energy load coefficient τ_e/τ_v (green) for different angles φ of light incidence.

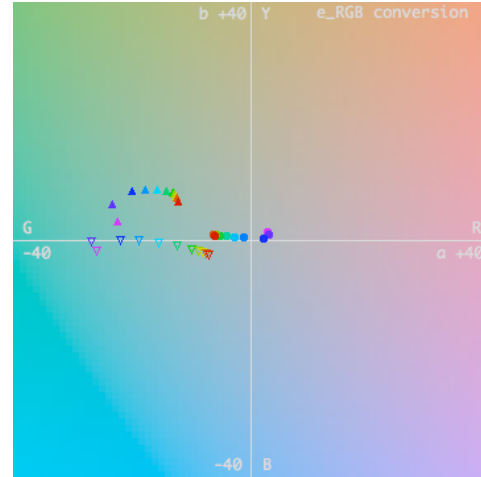


Figure 5.13: Representing the colour evolution in the CIE Lab colour space at constant luminosity of the transmittance (full circle), reflectance glass side (full triangles) and reflectance layer side (empty triangles), if the angle of light incidence is changed. For the smallest angle a purple symbol is used and for the largest a red symbol.

τ_e/τ_v is further reduced. Another positive side effect is that the energy load coefficient even decreases with increasing angle of light incidence. This is of importance as sun light usually enters a building through a window under a varying angle greater than $\varphi = 0^\circ$ except for dormers in the roof. So with a decreasing energy load coefficient the actual performance of a sun protection glass in a building even increases. The other demand of having a light transmittance $\tau_v(0^\circ) > 0.5$ is even fulfilled for angles up to $\varphi = 30^\circ$. Until an angle of $\varphi = 60^\circ$ the light transmittance is greater than 0.4, only for greater angles it decreases rapidly. A reduction of the light transmittance for larger angles has the benefit, that the blinding effect of the sun at large angles is also reduced.

Besides the energetic properties of the coating the colour appearance is very important, as the colour is an important feature in architectural design. The evolution of the colour for the reflected or transmitted light with changing angles of light incidence is shown in figure 5.13 in the CIE Lab colour space. The filled circles represent the values for the transmitted light, while the filled and open triangles correspond to light reflected from the glass side and the layer side of the coated glass, respectively. The colour of the circles or triangles correspond to the angles of light incidences as follows: purple corresponds to $\varphi = 0^\circ$ and red to $\varphi = 75^\circ$ for transmitted light. For the reflected light purple corresponds to $\varphi = 15^\circ$ and red to $\varphi = 75^\circ$. The steps of the angles are the same as the ones depicted in figure 5.11 giving the angular evolution of the measured transmittance.

The colour coordinates for the transmitted light of this coating are between $-6.1 < a < 3.3$ and $0.2 < b < 1.3$. The values of the colour coordinates are for all angles between 0° and 60° in the range of values $|a| < 5$ and $|b| < 5$, that are still sensed as colour neutral by the human eye, which was defined in chapter 3. Since the eye is very sensitive towards yellow components in the transmitted light, it is of importance to keep the values of b as small as possible, which is fulfilled by this coating. The colour of the reflected light for this coating is green, changing from blue green ($a = -22.6$, $b = 3.3$) to yellowish green ($a = -12.4$, $b = 6.6$), going from small to large angles of light incidence. Although the colour is changing through different shades of green the hue of the reflected colour is constant as demanded in chapter 3.

The colour properties of this coating are therefore all satisfying, but the energetic properties would need further improvements. The attempt to further optimise this coating was not made, as the design itself is too complicated for industrial serial production. The reason is, this design contains a total of fourteen different layers made of four different materials. The design needs eight optical layers to form the optical bandpass, which are made of silver, titanium dioxide and silicon dioxide. To improve the growth and the adhesion of the silver layers on glass or on silicon dioxide another three layers made of zinc oxide are required. And finally to prevent the oxidation of the silver layers during the reactive deposition of titanium dioxide, the second material for the mirrors, another three titanium layers are of need. In addition to these fourteen layers further layers would be needed to protect the whole layer stack, against mechanical or chemical influence, like scratching or etching, respectively.

5.2.2 Design with ZnO and Ag

The second design, which was investigated, is based on a classical metal-dielectrical Fabry-Perot interference filter. A detailed description concerning this filter is given in chapter 2.4.1. As already mentioned in connection with the enhanced bandpass design the simulated layer thicknesses have to be adjusted during the process of realisation, even if realistic optical constants for the different layers are used during the simulations. The reason for this is, that the optical constants of each layer strongly depend on the layers surrounding it, this is because the underlying layer influences the growth mode of the deposited layer and the following layer can change the chemical composition of a few atomic monolayers at the interface. This is not only true for metallic films, but also for ceramic metal oxide films. The layer sequence of the metal-dielectric design is shown in figure 5.14, only representing the order of the layers but not the actual thicknesses. As already described with the other design in the previous section additional layers were

added, which have no influence on the optical design itself, but influence the optical properties and the growth of the different layers.

To prevent, the silver layers from getting partly oxidised during the deposition of the following ZnO layer, thin titanium layers were introduced on top of each silver layer. That the introduction of a buffer layer is an excellent method to prevent the oxidation of the silver layers was experimentally investigated and described in detail in chapter 5.1.2. During the following reactive sputtering deposition of the zinc oxide layers those thin titanium layers are oxidised to titanium dioxide and are transparent in the wavelength region of interest. To assure that only the titanium is fully oxidised, a thickness of 2.1 nm for those buffer layers was used. This thickness was determined experimentally, by depositing multilayers with different thicknesses of the titanium layers. After the deposition the transmittance and the specific resistivity were measured. The thickness corresponding to the minimum of the specific resistance was chosen for the titanium layer (see chapter 5.1.2).

Further a zinc oxide layer between the first silver film and the glass substrate was introduced to increase the stability of the multilayer coating, as silver has a very low sticking coefficient, if deposited directly on glass [45, 96, 97]. The thickness of this layer was 5.5 nm, in order to avoid an influence of this layer on the optical characteristics of the multilayer coating.

As a final change to the theoretically developed bandpass coating given in figure 2.6 an additional covering layer made of silicon nitride (Si_3N_4) was introduced. This layer was added to enhance the stability of the coating, since zinc oxide is a very soft material, especially if deposited by reactive sputtering [99, 100]. The hardness of zinc oxide is between 2.0 GPa – 7.1 GPa depending on the production mechanism [99, 101, 102]. Due

to this very low hardness it is even used as lubricant [100]. To protect the multilayer coating a silicon nitride layer was added to the design. Silicon nitride was chosen, as its thin films have excellent properties such as high chemical inertness, high ther-

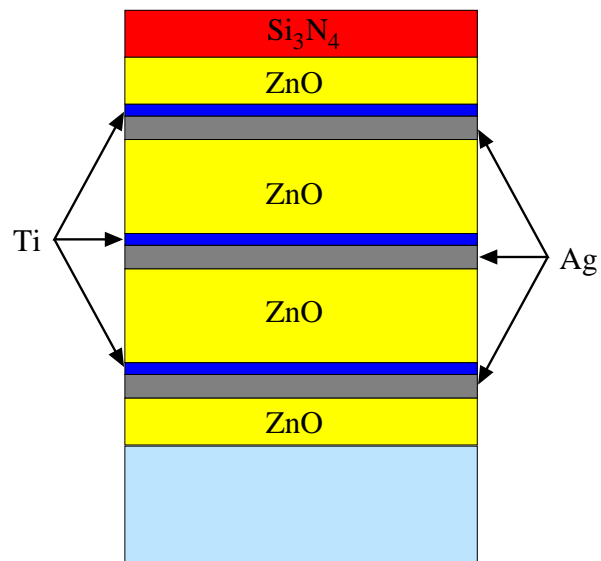


Figure 5.14: Schematic drawing of the layer stack used for the coatings with zinc oxide and silver. The thin titanium layers were introduced to prevent the oxidation of the silver layers during the deposition of the following ZnO layer, as investigated in chapter 5.1.2. The titanium layers are oxidised during the following deposition of the zinc oxide layers.

mal stability, good corrosion resistance and excellent mechanical, optical and dielectric properties [103]. The properties relevant for the multilayer coatings described in this chapter, will be discussed in detail. The hardness of silicon nitride thin films is between 14.1 GPa–20.5 GPa, which is about three times higher than the hardness of zinc oxide. Further its influence on the optical properties of the multilayer design is very small, as the optical transparency is between 80%–92% in the visible range [103]. The thickness of the silicon nitride layers used, was 10 nm, which reduces the simulated thickness of the underlying zinc oxide layer by about the same amount (10 nm). The reason for this is the refractive indices of Si_3N_4 ($n = 2.04$) and of ZnO ($n = 2.01$) are nearly identical. In some experimental realisations this protection layer was omitted for simplicity reasons, as it has no influence to the optical properties of the whole multilayer stack and the layers did not have to stand industrial handling.

During the optimisation of the layer thicknesses by simulation and deposition two strategies were followed. The first one was to optimise the layer thicknesses in such a way, that a multilayer system with a low energy load coefficient τ_e/τ_v and a stable hue of reflectance colour for all angles of light incidence would be obtained. The second was to find a layer stack with a very small energy load coefficient, without taking the colour of the transmitted or the reflected light into account. The results of those optimisation strategies will be discussed in the following two sections.

5.2.2.1 Optimisation towards Energy Load Coefficient and Colour

The spectral transmittance for the first case, where the hue of the reflected light and the energy coefficient have been taken into account during the optimisation, is shown in figure 5.15 by the red curve in comparison to the theoretical transmittance $\tau_{min}(\lambda)$ given by the black dotted curve for perpendicular light incidence. The coating was deposited on a 4 mm float glass without the silicon nitride protection layer. The energy load coefficient for this coating is determined to $\tau_e/\tau_v = 0.398$ for perpendicular incidence of light. The difference to the theoretical limit of $\tau_e/\tau_v = 0.334$ can be explained by the discrepancies between the theoretical and the measured spectral transmittance in the wavelength range $\lambda = 600 \text{ nm} - 800 \text{ nm}$. For those wavelengths the measured transmittance is higher than the theoretical curve. Since the complete spectral transmittance of the coating is broadened towards the infrared in comparison to the theoretical, this difference between the energy load coefficient is expected. The evolution of the transmittance with increasing angle of light incidence is given in figure 5.16, showing that the transmittance of the coating decreases. For angles smaller than 60° the double peaked shape of the transmittance still exists, although the ratio between the dip and the peaks decreases. When the angle of light incidence is further

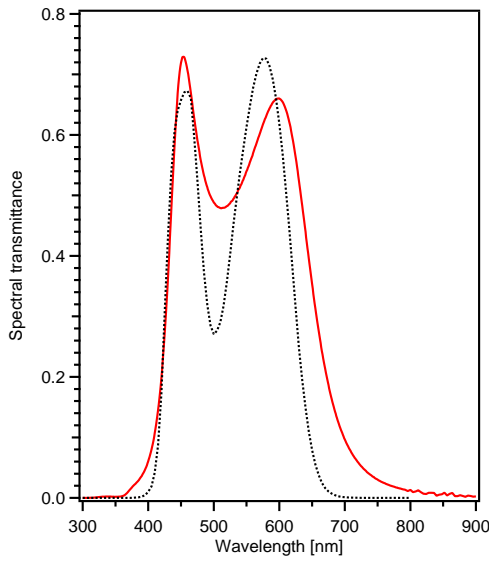


Figure 5.15: The red curve shows the spectral transmittance of the multilayer, which was optimised to have a low energy load coefficient in combination with a constant hue for the reflected light from the glass side of the coating. For comparison the theoretical spectral transmittance (black, dotted curve) is shown.

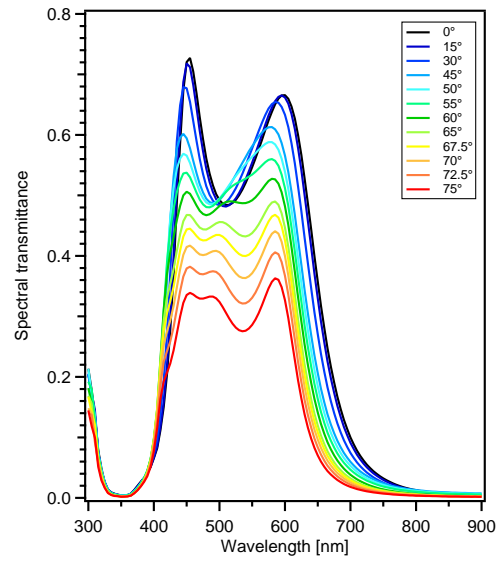


Figure 5.16: The angular dependence of the spectral transmittance of a multilayer design made of Ag and ZnO layers with thin TiO_x buffer layers to prevent the oxidation of the silver layers. The different colours give the spectral transmittance for the different angles of light incidence. The increase of the transmittance for $\lambda < 350$ nm is an instrumental artefact.

increased the dip of the curve first vanishes before a new dip is appearing at larger wavelengths. The infrared wavelength edge of the transmittance is shifting to smaller wavelengths for increasing angles of light incidence, but the steepness is not changed. The left edge towards the ultraviolet is not changing, when the angle of light incidence is varied.

Since the transmittance of this coating changes with varying angle of light incidence, an influence on the energy load coefficient can be expected. Due to the fact, that the infrared wavelength edge is shifting to smaller wavelengths the energy load coefficient should reduce. The evolution of the light transmittance τ_v (red), the solar direct transmittance τ_e (blue) and the energy load coefficient τ_e/τ_v (green) is given in figure 5.17 for different angles of light incidence. The light transmittance is constant for small angles, whereas the solar direct transmittance is decreasing. This leads to a reduction of the energy load coefficient, which is desirable since sun light usually is not penetrating perpendicular through the glass facade of a building. For this coating the smallest energy load coefficient is obtained at $\varphi = 60^\circ$ having a value of 0.373, as can be seen in figure 5.17. For all angles greater than 55° the light transmittance τ_v is greater than the desired minimum value of 0.5 defined in chapter 3.

The influence on the colours of the transmitted and reflected light due to the changes of the spectral transmittance are shown in figure 5.18 for varying angles of light incidence.

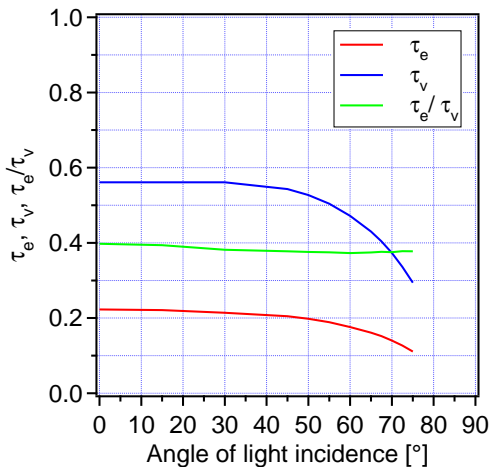


Figure 5.17: The evolution of the light transmittance $\tau_v(\varphi)$ (blue), the solar direct transmittance $\tau_e(\varphi)$ (red) and the energy load coefficient $\tau_e(\varphi)/\tau_v(\varphi)$ (green) for different angles of light incidence for the design composed of ZnO and Ag, that was optimised to have a stable colour and a low energy load coefficient.

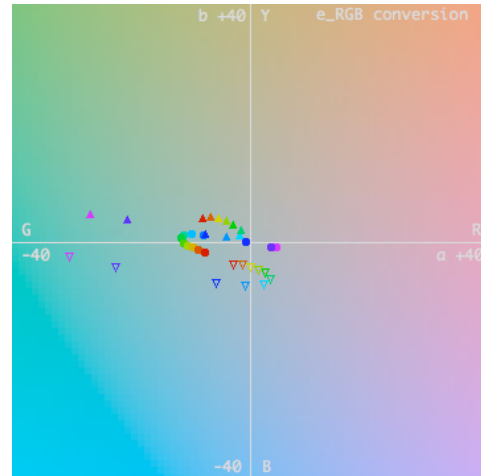


Figure 5.18: Representing the colour evolution in the CIE Lab colour space at constant luminosity of the transmittance (full circle), reflectance glass side (full triangles) and reflectance layer side (empty triangles) if the angle of light incidence is changed. For the smallest angle a purple symbol and for the largest a red symbol is used.

The colours are presented in the ab -plane of the CIE Lab coordinate system, where the value of L (luminosity) was chosen arbitrarily to $L = 70$ for convenient graphical representation. The filled circles represent the values for the transmitted light, the triangles, full and empty, represent light reflected from the glass and from the layer side of the coating, respectively. The colour code of the symbols is going from purple smallest to red largest angle.

The light transmitted through this coating is colour neutral for an angle of light incidence of $\varphi = 0^\circ$. The values $a = 4.5$ and $b = -1.1$ are in the range defined by $|a| < 5$ and $|b| < 5$, which is still recognised as colour neutral by the human eye. Although the $|a|$ -values already exceed the neutral range for an angle of $\varphi = 30^\circ$, the colour of the transmitted light is a very light green, since the $|b|$ -values are always smaller than 5. The colour values of the light reflected from the glass side of the deposited coating are all in one quadrant. Therefore the hue of the outside reflection is constant for this coating, as intended by the development done with simulations. The values are $-27.0 < a < -1.6$ and $1.0 < b < 4.8$ giving a bright green reflection. Besides the colour stability of this coating another advantage is, it has a light transmittance of $\tau_v = 0.561$ for perpendicular incidence, which is higher than the light transmittance of the described enhanced bandpass filter, which only was 0.504.

The colour variation and the energy load coefficient τ_e/τ_v of this ZnO – Ag coating is similar to that of the TiO₂ – Ag – SiO₂ coating described earlier. The advantage of this design is it contains less layers and therefore the industrial serial production of

this coating is more realistic. Furthermore the layer thicknesses of the metal oxide are larger and therefore less sensitive to production fluctuations.

5.2.2.2 Optimisation towards Energy Load Coefficient Only

For the next coating based on the metal-dielectric bandpass filter the thicknesses of the different layers were adjusted with the aim to obtain a coating, that has an energy load coefficient, which is nearly as small as the one theoretically calculated. The layer sequence of this coating is the same as the one given in figure 5.14, again without the silicon nitride protection layer. During the simulations no effort concerning the values or the angle dependancy of the colour of the transmitted and the reflected light was made, as the focus was only on the energy load coefficient. The spectral transmittance (red) of this coating for perpendicular light incidence is shown in figure 5.19 together

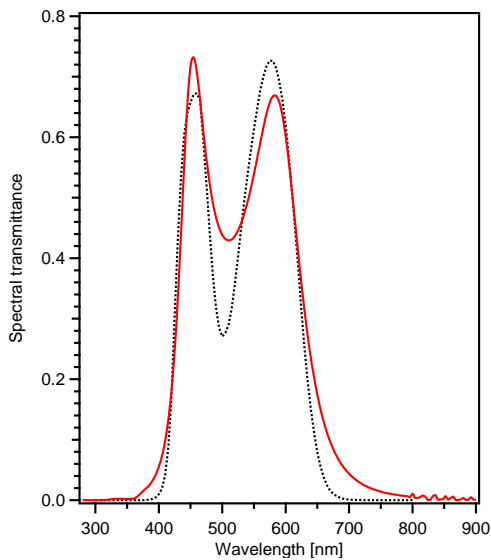


Figure 5.19: The red curve shows the spectral transmittance of the multilayer optimised to have a low energy load coefficient while the colour of the spectral reflectance was not taken into account during optimisation. For comparison the theoretical spectral transmittance (dotted, black line) is shown.

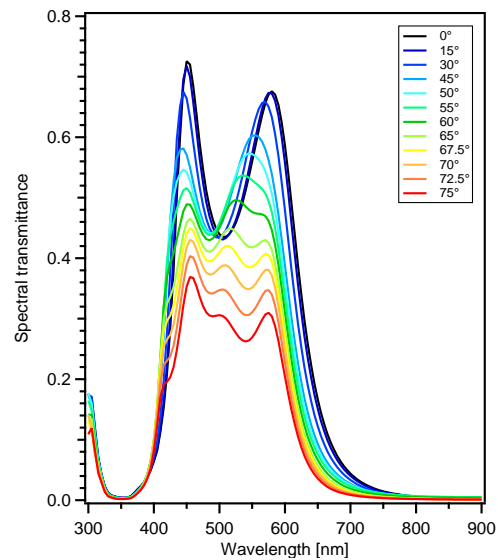


Figure 5.20: The angular dependence of the spectral transmittance of a multilayer design consisting of Ag, ZnO and thin TiO_x as buffer layers only optimised to have a very low energy load coefficient neglecting the colour properties during the simulations. The different colours give the spectral transmittance for the different angles of light incidence. The increase of the transmittance for $\lambda < 350$ nm is an instrumental artefact.

with the theoretical transmittance τ_{min} (black, dotted). Compared to the coatings discussed before the spectral transmittance is very close to the theoretical curve. Compared to the coatings discussed before the spectral transmittance is very close to the theoretical curve.

The main differences are the transmittance values of the peaks ($\lambda = 450$ nm and 560 nm) and the dip ($\lambda = 500$ nm). Furthermore, the fadeout of the steep edge at 625 nm is less abrupt, leading to higher values between 640 nm and 800 nm. Due to these differences the energy load coefficient of this coating should be higher than the theoretical one. With an energy load coefficient of $\tau_e/\tau_v = 0.368$ this coating is relative close to the theoretical value of 0.334 compared to the others which were described. This means an improvement of 23% in comparison to the best 25% of the commercial sun protection glasses on the market.

By comparing the spectral transmittance of this coating with the one of the previous described coating in figures 5.10 and 5.15, the reasons for the improvement to the energy load coefficient are obvious. The edge towards the infrared light of this coating is at shorter wavelengths $\lambda = 630$ nm and is nearly equal to the theoretical curve. Like this the amount of invisible infrared light, that contributes only to the solar direct transmission τ_e , was reduced to a minimum.

In figure 5.20 the angular dependence of the spectral transmittance is shown. As already shown for the previous described coatings the shape of the transmittance is conserved, when the angle of light incidence is increased from 0° to 60° . Although the shape is conserved, the whole curve is compressed since the infrared edge is shifted towards smaller wavelengths. Like this the wavelengths position of the peaks and the dip are changed, which should influence the colour appearance of the transmitted and the reflected light of this coating. The angular dependence of the transmittance further shows, that the light transmittance τ_v is decreasing with increasing angle.

The influences of the changing shape of the spectral transmittance on the visible light transmittance τ_v (blue), the solar direct transmittance τ_e (red) and the energy load coefficient τ_e/τ_v (green) are shown in figure 5.21. The light transmittance of this coating is 0.531 for 0° of light incidence and stays above the 0.5 mark until an angle of 40° is reached. Since the solar direct transmittance τ_e also decreases with increasing angle, changes to the energy load coefficient τ_e/τ_v are expected. For zero angle of incidence it is 0.368 and then decreases with increasing angle. At 30° of light incidence the energy load coefficient has a value of 0.357, which is the smallest it gets. For greater angles it slowly increase till it reaches a value of 0.381 at 75° . Further the graph shows, that the energy load coefficient is smaller than 0.4 for all angles of incidence.

The colours of this coated glass are changing rapidly with the angle φ of light incidence as can be seen in figure 5.22. The values for the transmitted light are in the range $-23.6 < a < -2.8$ and $-7.6 < b < -1.4$, which shows the huge changes of the transmitted colour. But for 0° of light incidence the values $a = -2.8$ and $b = -2.8$

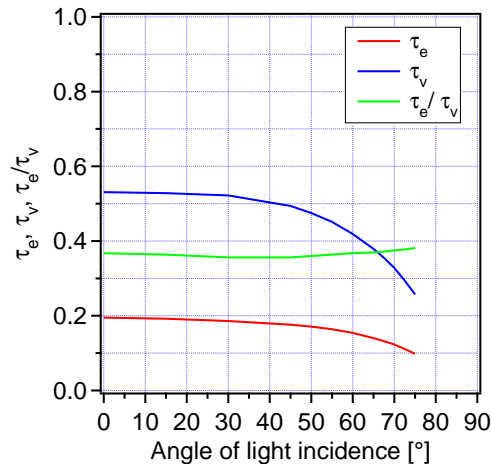


Figure 5.21: The evolution of the quantities light transmittance τ_v (blue), solar direct transmittance τ_e (red) and the energy load coefficient τ_e/τ_v (green) for different angles of light incidence for the ZnO–Ag design, which was only optimised to have a low energy load coefficient.

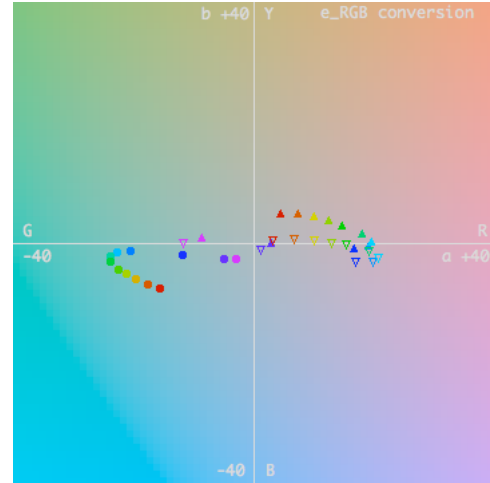


Figure 5.22: Representing the colour evolution in the CIE Lab colour space at constant luminosity, if the angle of light incidence is changed, of the transmittance (full circle), reflectance glass side (full triangles) and reflectance layer side (empty triangles) if the angle of light incidence is changed. For the smallest angle a purple symbol is used and for the largest a red symbol.

still fulfil the criteria of colour neutrality. Further the transmitted light has no yellow component for all angles of light incidence, since the b -value is always negative which was one of the evaluation criteria defined in chapter 3. The more obvious change in colour is that of the light reflected from the glass side and the layer side of this sun protection coating as the angle of light incidence is changed. The colour of the reflected light on the glass side starts of as a green ($a = -8.9$, $b = 1.0$) for perpendicular light incidence and changes very rapidly to an intensive red for large angles. For an angle $\varphi = 55^\circ$ the colour values of the reflected light are $a = 19.7$ and $b = 0.3$. Therefore, the boundary condition of having a constant hue of colour for all angles of light incidence is not fulfilled by this coating. The range of colour values for this coating is $-8.9 < a < 19.7$ and $-0.9 < b < 5.0$ for the reflected light on the glass side. The crucial point for the reflected light is that the colour value range contains two changes of sign and therefore the values are not in one quadrant, which is required to have a stable colour hue.

A constant hue of reflected colour is a critical point in the view of architects, which is not fulfilled by this coating. As one aim of this thesis was to develop a coating for sun protection glasses, that should be producible and that will be chosen by architects for their buildings, further optimisations concerning this coating were not made, although it has a very low energy load coefficient. If colour appearance would play a smaller role, the low energy load coefficient of this coating could have been further reduced in

additional iteration steps, by reducing the fadeout at around 700 nm drastically. To overcome the problem of colour variation of the reflected light, the balance between reflected and absorbed light must be changed. Further the amount of green light reflected must be increased, which would mean the dip of the spectral transmittance at $\lambda = 550$ nm must get deeper, as the light which is not transmitted is mainly reflected in these bandpass designs.

5.2.3 Influence of the Number of Silver Layers on the Spectral Properties of the Coatings

Since commercial sun protection glasses only contain two silver layers, it was of interest to verify, if it is possible to make coatings of the same quality only having two silver layers. A coating like this is based on the single cavity Fabry-Perot filter, described in chapter 2.4, which is made of two mirror layers (silver) and a spacer (zinc oxide). The advantage of using two silver layers would be, the total amount of layers needed to construct the bandpass filter would be reduced and this would make the industrial realisation of such a coating easier. In order to find out, if the theoretical spectral transmittance τ_{min} could be realised with a coating only containing two silver layers, a

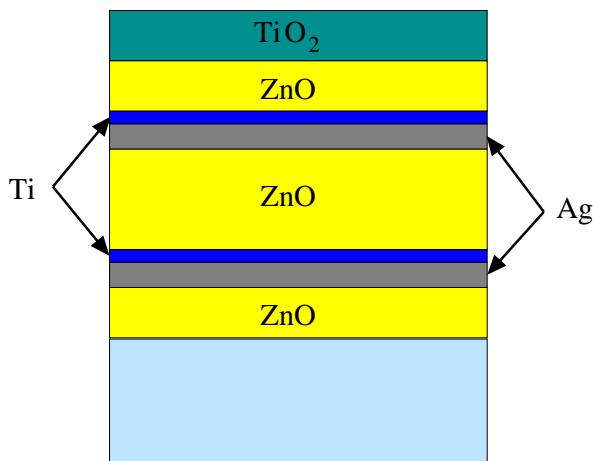


Figure 5.23: Schematic drawing of the layer stack used for the single cavity coatings with zinc oxide and two silver. The thin titanium layers were introduced to prevent the oxidation of the silver layers during the deposition of the following ZnO layers, as investigated in chapter 5.1.2. The titanium layers are oxidised during the following deposition to titanium dioxide.

series of simulations were made. The simulations have shown that it should be possible, but that many difficulties will have to be dealt with. The layer sequence used for the simulations and the experiments is given in figure 5.23.

In this layer sequence the zinc oxide between the glass and the first silver layer was already introduced, which is needed to increase the sticking coefficient between the glass and the multilayer. Further the buffer layers made of titanium to prevent the oxidation of the silver during the following reactive sputtering deposition, which was investigated in chapter 5.1.2, are also added. The last titanium oxide layer was used to protect the multilayer system. Instead of the preferable

silicon nitride layer a titanium dioxide layer was used here, as it was convenient for the experimental studies to use the same material as for the buffer layers or to omit it.

The spectral transmittance $\tau(\lambda)$ for perpendicular light incidence of the above given two silver layer coating is shown in figure 5.24. The measured (red) and the theoretical (black, dotted) spectral transmittance are very similar. An important difference to the coatings described in the two previous sections is, that the light transmittance was reduced to $\tau_v(0^\circ) = 0.41$. This light transmittance is much lower than the value 0.5 defined in the evaluation criteria in chapter 3 for the coatings with three silver layers. When the quality of the different coatings is compared, it is important to keep this in mind. The reason for this is, a lower light transmittance τ_v is equivalent to edges that need to be less steep towards the ultraviolet or the infrared range of the spectrum. A challenge in realising the theoretical spectral transmittance $\tau_{min}(\lambda)$ are the steep slopes and the difference between the transmittance value of the dip and the peaks being so extreme. This is also reduced, if the light transmittance is lowered. From this follows, in theory the realisation of the spectral transmittance investigated in this thesis should be reached easier, if the light transmittance is lowered from 0.5 to 0.4.

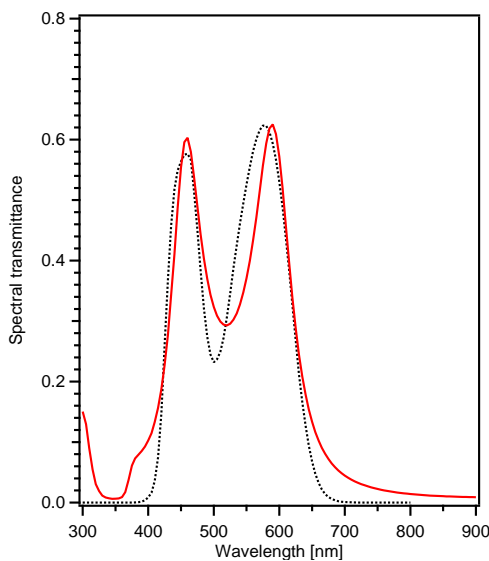


Figure 5.24: The red line shows the spectral transmittance of the multilayer which only contains two silver layers and not as the previous described three. For comparison the theoretical ideal spectral transmittance (dotted, black line) is shown. The increase of the transmittance for $\lambda < 350$ nm is an instrumental artefact.

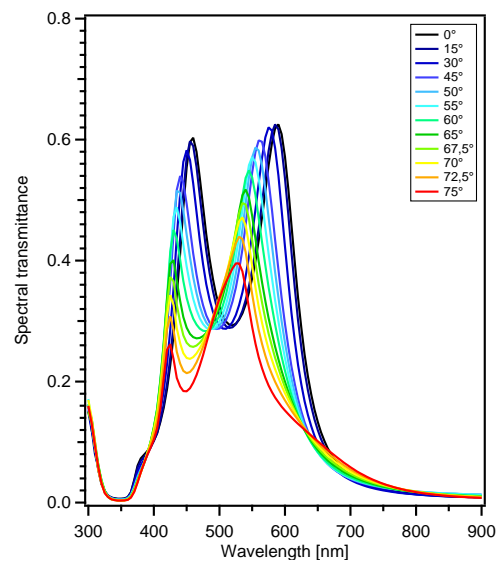


Figure 5.25: The angular dependence of the spectral transmittance of a multilayer design with 2 Ag, 3 ZnO and 2 thin TiO_x buffer layers. The different colours give the spectral transmittance for the different angles of light incidence. The increase of the transmittance for $\lambda < 350$ nm is an instrumental artefact.

The theoretical value of 0.334 for the energy load coefficient τ_e/τ_v is not reached by this coating since the shoulder for wavelengths greater 750 nm has higher transmittance values than the theoretical curve (see figure 5.24). The fact is, this part of the spectrum

only contributes to the solar direct transmittance τ_e , which ought to be as small as possible in order to achieve a small energy load coefficient. The hump at 400 nm further contributes to the solar direct transmittance, which also directly leads to an increase of the energy load coefficient τ_e/τ_v . The energy load coefficient of this coating only containing two silver layers is $\tau_e/\tau_v = 0.394$ for perpendicular light incidence. However, in comparison to the other coatings this is high, especially after the light transmittance τ_v was reduced from over 0.5 to 0.4, but in comparison to the sun protection glasses on the market, with an energy load coefficient of $\tau_e/\tau_v \geq 0.429$, it is still an improvement.

The evolution of the spectral transmittance, if the angle of light incidence is increased is shown in figure 5.25. Already small changes to the angle of light incidence φ cause significant changes to the spectral transmittance. The second peak at 600 nm for perpendicular incidence (0°) is shifting to smaller wavelengths with increasing angle and at the same time the intensity of this peak decreases. The changes to the other peak in the blue region of the spectrum are even more drastic. The intensity is diminishing until the peak is very small for an incident angle of $\varphi = 75^\circ$. The dip at around 500 nm is also object to change, since the two peaks are shifting if the angle of incidence is varied. Those extreme changes of the spectral transmittance leads to the conclusion that the energy load coefficient and the colours of the transmitted and reflected light should also exhibit great changes with varying angle of light incidence.

The influence of the changes on the quantities light transmittance τ_v (blue), solar direct transmittance τ_e (red) and energy load coefficient τ_e/τ_v (green) are shown in figure 5.26 for different angles of light incidence. The energy load coefficient τ_e/τ_v of this coating is decreased with increasing angle of incidence until it reaches the minimum value of 0.364 at an angle of $\varphi = 55^\circ$. For large angles ($\varphi > 55^\circ$) it raises again and even exceeds the value for perpendicular to become 0.396 if light penetrates the coated glass at an angle of 75° . The light transmittance τ_v is for angles smaller than 50° approximately 0.4 and it reduces very rapidly for angles larger than 45° .

As already expected from the development of the spectral transmittance, the colours of the transmitted and reflected light of this coating are changing quickly, if the angle of light incidence is varied, as can be seen in figure 5.27. The colour of the transmitted light is not neutral for all the angles of investigation, as it is not fulfilling the requirement $|a| < 5$ and $|b| < 5$, defined during the simulations, which are described in chapter 3. The colour of the transmitted light for perpendicular incidence ($\varphi = 0^\circ$) is a pale red ($a = 7.8$ and $b = -4.5$) and therefore not fulfilling the colour neutrality. If the angle is increased, at which the light is penetrating through the glass, the colour changes to colour neutrality ($a = -1.5$ and $b = -3.9$) at $\varphi = 30^\circ$ to continue

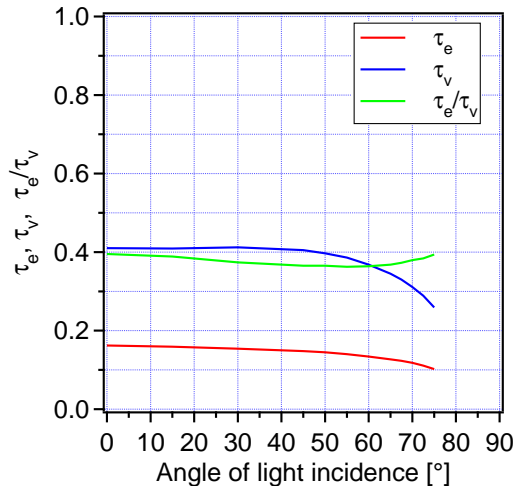


Figure 5.26: The evolution of the quantities light transmittance $\tau_v(\varphi)$ (blue), solar direct transmittance $\tau_e(\varphi)$ (red) and the energy load coefficient $\tau_e(\varphi)/\tau_v(\varphi)$ in green for different angles of light incidence for the design with only two silver layers.

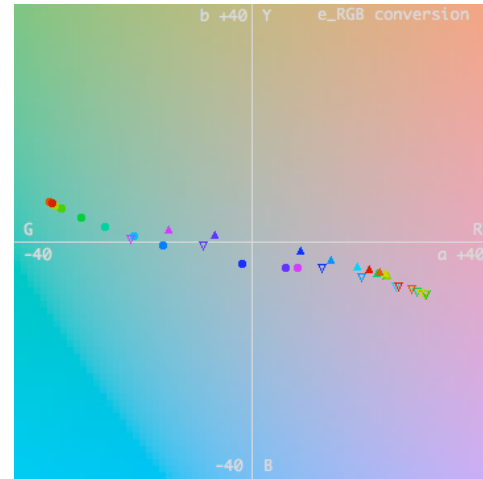


Figure 5.27: Representing the colour evolution in the CIE Lab colour space at constant luminosity of the transmittance (full circle), reflectance glass side (full triangles) and reflectance layer side (empty triangles) if the angle of light incidence is changed. For the smallest angle a purple symbol is used and for the largest a red symbol.

to an intense green ($a = -33.8$ and $b = 6.5$) for large angles ($\varphi \geq 67.5^\circ$). The colour of the reflected light from the glass side experiences the opposite change. For small angles ($\varphi = 15^\circ$) the reflected light is green ($a = -14.2$ and $b = 2.1$) to change to an intensive red (i.e., $a = 22.8$ and $b = -5.6$ for $\varphi = 65^\circ$) for large angles. The colour variations of the reflected and the transmitted light have extreme values and therefore they are not fulfilling the boundary conditions defined in chapter 3. Those boundary conditions were defined to be able to evaluate if a coating has chances to compete with existing coatings in respect to their colour appearance. With respect to the aim to lower the energy load coefficient even this coating is an improvement in comparison to commercial sun protection glasses on the market.

Another problem of two silver layer coatings in comparison to the ones with three silver layer is that the spectral reflectance in the infrared region of the solar spectrum is lower in the case of only two silver layers. This can be seen in figure 5.28, where the measured spectral reflectance of the two coatings, one with two and the other one with three silver layers, is shown. The shown reflectance is measured on the layer side of the coated glass, as this gives the reflectance of the coating without the absorption losses in the float glass. The differences in this graph in the visible and ultraviolet region ($\lambda < 800$ nm) are of minor interest for this consideration, since in this region the spectral transmittance of the coatings are also different. The interesting part of this graph is the large wavelength range $\lambda > 800$ nm. In this region the spectral

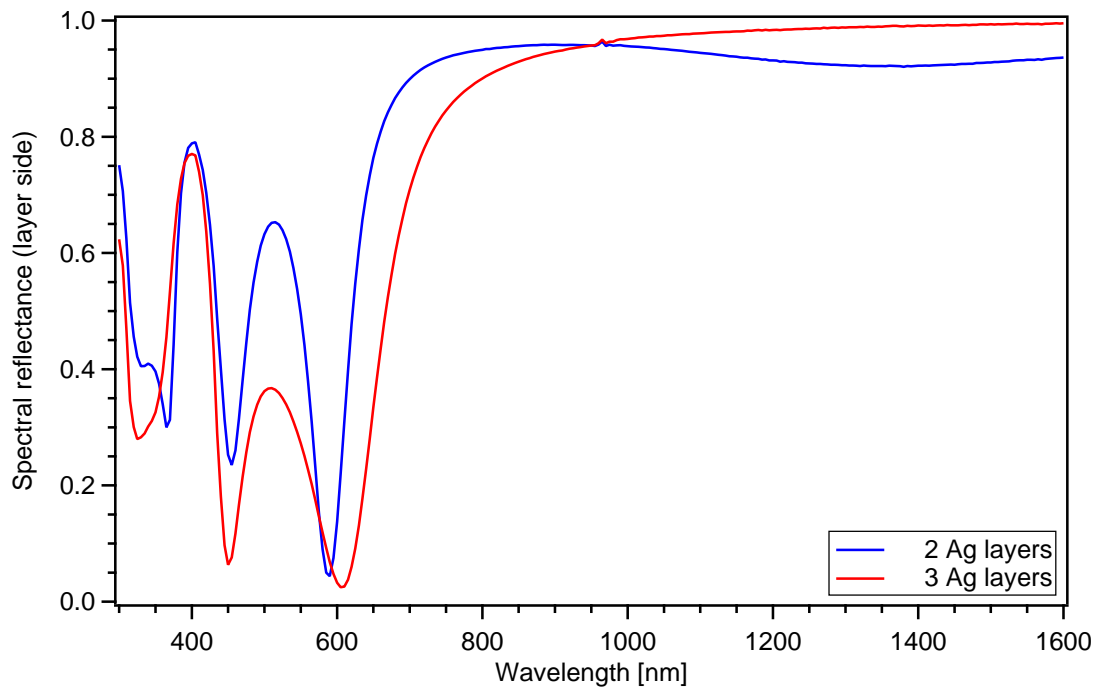


Figure 5.28: The spectral reflectance of two different coatings, one containing two silver layers (blue) and the other containing three (red) measured for nearly perpendicular light incidence ($\varphi = 7.5^\circ$). The graph shows, that the reflectance in the infrared ($\lambda > 800$ nm) is higher if a coating contains more silver layers. The origin of the little peaks at $\lambda = 1000$ nm is a change of detector in combination with a filter change of the spectrophotometer.

transmittance is independent of the coating design zero and therefore has no influence on the reflected light. It can easily be seen, that the spectral reflectance in the infrared of the three silver layer coating is much higher than the one of the two silver layer coating. For larger angles of light incidence (not shown) this difference is even more pronounced. A high infrared reflectance is of great importance as the heat input of the sun, as can be seen in the solar spectrum given in figure 2.3, is still very high for wavelengths greater than 800 nm. This is of importance, as all the light that is not transmitted or reflected will be absorbed, as already described in the radiation distribution equation (eq. 2.1). Since the transmittance is zero for those wavelengths the radiation that is not reflected is absorbed by the layer. The light absorbed is converted into heat, that is reradiated from the coating. Part of the reradiated heat will enter the building and like this increases the secondary internal heat transfer factor q_i . The secondary internal heat transfer factor q_i describes the additional heat which is emitted and convected to the interior of the building due to absorption of solar radiation in the glass panes [24]. By only evaluating the energy load coefficient this important contribution is neglected. This shows the energy load coefficient τ_e/τ_v is good for comparing different coatings as long as they possess an infrared reflectance that is nearly equal to one.

The difference between the infrared reflectance of the coating containing only two silver layers and of the one with three silver layers is based on the total amount of silver used in the different coatings. When the light transmittance τ_v is equal for a two and a three silver layer system, the total amount of silver in the coating can be higher if the silver amount is split up into more layers [26]. In the given example in figure 5.28 the total amount of silver for the two silver coating would be even lower if it also had a light transmittance $\tau_v = 0.5$ as the three silver coating. Silver is in charge of the reflection of the infrared radiation, as silver is a metal containing free electrons, as already explained in chapter 2.2. From this follows the larger the total amount of silver a coating contains is, the higher the reflectance in the infrared wavelength region will be. On the other hand if the amount of silver is increased the spectral transmittance in the visible part will decrease, till it gets opaque as in the case of bulk silver. The visible light transparency, but not that of the infrared light, of thin silver layers can be improved by covering them with a transparent metal oxide layer. This leads to the conclusion, if silver is split up in several layers all covered with a transparent metal oxide layer which reduce the reflectivity of silver in the visible, the total amount of silver can be increased leading to a higher infrared reflectance without changing the transparency.

To prove that this is valid for the two investigated multilayer coatings having the spectral reflectance shown in figure 5.28, the light transmittance τ_v and the total silver thickness d_{Ag} are given in the table below:

Number of Ag layers	d_{Ag}	τ_v
2	48.3 nm	0.41
3	63.7 nm	0.56

This proves that the coating containing three silver layers, with an infrared spectral reflectance nearly equal to one, has a higher light transmittance τ_v , although the total thickness of silver is higher than for the two silver layer coating. An example for a single silver layer imbedded in two titanium dioxide layers is given by J.C.C. Fan et al., showing that the infrared reflectance of an 18 nm thick silver layer is very low in the near infrared region [52].

Summarising the above described experimental results show, why double cavity band-pass filters containing three silver layers should be favoured instead of the two silver layer coatings as used in the industrial production. The double cavity filters have a higher infrared reflectance, that is nearly equal to one, and the colour of the transmitted and the reflected light is prevailing more stability. Further the energy load coefficient

τ_e/τ_v is lower or equal, even if the light transmittance of the investigated coatings was higher.

This investigation gives rise to the question, if introducing a fourth silver layer to the coating could even further improve the properties of sun protection glasses having a spectral transmittance that is similar to the theoretical spectral transmittance τ_{min} , which was developed by Professor Oelhafen [20, 21]. First simulations have shown, that the introduction of a fourth silver layer would further reduce the energy load coefficient τ_e/τ_v of the coatings, as it is possible to achieve steeper slopes. Due to this the contribution of the invisible infrared light could be further minimised, which leads to a reduction of the solar direct transmission τ_e . In order to find out, if this is only a theoretical improvement or not, experimental investigations are necessary. A problem of introducing an extra silver layer is, the thicknesses of some silver layers are reaching the critical thickness of 10 nm, for which silver is not forming a continuous film but interlinking islands (see chapter 5.1.1). Further those simulations did not take the evolution of the colour for changing angles of light incidence into account. To be able to give a clear statement, if four or even more silver layers are an improvement further simulations and experimental investigations have to be made.

Chapter 6

Conclusions

New coatings for sun protection glasses were developed which reduce the energy input to a building due to the infrared radiation of the sun. The prerequisite of those coatings was, they ought to have a spectral transmittance which is equal to the theoretical minimised transmittance τ_{min} developed by P. Oelhafen [20, 21] and described in chapter 2.1. The coating designs are based on the Fabry-Perot principle for thin film interference filters. Those bandpass filters are made of multilayer systems containing metal and metal oxide layers. For the realisation of the spectral transmittance τ_{min} two different bandpass filters were used. They are made of materials which are standard in the glass industry.

- The **metal-dielectric bandpass filter** contains thin film spacers of zinc oxide which are surrounded by silver mirrors.
- The **enhanced metal-dielectric bandpass filter** is made of silicon dioxide spacers which separate the mirrors of the filter. In this case the mirrors are made out of two layers, a silver and a titanium dioxide layer. Like this the advantages of a metal mirror are combined with those of a dielectric multilayer interference mirror with a high ration of refractive indices.

The obtained energy load coefficient τ_e/τ_v for the new developed coatings are shown in figure 6.1 in comparison to the sun protection glasses on the market given in the database of the University of Basel [25]. In this context it is important to keep in mind that the developed coatings are only single coated glass panes and not a complete double glazing. By adding a second glass pane the values of the energy load coefficient τ_e/τ_v would reduce further. The measured data points for the new coatings are divided into two groups: The red markers correspond to coatings containing three silver layers independent of the bandpass design which was used. The energy load coefficient for

coatings only containing two silver layers is shown in green. The data points marked with an additional yellow dot are corresponding to the coatings discussed in detail chapter 5.2.

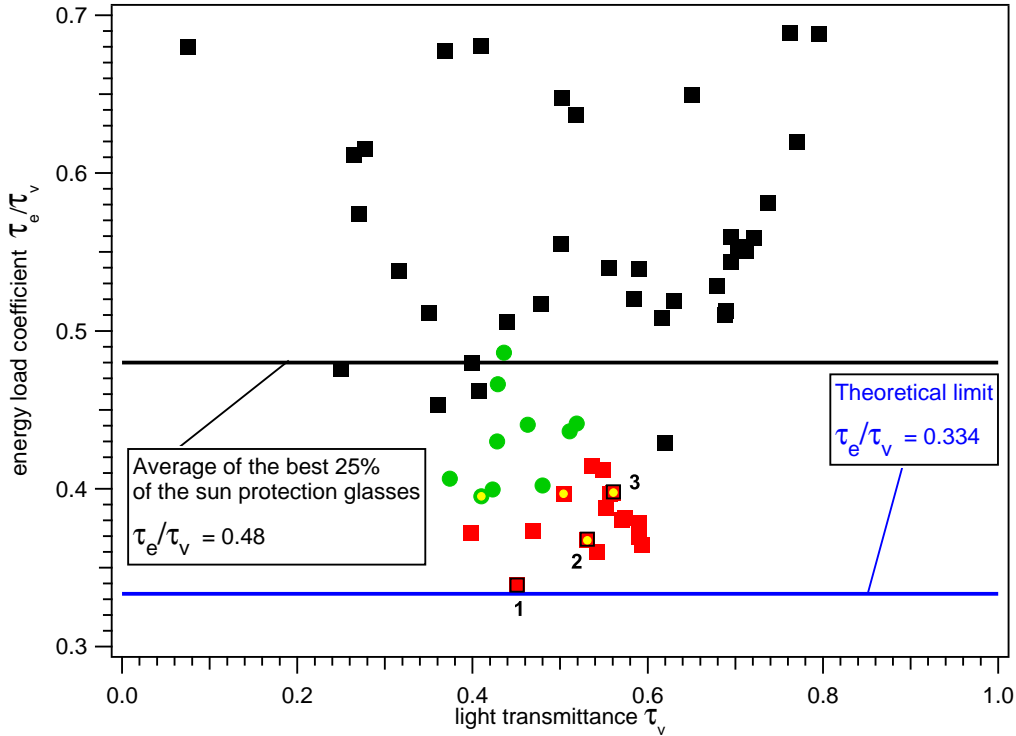


Figure 6.1: The energy load coefficient τ_e/τ_v for perpendicular light incidence plotted over the light transmittance τ_v . The data obtained for a variety of sun protection glasses on the market are shown in black. The values for the new developed coatings are given in red for the three silver layers and in green for the two silver layer coatings. The data points which are marked with an additional yellow dot correspond to the coatings discussed in chapter 5.2. The line in black marks the limit for commercial sun protection glasses given by the average of the best 25% [22]. The blue line gives the theoretical limit developed by P. Oelhafen [20, 21].

The graph shows that all the new coatings which contain three silver layers have an energy load coefficient τ_e/τ_v that is lower than the current limit for commercial sun protection glasses, marked by the black line. In comparison the newly developed coatings having only two silver layers (green markers) are also better than most of the commercial sun protection glasses. In respect to the energy input they are an improvement, whereas the colour values are not meeting the requirements defined concerning the colour stability of the transmitted and the reflected light. Furthermore, the transmitted light is not colour neutral for small angles of light incidence.

The three coatings marked with the numbers 1 to 3, all containing three silver layers, should be highlighted here:

Coating 1: This coating, based on the metal-dielectrical bandpass filter, has an energy load coefficient of 0.339 which is nearly equal to the theoretically minimised

spectral transmittance τ_{min} . Due to the colour variations for the transmitted and the reflected light this coating was not taken into consideration for an further realisations. The transmitted light varies from a strong yellow-green to a bright green, whereas the reflected colours on the glass side vary from blue to purple.

Coating 2: The energy load coefficient of 0.368 belongs to the coating described in section 5.2.2.2 which was optimised to have a low energy load coefficient without taking the colours into account. Nevertheless the colour values of this coating are more satisfying than for the coating marked with 1. The transmitted colour of the energy optimised coating changes from neutral to a blue. The colour of the reflected light on the glass side is varying from green to red for increasing angle of light incidence. This is an effect that is not yet tolerated by architects.

Coating 3: This coating has a low energy coefficient of 0.398 in combination with satisfying colour values. The colour of the reflected light on the glass side is green, independent of the angle light incidence, as described in section 5.2.2.1. The transmitted light is colour neutral for small angles and changes for increasing angles to a pale green which is barely detectible for the human eye.

Outlook and Improvements

The data points in figure 6.1 show that the theoretical limit (blue line) of the spectral transmittance τ_{min} is not yet reached. It is important to keep in mind that the theoretical transmittance τ_{min} is based on standard spectral distributions like the spectral photopic luminous efficiency $V(\lambda)$ and the colour-matching functions \bar{x}_λ , \bar{y}_λ , \bar{z}_λ . During the development of this transmittance the properties and limits of thin film multilayer coatings were not taken into account. Possible measures to reach the theoretical limit of the energy load coefficient $\tau_e/\tau_v = 0.334$ without changing the preferred light transmittance of $\tau_v \geq 0.5$ would be to increase the number of layers in the coating. This was verified by first simulations. For a multilayer system consisting of 28 layers a simulated energy load coefficient of 0.35 was determined. The advantage of a higher number of layers is that the total amount of silver can be raised if the light transmittance is kept constant, which leads to a higher infrared reflectance as shown in chapter 5.2.3. A problem of a large number of layers is, that the feasibility of such multilayer systems is not guaranteed as the thickness of some of the layers will be below or near the percolation threshold. Another problem is the producibility of such coatings in a serial production as the tolerances for the layer thicknesses will be very small, which will lead to an increase of the costs. An alternative solution would be to

use new materials, like nano-composites or doped semiconductors. For this solution the costs and the practicability are subject of investigation.

Another way to reduce the energy load coefficient τ_e/τ_v is to reduce the light transmittance τ_v of the sun protection glass. The value of 0.5 for the light transmittance is based on the classic experience where the aim was to use as much daylight as possible. In the case of glass facades the light transmittance can be lowered as the daylight income is anyway higher since the whole facade is made of glass and not partly of brick work. Due to this it is likely that the light transmittance can be reduced to $0.25 \leq \tau_v \leq 0.3$. The advantage of lowering the light transmittance is that the slopes towards the infrared and the ultraviolet spectrum need to be less steep. Exactly those steep slopes and the huge difference between the three extrema are the challenge and the critical point in the experimental realisation of the theoretical minimised transmittance τ_{min} by P. Oelhafen [20, 21]. Another advantage of the reduction of the transmittance is that the total thickness of the silver layers can be higher. This leads to a higher infrared reflection and to thicker and therefore denser silver layers in the multilayer coating.

A Sustainable Contribution to Our Future

Blocking the near-infrared light coming from the sun is the most important attribute of sun protection glasses. This feature is wanted during the summer as it reduces the cooling load, but during winter it increases the energy needed for heating. This is true, but buildings with glass facades are usually commercial and institutional buildings where the heating needs are low, as a huge amount of heat is produced by the office equipment. Summing up, the losses during winter and the gains during summer due to sun protection glasses, the annual energy balance of such buildings is reduced. A fact is the period of cooling is longer than that of heating which is pushed due to the heat load of the office equipment. Furthermore, due to climatic changes and global warming summers will be come hotter and winters less severe in the future. This will lead to an increase of the gain during summers as the cooling load will rise and will increase the importance of sustainable buildings even further.

Something that should not be underestimated is the economic development in the asian countries. In those countries the architectural trend to large glass facades is just at the beginning. Furthermore, the climatic prerequisites in these countries are different, as those countries are located in the tropical region of our earth. In those regions it is not necessary to gain solar infrared radiation to support heating as they have no

cold periods where heating is necessary at all. Reducing the temperature in buildings in those regions is of great importance as they also have to face high humidity.

This shows the market for sun protection glasses with a low energy load coefficient is huge, and it is still increasing, and just at the beginning. Therefore, new coatings for sun protection glasses are an important measure to reduce energy consumption and to protect our climate.

Appendix A

Optical Functions and Quantities

A.1 Solar Spectrum and Photopic Luminous Efficiency

The relative spectral distribution of the solar radiation $S_\lambda(\lambda)$ is the spectrum of the sun measured at the surface of the earth. It differs to the radiation emitted from the sun as some wavelengths get absorbed in the atmosphere.

The spectral photopic luminous efficiency $V_\lambda(\lambda)$ gives the ratio of the radiation flux at a wavelength of $\lambda = 555$ nm to that at a wavelength λ , when both radiation fluxes lead to the identical photopic impression of illumination.

The standard illuminant D_{65} intends to represent average daylight and has a correlated colour temperature of approximately 6500 K.

A.2 Light Transmittance and Direct Solar Transmittance

The characteristic values related to radiation are the light transmittance τ_v and the direct solar transmittance τ_e . They are gained by connecting the spectral transmittance $\tau(\lambda)$ of a glazing with standard functions as:

$D_\lambda(\lambda)$: relative spectral distribution of the standard illuminant D_{65}

$V_\lambda(\lambda)$: spectral photopic luminous efficiency

$S_\lambda(\lambda)$: relative spectral distribution of the solar radiation

$$\tau_v = \frac{\int_{380}^{780} D_\lambda(\lambda)\tau(\lambda)V(\lambda)d\lambda}{\int_{380}^{780} D_\lambda(\lambda)V(\lambda)d\lambda}$$

$$\tau_e = \frac{\int_{300}^{2500} S_\lambda(\lambda)\tau(\lambda)d\lambda}{\int_{300}^{2500} S_\lambda(\lambda)d\lambda}$$

They describe the ratio of radiation coming through the glazing to the incoming radiation.

Since the values D_λ , V_λ , τ and S_λ are all measured quantities, the integrals have to be changed to sums.

$$\tau_v = \frac{\sum_{380}^{780} D_\lambda(\lambda)\tau(\lambda)V(\lambda)\Delta\lambda}{\sum_{380}^{780} D_\lambda(\lambda)V(\lambda)\Delta\lambda}$$

$$\tau_e = \frac{\sum_{300}^{2500} S_\lambda(\lambda)\tau(\lambda)\Delta\lambda}{\sum_{300}^{2500} S_\lambda(\lambda)\Delta\lambda}$$

Appendix B

Electromagnetic Waves and Matter

B.1 Maxwell Equations

Considering a homogeneous isotropic, non magnetic ($\mu = 1$), medium of dielectric constant ε and conductivity σ . The *Maxwell equations* are

$$\begin{aligned}\operatorname{rot} \vec{H} &= \frac{d\vec{D}}{dt} + \vec{j} \\ \operatorname{rot} \vec{E} &= -\frac{d\vec{B}}{dt} \\ \operatorname{div} \vec{B} &= 0 \\ \operatorname{div} \vec{D} &= \varrho\end{aligned}$$

with the material equations

$$\begin{aligned}\vec{D} &= \varepsilon\varepsilon_0\vec{E} \\ \vec{B} &= \mu\mu_0\vec{H}\end{aligned}$$

with the electrical vector \vec{E} , the magnetic induction \vec{B} , the electrical displacement \vec{D} , the magnetic vector \vec{H} , the electrical current density \vec{j} , and the electric charge density ϱ . The first Maxwell equation in matter can be rewritten to

$$\operatorname{rot} \vec{H} = \varepsilon\varepsilon_0 \frac{d\vec{E}}{dt} + \sigma\vec{E} \quad (\text{B.1})$$

with $\vec{j} = \sigma\vec{E}$. When we now use the electrical vector of a wave, which has the form

$$\vec{E} = \vec{E}_0 \exp(-i\omega t)$$

calculate the derivative of it and substitute it back into the first Maxwell equation (B.1), we get:

$$\text{rot } \vec{H} = \left(\varepsilon \varepsilon_0 - \frac{\sigma}{i\omega} \right) \frac{d\vec{E}}{dt}$$

This equation looks similar to the Maxwell equation for insulators, just that the dielectric constant is complex. From this follows for the complex dielectric constant $\hat{\varepsilon}$

$$\hat{\varepsilon} = \varepsilon + i \frac{\sigma}{\varepsilon_0 \omega} = (n - ik)^2 \quad (\text{B.2})$$

where n is the real refractive index and k the extinction coefficient.

B.2 Drude Model

In an electric field the free electrons in a metal acquire an additional velocity and start to move more ordered in comparison to when no electrical field is applied [33]. The electron will still be subject to collisions. The whole motion can be described by a forced motion with a damping term:

$$m\ddot{\vec{r}} + m\beta\dot{\vec{r}} = e\vec{E}$$

where m is the mass, e the charge of an electron and β the damping constant.

To better understand the meaning of the damping constant β we first look at the stationary case where no electrical field is present. If $\vec{E} = 0$, we have

$$\ddot{\vec{r}} + \beta\dot{\vec{r}} = 0$$

with the solution:

$$\vec{r} = \vec{r}_0 - \frac{1}{\beta} \vec{v}_0 \exp(-\beta t) \quad \dot{\vec{r}} = \vec{v}_0 \exp(-\beta t)$$

In this case the electron starts with the velocity \vec{v}_0 and is slowed down in an exponential way, with the decay constant β . The time $\tau_c = 1/\beta$ is the relaxation time which is the average period of time between two scattering events.

If we now assume a time-harmonic field $\vec{E} = \vec{E}_0 \exp(-i\omega t)$, we get the following

solution:

$$\vec{r} = -\frac{e}{m(\omega^2 + i\omega_c \omega)} \vec{E}$$

This periodic motion gives rise to a current in the medium. If there are N free electrons per unit volume, the current density \vec{j} is

$$\vec{j} = eN\dot{\vec{r}} = \frac{Ne^2}{m(\omega_c - i\omega)} \vec{E}$$

Comparison with the definition $\vec{j} = \sigma \vec{E}$ leads to:

$$\sigma = \frac{Ne^2}{m(\omega_c - i\omega)} \quad (\text{B.3})$$

From this equation the relationship between the static value of the conductivity σ_0 and the collision frequency ω_c follows:

$$\sigma_0 = \frac{Ne^2}{m\omega_c} \quad (\text{B.4})$$

B.3 Plasma Frequency ω_p

The frequency dependence of the complex dielectric constant $\hat{\varepsilon}$ and of the complex refractive index \hat{n} is not only influenced by the contribution of the free electrons, and therefore by the frequency dependence of the conductivity σ , but also by the contribution of the bound electrons (the real dielectric constant ε). At low enough frequencies the contribution of the bound electrons is small compared to the contribution of the free electrons. In this case we can replace in the equation B.2 for the complex dielectric constant $\hat{\varepsilon}$ the real dielectric constant ε by 1 and the conductivity σ by the value of equation B.3, calculated above.

$$\hat{\varepsilon} = (n - ik)^2 = 1 - \frac{Ne^2}{\varepsilon_0 m} \frac{1}{\omega(\omega + i\omega_c)}$$

By introducing the plasma frequency ω_p

$$\omega_p = \sqrt{\frac{Ne^2}{\varepsilon_0 m}}$$

the equation for the complex dielectric constant $\hat{\epsilon}$ can be simplified to:

$$\hat{\epsilon} = 1 - \frac{\omega_p^2}{\omega(\omega + i\omega_c)} \quad (\text{B.5})$$

At the plasma frequency the reflectivity changes from no reflectance to a very high reflectance.

Bibliography

There are a many bibliography entries where all the authors are listed. The reason for this is a formal request of the publishers of these entries. Most of them are references to documents published by the Intergovernmental Panel on Climatic Changes where many different authors contribute to one topic.

- [1] Al Gore. *An Inconvenient Truth, The Planetary Emergency of Global Warming and What We Can Do About It*. Rodale, Emmaus PA, 2006.
- [2] J. Schneider. Die Enzyklopädie der extrasolaren Planeten - Der Interaktive Extrasolare Planeten Katalog. <http://exoplanet.eu/catalog.php>, April 2008.
- [3] H. Le Treut, R. Somerville, U. Cubasch, Y. Ding, C. Mauritzen, A. Mokssit, T. Peterson, and M. Prather. Historical overview of climate change. In S. Solomon, D. Qin, M. Manning, Z. Chen, M. Marquis, K. B. Averyt, M. Tignor, and H. L. Miller, editors, *Climate Change 2007: The Physical Science Basis. Contribution of Working Group I to the Fourth Assessment Report of the Intergovernmental Panel on Climate Change*. Cambridge University Press, Cambridge, United Kingdom and New York, NY, USA, 2007.
- [4] IPCC. Summary for policymakers. In S. Solomon, D. Qin, M. Manning, Z. Chen, M. Marquis, K. B. Averyt, M. Tignor, and H. L. Miller, editors, *Climate Change 2007: The Physical Science Basis. Contribution of Working Group I to the Fourth Assessment Report of the Intergovernmental Panel on Climate Change*. Cambridge University Press, Cambridge, United Kingdom and New York, NY, USA, 2007.
- [5] P. Forster, V. Ramaswamy, P. Artaxo, T. Berntsen, R. Betts, D. W. Fahey, J. Haywood, J. Lean, D. C. Lowe, G. Myhre, J. Nganga, R. Prinn, G. Raga, M. Schulz, and R. Van Dorland. Changes in atmospheric constituents and in radiative forcing. In S. Solomon, D. Qin, M. Manning, Z. Chen, M. Marquis, K. B. Averyt, M. Tignor, and H. L. Miller, editors, *Climate Change 2007: The Physical Science Basis. Contribution of Working Group I to the Fourth Assessment Report*

- of the Intergovernmental Panel on Climate Change*. Cambridge University Press, Cambridge, United Kingdom and New York, NY, USA, 2007.
- [6] K. L. Denman, G. Brasseur, A. Chidthaisong, P. Ciais, P. M. Cox, R. E. Dickinson, D. Hauglustaine, C. Heinze, E. Holland, D. Jacob, U. Lohmann, S. Ramachandran, P. L. da Silva Dias, S. C. Wofsy, and X. Zhang. Couplings between changes in the climate system and biogeochemistry. In M. Tignor, S. Solomon, D. Qin, M. Manning, Z. Chen, M. Marquis, K. B. Averyt, and H. L. Miller, editors, *Climate Change 2007: The Physical Science Basis. Contribution of Working Group I to the Fourth Assessment Report of the Intergovernmental Panel on Climate Change*. Cambridge University Press, Cambridge, United Kingdom and New York, NY, USA, 2007.
- [7] I. C. Prentice, G. D. Farquhar, M. J. R. Fasham, M. L. Goulden, M. Heinmann, V. J. Jaramillo, H. S. Kheshgi, C. Le Quéré, R. J. Scholer, and D. W. R. Wallace. The carbon cycle and atmospheric carbon dioxide. In J. T. Houghton, Y. Ding, D. J. Griggs, M. Noguer, P. J. van der Linden, X. Dai, K. Maskell, and C. A. Johnson, editors, *Climate Change 2001: The Scientific Basis. Contribution of Working Group I to the Third Assessment Report of the Intergovernmental Panel on Climate Change*. Cambridge University Press, Cambridge, United Kingdom and New York, NY, USA, 2001.
- [8] V. Ramaswamy, O. Boucher, J. Haigh, D. Hauglustaine, J. Haywood, G. Myhre, T. Nakajima, G. Y. Shi, S. Solomon, R. Betts, R. Charlson, C. Chuang, J. S. Daniel, A. Del Genio, R. van Dorland, J. Feichter, J. Fuglestvedt, P. M. de F. Forster, S. J. Ghan, A. Jones, J. T. Kiehl, D. Koch, C. Land, J. Lean, U. Lohmann, K. Minschwaner, J. E. Penner, D. L. Roberts, H. Rodhe, G. J. Roelofs, L. D. Rotstayn, T. L. Schneider, U. Schumann, S. E. Schwartz, M. D. Schwarzkopf, K. P. Shine, S. Smith, D. S. Stevenson, F. Stordal, I. Tegen, and Y. Zhang. Radiative forcing of climate change. In F. Joos and J. Srinivasan, editors, *Climate Change 2001: The Scientific Basis. Contribution of Working Group I to the Third Assessment Report of the Intergovernmental Panel on Climate Change*. Cambridge University Press, Cambridge, United Kingdom and New York, NY, USA, 2001.
- [9] K. E. Trenberth, P. D. Jones, P. Ambenje, R. Bojariu, D. Easterling, A. Klein Tank, D. Parker, F. Rahimzadeh, J. A. Renwick, M. Rusticucci, B. Soden, and P. Zhai. Observations: Surface and atmospheric climate change. In S. Solomon, D. Qin, M. Manning, Z. Chen, M. Marquis, K. B. Averyt, M. Tignor, and H. L. Miller, editors, *Climate Change 2007: The Physical Science Basis. Contribution*

- of Working Group I to the Fourth Assessment Report of the Intergovernmental Panel on Climate Change*. Cambridge University Press, Cambridge, United Kingdom and New York, NY, USA, 2007.
- [10] N. L. Bindoff, J. Willebrand, V. Artale, A. Cazenave, J. Gregory, S. Gulev, K. Hanawa, C. Le Quéré, S. Levitus, Y. Nojiri, C. K. Shum, L. D. Talley, and A. Unnikrishnan. Observations: Oceanic climate change and sea level. In S. Solomon, D. Qin, M. Manning, Z. Chen, M. Marquis, K. B. Averyt, M. Tignor, and H. L. Miller, editors, *Climate Change 2007: The Physical Science Basis. Contribution of Working Group I to the Fourth Assessment Report of the Intergovernmental Panel on Climate Change*. Cambridge University Press, Cambridge, United Kingdom and New York, NY, USA, 2007.
- [11] R. A. Moreno, R. Baron, P. Bohm, W. Chandler, V. Cole, O. Davidson, G. Dutt, E. Haites, H. Ishitani, D. Kruger, M. Levine, L. Zhong, L. Michaelis, W. Moomaw, J. R. Moreira, A. Mosier, R. Moss, N. Nakicenovic, L. Price, N. H. Ravindranath, H.-H. Rogner, J. Sathaye, P. Shukla, L. Van Wie McGroory, T. Williams, J. Corfee-Morlot, J. Edmonds, Ph. Fearnside, R. Friedman, F. Mullins, L. Solsbery, and Z. Quiguo. Residential, commercial and institutional buildings sector. In R. T. Watson, M. C. Zinyowera, and R. H. Moss, editors, *Technologies, Policies and Measures for Mitigating Climate Change*. IPCC Working Group II, Intergovernmental Panel on Climate Change, 1996.
- [12] C. A. Balaras, K. Droutsas, A. A. Argiriou, and D. N. Asimakopoulos. Potential for energy conservation in apartment buildings. *Energy and Buildings*, 31:143 – 154, 2000.
- [13] K. T. Chan and W. K. Chow. Energy impact of commercial-building envelopes in the sub-tropical climate. *Applied Energy*, 60:21 – 39, 1998.
- [14] M. Levine, M. Uerge-Vorsatz, K. Blok, L. Geng, D. Harvey, S. Lang, G. Levermore, A. M. Mehlwana, S. Mirasgedis, A. Novikova, J. Rilling, H. Yoshino, P. Bertoldi, B. Boardman, M. Brown, S. Joosen, Ph. Haves, J. Harris, and M. Moezzi. Residential and commercial buildings. In B. Metz, O. R. Davidson, P. R. Bosch, R. Dave, and L. A. Meyer, editors, *Climate change 2007: Mitigation. Contribution of Working group III to the Fourth Assessment Report of the Intergovernmental Panel on Climate Change*. Cambridge University Press, Cambridge, United Kingdom and New York, NY, USA, 2007.
- [15] W. Cramer, J. I. Holten, Z. Kaczmarek, P. Martens, R. J. Nicholls, M. Oquist, M. D. A. Rounsevell, J. Szolgay, N. W. Arnell, G. Balint, M. Beniston, G. Berz, M. Bindi, T. R. Carter, S. des Clers, H. Q. P. Crick, A. F. Dlugolecki, T. Dockerty,

- M. Gottfried, G. Grabherr, A. Guisan, M. Hulme, P. Imeson, J. Jenik, A. Jordan, A. Kedziora, S. Kovats, S. Lavorel, M. Livermore, J. Lowe, J. P. Martinez Rica, U. Molau, I. Nemesova, J. E. Olesen, J. P. Palutikof, H. Pauli, A. H. Perry, L. Ryszkowski, S. A. Shchuka, A. Z. Shvidenko, S. Tapsell, J.-P. Theurillat, A. De la Vega-Leinert, A. A. Velichko, and L. Villar. Europe. In J. J. McCarthy, O. F. Canziani, N. A. Leary, D. J. Dokken, and K. S. White, editors, *Climate Change 2001: Impacts, Adaptation and Vulnerability: Contribution of Working Group II to the Third Assessment Report of the Intergovernmental Panel on Climate Change*, chapter Europe, pages 641–692. Cambridge University Press, Cambridge, United Kingdom and New York, NY, USA, 2001.
- [16] N. Milbank. Building design and use: response to climate change. *The architects' journal*, 190:59 – 63, 1989.
- [17] C. G. Granqvist. *Materials Science for Solar Energy Conversion Systems*. Pergamon Press, 1991.
- [18] C. M. Lampert. Heat mirror coatings for energy conserving windows. *Solar Energy Materials*, 6:1 – 41, 1981.
- [19] S. Chaudhuri, D. Bhattacharyya, A. B. Maity, and A. K. Pal. Surface coatings for solar application. *Materials Science Forum*, 246:181 – 206, 1997.
- [20] P. Oelhafen. Optimal spectral transmittance of sun protection glasses. *Proceedings of CISBAT*, 2005:37 – 42, 2005.
- [21] P. Oelhafen. Optimized spectral transmittance of sun protection glasses. *Solar Energy*, 81(9):1191–1195, 2007.
- [22] R. Steiner, P. Oelhafen, G. Reber, and A. Romanyuk. Experimental determination of spectral and angular dependent optical properties of insulating glasses. *Proceedings of CISBAT*, 2005:441 – 446, 2005.
- [23] G. Reber, R. Steiner, P. Oelhafen, and A. Romanyuk. Angular dependent solar gain for insulating glasses from experimental optical and thermal data. *Proceedings of CISBAT*, 2005:173 – 178, 2005.
- [24] Glass in buildings - determination of luminous and solar characteristics of glazing. German version of EN410, November 1998.
- [25] P. Oelhafen. glassdbase - The independent and comprehensive database for building glass. www.glassdbase.unibas.ch, April 2008.
- [26] H. J. Gläser. *Large Area Glass Coating*. Von Ardenne Anlagentechnik GmbH, Dresden, 2005.

- [27] G. Leftheriotis, S. Papaefthimiou, and P. Yianoulis. Development of multilayer transparent conductive coatings. *Solid State Ionics*, 136 - 137:655 – 661, 2000.
- [28] M. Chen, Z. L. Pei, C. Sun, J. Gong, R. F. Huang, and L. S. Wen. ZAO: an attractive potential substitute for ITO in flat display panels. *Mat. Science and Eng.*, B85:212–217, 2001.
- [29] K. H. Choi, J. Y. Kim, Y. S. Lee, and H. J. Kim. ITO/Ag/ITO multilayer films for the application of a very low resistance transparent electrode. *Thin Solid Films*, 341:152–155, 1999.
- [30] K. Utsumi, O. Matsunaga, and T. Takahata. Low resistivity ITO film prepared using the ultra high density ITO targets. *Thin Solid Films*, 334:30–34, 1998.
- [31] A. Klöppel, B. Meyer, and J. Trube. Influence of substrate temperature and sputtering atmosphere on electrical and optical properties of double silver layer systems. *Thin Solid Films*, 392:311 – 314, 2001.
- [32] J. D. Jackson. *Classical Electrodynamics*. John Wiley & Sons, third edition, 1999.
- [33] M. Born and E. Wolf. *Principles of Optics*. Pergamon Press, sixth (corrected) edition, 1986.
- [34] K. Gelin and E. Waeckelgard. Infrared emittance of $\text{Cu}_x - \text{Ni}_{1-x}$ alloys. *J. Phys.: Condens. Matter*, 16:833 – 843, 2004.
- [35] E. Valkonen and B. Karlsson. Optimization of metal-based multilayers for transparent heat mirrors. *Energy Research*, 11:397 – 403, 1987.
- [36] I. Dima, B. Popescu, F. Iova, and G. Popescu. Influence of the silverlayer on the optical properties of the $\text{TiO}_2/\text{Ag}/\text{TiO}_2$ multilayer. *Thin Solid Films*, 200:11 – 18, 1991.
- [37] H. A. Macloed. *Thin-Film Optical Filters*. Institute of Physics Publishing, Bristol and Philadelphia, 2003.
- [38] M. Rubin, K. von Rottkay, and R. Powles. Windows optics. *Solar Energy*, 62(3):149 – 161, 1998.
- [39] S. Baskoutas and N. S. Athanasiou. Optical constants of $\text{TiO}_2/\text{Ag}/\text{TiO}_2$ three-layer thin films. *Modern Physics Letters B*, 11(24):1077–1084, 1997.
- [40] Ph. W. Baumeister. Application of microwave technology to design an optical multilayer bandpass filter. *Appl. Opt.*, 42(13):2407–2414, 2003.

- [41] O. Zueger. Device for combination of light of different wavelengths. <http://www.freepatentsonline.com/20060256445.html>, November 2006.
- [42] O. S. Heavens. *Optical Properties of Thin Solid Films*. Dover Publications, INC. New York, 1991.
- [43] Ph. W. Baumeister. *Optical Coating Technology*. SPIE Press, 2004.
- [44] E. Valkonen, B. Karlsson, and C.-G. Ribbing. Solar optical properties of thin films of Cu, Ag, Au, Cr, Fe, Co, Ni and Al. *Solar Energy*, 32(2):211 – 222, 1984.
- [45] H. J. Gläser. Improved insulating glass with low emissivity coatings based on gold, silver, or copper films embedded in interference layers. *Glass Technology*, 21(5):254 – 261, 1980.
- [46] R. J. Martin-Palma, L. Vazquez, J. M. Martinez-Duart, and Malats-Riera. Silver-based low-emissivity coatings for architectural windows: Optical and structural properties. *Solar Energy Materials and Solar Cells*, 53:55 – 66, 1998.
- [47] J. C. C. Fan and F. J. Bachner. Transparent heat mirrors for solar-energy applications. *Applied Optics*, 15(4):1012 – 1017, 1976.
- [48] X. W. Sun and H. S. Kwok. Optical properties of epitaxially grown zinc oxid films on sapphire by pulsed laser deposition. *Journal of Applied Physics*, 86(1):408 – 411, 1999.
- [49] S. N. A. Rahman, A. Shafii, A .F. M. Nor, and B. Kamaluddin. Electrical and optical properties of indium doped zinc oxid thin films.
- [50] M. C. Larciprete, C. Sibilia, S. Paoloni, and M. Bertolotti. Accessing the optical limiting properties of metallo-dielectric photonic band gap structures. *J. Appl. Phys.*, 93(9):5013 – 5017, 2003.
- [51] T. K. Subramanyam, B. Srinivasulu Naidu, and S. Uthanna. Structure and optical properties of dc reactive magnetron sputtered zinc oxide films. *Cryst. Res. Technol.*, 34:981 – 988, 1999.
- [52] J. C. C. Fan, F. J. Bachner, G. H. Foley, and P. M. Zavracky. Transparent heat-mirror films of $\text{TiO}_2/\text{Ag}/\text{TiO}_2$ for solar energy collection and radiation insulation. *Appl. Phys. Lett.*, 25(12):693 – 695, 1974.
- [53] E. D. Palik, editor. *Handbook of Optical Constants of Solids*. Academic Press, 1st edition, 1997.

- [54] A. F. Mayadas and M. Shatzkes. Electrical-resistivity model for polycrystalline films: the case of arbitrary reflection at external surfaces. *Physical Review B*, 1(4):1382 – 389, 1970.
- [55] C.-C. Huang, J. Tang, and W.-H. Tao. Optical properties of tungsten and titanium oxide thin films prepared by plasma sputter deposition. *Solar Energy Materials & Solar Cells*, 83:15 – 28, 2004.
- [56] D. W. Hoffman. Perspective on stresses in magnetron-sputtered thin films. *J. Vac. Sci. Technol. A*, 12(4):953 – 961, 1994.
- [57] J. A. Thornton. High rate thick film growth. *Ann. Rev. Mater. Sci.*, 7:239 – 260, 1977.
- [58] J. Szczybrowski, A. Dietrich, and K. Hartig. Evaluation and control of the properties of thin sputtered silver films for spectrally selective coatings. *Solar Energy Materials*, 16:103 – 111, 1987.
- [59] B. Chapman. *Glow Discharge Processes; Sputtering and Plasma Etching*. John Wiley & Sons, 1980.
- [60] Materials Science, Inc. Technology Note TN 000 100 02/03. http://www.msipse.com/magnetron_sputtering.htm.
- [61] Leybold-Heraeus. *XTM Technical Manual*.
- [62] H. R. Hertz. Über einen Einfluss des ultravioletten Lichtes auf die elektrische Entladung. *Ann. Physik*, 267(8):983, 1887.
- [63] A. Einstein. Über einen die Erzeugung und Verwandlung des Lichtes betreffenden heuristischen Gesichtspunkt. *Annalen der Physik*, 322:132 – 148, 1905.
- [64] B. Feuerbacher, B. Fitton, and R. F. Willis. *Photoemission and the Electronic Properties of Surfaces*. John Wiley, 1978.
- [65] S. Hüfner. *Photoelectron Spectroscopy - Principles and Applications*. Springer-Verlag, Berlin, third edition, 2002.
- [66] C. Nordling, E. Sokolowski, and K. Siegbahn. Precision method for obtaining absolute values of atomic binding energies. *Phys. Rev.*, 105(5):1676–1677, Mar 1957.
- [67] Varian. *Operation Manual: Cary5*.
- [68] A. Röseler. *Infrared Spectroscopic Ellipsometry*. Akademie-Verlag, Berlin, 1990.

- [69] L.B. Valdes. Resistivity measurements on germanium for transistors. *Proceedings of the IRE*, 42:420 – 427, 1954.
- [70] R. Rymaszewski. Relationship between the correction factor of the four-point probe value and the selection of potential and current electrodes. *J. of Scientific Instruments (Journal of Physics E)*, 2(2):170 – 174, 1969.
- [71] K. Scherpinski, M. Töpfer, F. Krause, K. Halser, R. Hahn, O. Ehrmann, and H. Reichl. Integration of NiCr resistors in a multilayer Cu/BCB wiring system. *International Symposium on Advanced Packaging Materials*, pages 178 – 185, 1999.
- [72] L. Reimer. *Scanning Electron Microscopy: Physics of Image Formation and Microanalysis*. Springer, Berlin, 2008.
- [73] E. Masetti, J. Bulir, S. Gagliardi, V. Janicki, A. Krasilnikova, and C. Coluzza. Ellipsometric and XPS analysis of the interface between silver and SiO_2 , TiO_2 and SiN_x thin films. *Thin solid films*, 455 - 456:468 – 472, 2004.
- [74] Y. Tachibana, K. Kusunoki, and H. Ohsaki. Optical properties of Ag/dielectric-material multilayers. *Vacuum*, 74:555 – 559, 2004.
- [75] Y. Tachibana, K. Kusunoki, T. Watanabe, K. Hashimoto, and H. Ohsakib. Optical properties of multilayers composed of silver and dielectric materials. *Thin Solid Films*, 442:212 – 216, 2003.
- [76] M. Marinov. Effect of ion bombardment on the initial stages of thin film growth. *Thin Solid Films*, 46:267 – 274, 1977.
- [77] L. Pranevichus and S. Tamulevichus. The physical properties of thin Ag films formed under the simultaneous ion implantation in the substrate. *Nuclear Instruments and Methods*, 209/210:179 – 184, 1983.
- [78] E. Chason and B. K. Kellerman. Monte carlo simulations of ion-enhanced island coarsening. *Nucl. Instrum. Meth. B*, 127-128:225 – 229, 1997.
- [79] J. Sillanpää and I. Koponen. Island growth in ion beam assisted metal-on-metal deposition modelled by rate equations. *Nucl. Instrum. Meth. B*, 142:67–76, 1998.
- [80] G. Carter. Island-density and size dynamics in ion-assisted atomic deposition. *Vacuum*, 55(3-4):23–247, 1999.
- [81] M. V. Ramana Murty, Harry A. Atwater, A. J. Kellock, and J. E. E. Baglin. Very low temperature ($< 400^\circ\text{C}$) silicon molecular beam epitaxy: The role of low energy ion irradiation. *Appl. Phys. Lett.*, 62(20):2566 – 2568, 1993.

- [82] A. Romanyuk, R. Steiner, I. Mack, P. Oelhafen, and D. Mathys. Growth of thin silver films on silicon oxide pretreated by low temperature argon plasma. *Surface Science*, 601:1026 – 1030, 2007.
- [83] X. Bao, M. Muhler, Th. Schedel-Niedrig, and R. Schlögl. Interaction of oxygen with silver at high temperature and atmospheric pressure: A spectroscopic and structural analysis of a strongly bound surface species. *Phys. Rev. B*, 54(3):2249 – 2262, 1996.
- [84] L. H. Tjeng, M. B. J. Meinders, J. van Elp, J. Ghijsen, G. A. Sawatzky, and R. L. Johnson. Electronic structure of Ag_2O . *Phys. Rev. B*, 41(5):3190–3199, 1990.
- [85] J. A. Venables, L. Giordano, and J. H. Harding. Nucleation and growth on defect sites: Experiment - theory comparison for Pd/MgO(001). *Journal of Physics: Condensed Matter*, 18(16):S411 – S427, 2006.
- [86] H. A. van der Vegt, W. J. Huisman, P. B. Howes, T. S. Turner, and E. Vlieg. Surfactants used in Ag(111) homoepitaxy: Sb, In, Pt and O_2 . *Surface Science*, 365(2):205 – 211, 1996.
- [87] W. Zhang, Y. Li, S. Zhu, and F. Wang. Influence of argon flow on TiO_2 photocatalyst film deposited by dc reactive magnetron sputtering. *Surface and Coatings Technology*, 182:192 – 198, 2004.
- [88] R. J. Martin-Palma and J. M. Martinez-Duart. Ni–Cr passivation of very thin Ag films for low-emissivity multilayer coatings. *J. Vac. Sci. Technol. A*, 17(6):3449 – 3451, 1999.
- [89] T. Okamura, S. Fukuda, K. Koike, H. Saigou, M. Yoshikai, M. Koyama, T. Misawa, and Y. Matsuzaki. Optical filters for plasma display panels using organic dyes and sputtered multilayer coatings. *J. Vac. Sci. Technol. A*, 19(4):1090 – 1094, 2001.
- [90] E. Kusano, J. Kawaguchi, and K. Enjouji. Thermal stability of heat-reflective films consisting of oxide-Ag-oxide deposited by dc magnetron sputtering. *J. Vac. Sci. Technol. A*, 4(6):2907 – 2910, 1986.
- [91] X.-Y. Gao, S.-Y. Wang, J. Li, Y.-X. Zheng, R.-J. Zhang, P. Zhou, Y.-M. Yang, and L.-Y. Chen. Study of structure and optical properties of silver oxide films by ellipsometry, XRD and XPS methods. *Thin Solid Films*, 455- 456:438 – 442, 2004.
- [92] J.-H. Qiu, P. Zhou, X.-Y. Gao, J.-N. Yu, S.-Y. Wang, J. Li, Y.-X. Zheng, Y.-M. Yang, Q.-H. Song, and L.-Y. Chen. Ellipsometric study of the optical properties

- of silver oxide prepared by reactive magnetron sputtering. *Journal of the Korean Physical Society*, 46:S269 – S275, 2005.
- [93] P. M. Martin, D. C. Stewart, W. D. Bennett, J. D. Affinito, and M. E. Gross. Multifunctional multilayer optical coatings. *J. Vac. Sci. Technol. A*, 15(3):1098 – 1102, 1997.
- [94] J. C. Runkle. Method of producing a silicon/aluminum sputtering target. <http://www.freepatentsonline.com/6214177.html>, April 2001.
- [95] M. Ruske, G. Brauer, J. Pistner, J. Szczyrbowski, and M. Weigert. Properties of SiO₂ and Si₃N₄ layers deposited by mf twin magnetron sputtering using different target materials. *Thin Solid Films*, 351(1-2):158–163, 1999.
- [96] E. Barthel, O. Kerjan, P. Nael, and N. Nadaud. Asymmetric silver to oxide adhesion in multilayers deposited on glass by sputtering. *Thin Solid Films*, 473:272 – 277, 2005.
- [97] G. Hass, J. B. Heaney, H. Herzig, J. F. Osantowski, and J. J. Triolo. Reflectance and durability of Ag mirrors coated with thin layers of Al₂O₃ plus reactively deposited silicon oxide. *Applied Optics*, 14(11):2639 – 2644, 1975.
- [98] M. Arbab. The base layer effect on the d.c. conductivity and structure of direct current magnetron sputtered thin films of silver. *Thin Solid Films*, 381:15 – 21, 2001.
- [99] V. A. Coleman, J. E. Bradby, C. Jagadish, P. Munroe, Y. W. Heo, S. J. Pearton, D. P. Norton, M. Inoue, and M. Yano. Mechanical properties of ZnO epitaxial layers grown on a- and c-axis sapphire. *Appl. Phys. Lett.*, 86:203105, 2005.
- [100] S.V. Prasad and J.S. Zabinski. Tribological behavior of nanocrystalline zinc oxide films. *Wear*, 203 - 204:498 – 506, 1997.
- [101] L.-Y. Lin, M.-Ch. Jeong, D.-E. Kim, and J.-M. Myoung. Micro/nanomechanical properties of aluminum-doped zinc oxide films prepared by radio frequency magnetron sputtering. *Surface and Coatings Technology*, 201:2547 – 2552, 2006.
- [102] S. O. Kucheyev, J. E. Bradby, J. S. Williams, and C. Jagadish. Mechanical deformation of single-crystal ZnO. *Appl. Phys. Lett.*, 80(6):956 – 958, 2002.
- [103] Zh. Q. Yao, P. Yang, N. Huang, H. Sun, G. J. Wan, Y. X. Leng, J. Wang, and J. Y. Chen. Fabrication and surface characterization of pulsed reactive closed-field unbalanced magnetron sputtered amorphous silicon nitride films. *Surface and Coatings Technology*, 200:4144 – 4151, 2006.

List of Acronyms

AF45	laboratory glass substrate, classification AF45
CCD	charge-coupled device, CCD-Chip
CIE	Commission internationale de l' éclairage
CIE Lab colour space	Commission internationale de l' éclairage luminosity ab-coordinates colour space
dc	direct current
ESCA	Electron Spectroscopy for Chemical Analysis
rf	radio frequency
GPIB	GPIB instrumentation bus, classification IEEE-488
IPCC	Intergovernmental Panel on Climatic Changes
Low-E glasses	low emissivity glasses
PES	photon electron spectroscopy
ppb	parts per billion
ppm	parts per million
PTFE	Poly Tetra Fluoro Ethylene, known as Teflon
SEM	scanning electron microscopy
SPG	sun protection glasses
UHV	ultra high vacuum
UPS	ultra-violette photon electron spectroscopy
VASE	Variable Angle Spectroscopic Ellipsometer
XPS	X-ray photon electron spectroscopy

Important Quantities

α	absorptance
$D_{65}(\lambda)$	standard illuminant
E_B	binding energy
η	optical admittance
g	total solar energy transmittance factor, solar gain
k	extinction coefficient
\hat{n}	complex refractive index
n	real refractive index
R_{\square}	sheet resistance
ϱ	reflectance
ϱ	resistivity
$S_{\lambda}(\lambda)$	solar radiation
τ	transmittance
$\tau(\lambda)$	spectral transmittance
$\tau_{min}(\lambda)$	theoretical minimised spectral transmittance
τ_v	light transmittance
τ_e	solar direct transmittance
τ_e/τ_v	energy load coefficient
$V(\lambda)$	spectral photopic luminous efficiency
$\bar{x}_{\lambda}, \bar{y}_{\lambda}, \bar{z}_{\lambda}$	CIE colour-matching functions

Acknowledgment

After finishing my PhD-thesis I would like to thank all who contributed in one or the other way to this work.

- First of all I want to thank Professor Peter Oelhafen for the interesting and forward-looking topic. Furthermore, I want to thank him for his support and encouragement during the last years.
- Next, I would like to thank Professor E. Meyer for his interest in my work and the kind acceptance of the Korreferat.
- The Glas Trösch AG, I would like to thank for their cooperation and for giving me the possibility to deposited my multilayer coatings in their laboratories. In this context my special thanks go to F. Kamecke, St. Rögels, P. Salvo, W. Haag and P. Pecher and all the others of the development group.
- I would like to express my gratitude to Andreas Schüler for the fruitful discussions, the simulation sessions in Lausanne and for reading this manuscript carefully.
- Then I want to thank my colleagues and former colleagues: Michael Büttner, Laurent Marot, Roland Steiner, Gregory de Temmermann, Teresa de los Arcos, Andriy Romanyuk, Georges Reber and Jamila Boudaden.
- Furthermore, I want to thank Bernd Heimann, Michael Steinacher and Werner Erni from the electronics laboratory, who always helped when there were major or minor problems with the electronics in the lab. A special thanks goes to Bernd Heimann, who spend hours in the dim windows-lab helping me to measure the optical properties of my new coatings.
- Then there are the two very kind ladies, Barbara Kammermann and Astrid Kalt, from the secretary, who always help with a smile independent of the problem you address them with. I would like to thank them for this.

- Then I want to thank the colleagues from the Zentrum für Mikroskopie of the University of Basel, Daniel Mathys and Marcel Düggelin, for their effort to obtain SEM images even if the samples were changing under the electron beam.
- The Bundesamt für Energie (BFE) I want to thank for their financial support of this project.
- I would like to thank my mother, my father and my sisters, Sonja and Corinna, for their great support throughout my studies and this PhD. They were always there when I needed advice or just someone to talk to. Furthermore I would like to thank my mother and my father for their critical reading of this thesis and finding the errors and the imprecisions which you do not recognise if you work in a topic for some time.
- My special thanks goes to Rich Schuler, for reading this thesis and removing the germanised sentences that slipped through my fingers.
- And finally I would like to express my great thanks to my boy-friend Stefan, who was reading this thesis with a very critical eye and has always been supportive and patient even in the times when things were not going smooth.

Curriculum Vitae

Name: Iris Mack
Born: 15.08.1976 in Tübingen, Germany
Nationality: German

Scholar Education

Sep. 1983 – Aug. 1986 Primary School Österfeld, Stuttgart-Vaihingen, Germany
Sep. 1986 – Aug. 1990 European School Culham, Great Britain
Jan. 1991 – July 1996 Fanny-Leicht-Gymnasium (secondary school), Stuttgart-Vaihingen, Germany
July 1996 Abitur (university entrance exam)

Academic Education

Oct. 1996 – Jul. 1999 Academic studies in physics at the University of Stuttgart, Germany
Sep. 1998 Intermediate diploma
Aug. 1999 – June 2000 University of Missouri, St. Louis and Washington University in St. Louis, United States of America
May 2000 Master of Arts and Science
Jan. 2001 – Dec. 2002 Academic studies in physics at University of Karlsruhe, Germany
Sep. 2001 – Sep. 2002 Diploma thesis at the Institute for Applied Physics with Professor Schimmel: "Electrochemical Nano Structuring of Nickel and Copper: Deposition and Solving Activated with the AFM-Tip"
Dec. 2002 Diploma in Physics
Sep. 2003 – present PhD at the University of Basel, Switzerland

Experiences during Education

Sep. 1996 – July 1999	Software engineer at the University of Stuttgart, Germany Field: Distributed File Systems (DCE, DFS), Unix, Scripting, Documentation, Programming
Sep. 1998 – Feb. 1999	Instructor of an Unix introduction course for first year students at the University of Stuttgart, Germany
May 2000	Research assistance of Professor Ph. Frauendorf Centre for Molecular Electronics, University of Missouri St. Louis, USA Topic: TEM Investigation of Surface Defects on Silicon
Sep. 2001 - Sep. 2002	Teaching assistance at the University of Karlsruhe, Germany Course: Physics for Electrical Engineers
Sep. 2003 - Mar. 2008	Teaching assistance at the University of Basel, Switzerland Course: Physics for Biologists, Pharmacists and Geologists
June 2007	Teacher in physics (stand-in) at the secondary school (Kantonsschule) Baden, Switzerland

List of Professors Contributing to my Education

At the University of Basel: P. Oelhafen

At the University of Karlsruhe: Th. Schimmel, H. Kalt, and C. Klingshirn

At the University of Missouri, St. Louis: P. Händel, R. Flores, and Ph. Frauendorf

At the Washington University in St. Louis: W. Suen, and J. Schilling

At the University of Stuttgart: E. Wielandt, K. Höllig, J. Weidlein,

M. Pilkuhn, U. Kneißel, G. Wunner, M. Bestehorn, and G. Mahler